Optical and electric field control of magnetism

Ashima Arora

Dissertation

zur Erlangung des akademischen Grades
doctor rerum naturalium
(Dr. rer. nat.)
in der Wissenschaftsdisziplin
Physik kondensierter Materie

eingereicht an der
Mathematisch-Naturwissenschaftlichen Fakultät
Institut für Physik und Astronomie
der Universität Potsdam
und
Helmholtz Zentrum Berlin

Hauptbetreuer: apl. Prof. Dr. Oliver Rader
Weitere Gutachter: Prof. Dr. Wolfgang Kuch
Prof. Dr. Frithjof Nolting

Potsdam, den 8.10.2018

Published online at the
Institutional Repository of the University of Potsdam:
URN urn:nbn:de:kobv:517-opus4-421479
https://nbn-resolving.org/urn:nbn:de:kobv:517-opus4-421479

Abstract

Future magnetic recording industry needs a high-density data storage technology. However, switching the magnetization of small bits requires high magnetic fields that cause excessive heat dissipation. Therefore, controlling magnetism without applying external magnetic field is an important research topic for potential applications in data storage devices with low power consumption. Among the different approaches being investigated, two of them stand out, namely i) all-optical helicity dependent switching (AO-HDS) and ii) ferroelectric control of magnetism. This thesis aims to contribute towards a better understanding of the physical processes behinds these effects as well as reporting new and exciting possibility for the optical and/or electric control of magnetic properties. Hence, the thesis contains two differentiated chapters of results; the first devoted to AO-HDS on TbFe alloys and the second to the electric field control of magnetism in an archetypal Fe/$BaTiO_3$ system.

In the first part, the scalability of the AO-HDS to small laser spot-sizes of few microns in the ferrimagnetic TbFe alloy is investigated by spatially resolving the magnetic contrast with photo-emission electron microscopy (PEEM) and X-ray magnetic circular dichroism (XMCD). The results show that the AO-HDS is a local effect within the laser spot size that occurs in the ring-shaped region in the vicinity of thermal demagnetization. Within the ring region, the helicity dependent switching occurs via thermally activated domain wall motion. Further, the thesis reports on a novel effect of thickness dependent inversion of the switching orientation. It addresses some of the important questions like the role of laser heating and the microscopic mechanism driving AO-HDS.

The second part of the thesis focuses on the electric field control of magnetism in an artificial multiferroic heterostructure. The sample consists of an Fe wedge with thickness varying between 0.5 nm and 3 nm, deposited on top of a ferroelectric and ferroelastic $BaTiO_3$ [001]-oriented single crystal substrate. Here, the magnetic contrast is imaged via PEEM and XMCD as a function of out-of-plane voltage. The results show the evidence of the electric field control of superparamagnetism mediated by a ferroelastic modification of the magnetic anisotropy. The changes in the magnetoelastic anisotropy drive the transition from the superparamagnetic to superferromagnetic state at localized sample positions.

Kurzfassung

Die Herstellung zukünftiger magnetischer Datenspeicher erfordert eine hohe Speicherdichte mit entsprechend kleinen Bits. Das Schalten der Magnetisierung kleiner Strukturen benötigt jedoch starke Magnetfelder, die einen hohen Energieverbrauch und Wärmeeintrag verursachen. Daher ist das Schalten von Magnetismus ohne Anlegen eines externen Magnetfeldes ein wichtiges Forschungsthema für potentielle Anwendungen in der Datenspeicherung mit geringem Stromverbrauch. Unter den verschiedenen Ansätzen, die verfolgt werden, heben sich zwei hervor, nämlich i) rein optisches helizitätsabhängiges Schalten (AO-HDS) und ii) magnetoelektrische Kontrolle von Magnetismus. Diese Arbeit soll zu einem besseren Verständnis der physikalischen Prozesse beitragen, die hinter diesen Effekten stehen, sowie neue und aufregende Möglichkeiten für die optische und/ oder elektrische Kontrolle magnetischer Eigenschaften aufzeigen. Daher sind die Ergebnisse dieser Arbeit in zwei Kapitel gegliedert; das erste befasst sich mit dem helizitätsabhängigen optischen Schalten in Eisen-Terbium Legierungen und das zweite Kapitel widmet sich der magnetoelektrischen Kopplung in Hybridsystemen, bestehend aus einer ferromagnetischen Eisenschicht welche auf ferroelektrischen Bariumtitanat gewachsen wurde.

Im ersten Kapitel wird die Skalierbarkeit des helizitätsabhängigen optischen Schaltens in ferrimagnetischen Eisen-Terbium Legierungen mit Laserspotgrößen im Mikrometer Bereich untersucht. Photoelektronenmikroskopie (PEEM) in Kombination mit magnetischem Röntgendichroismus (XMCD) wird verwendet um die resultierende Magnetisierung hochaufgelöst abzubilden. Die Ergebnisse zeigen, dass helizitätsabhängiges optisches Schalten ein lokaler Effekt innerhalb des Laserspots ist, der in der ringförmigen Region in der Nähe der thermischen Entmagnetisierung auftritt. Innerhalb der Ringregion erfolgt die Umkehr der Magnetisierung über thermisch aktivierte Domänenwandbewegung. Des Weiteren berichtet die Arbeit über einen neuartigen Effekt der die Helizitätsabhängigkeit mit zunehmender Schichtdicke umkehrt. Auch werden wichtigen Fragen wie der Rolle thermischer Effekt oder die mikroskopische Ursache helizitätsabhängigen Schaltens beleuchtet.

Der zweite Teil der Arbeit konzentriert sich auf die elektrische Kontrolle des Magnetismus in einer künstlichen multiferroischen Heterostruktur. Die Probe besteht aus einem Eisen-Keil mit einer Dicke zwischen 0.5 nm und 3 nm, der auf einem ferroelektrischen und ferroelastischen Bariumtitanat abgeschieden ist. Hier wird der magnetische Kontrast als Funktion des elektrischen Feldes untersucht. Die Ergebnisse belegen die Möglichkeit superparamagnetische Bereiche per elektrischen Feld zu steuern. Die magnetelektrische Kopplung erfolgt durch eine ferroelastische Modifikation der magnetischen Anisotropie. Die Änderungen in der magnetoelastischen Anisotropie erlauben elektrisches Schalten zwischen dem superparamagnetischen zu dem superferromagnetischen Zustand.

Acknowledgements

My life as a PhD student at Bessy II has been an incredible journey. The very first experience of seeing a synchroton ring was intimidating but I have surely come a long way. I have been fortunate enough to work in an extremely supporting environment and with the kindest people I have ever met.

First of all, I would like to thank Dr. Florian Kronast for your constant support and guidance throughout these years. I am grateful for the countless number of hours you have invested in me. Without your knowledge and experience, this thesis would not have been possible. Your positive attitude and enthusiasm towards work and life has been very motivating. Next I would like to thank Dr. Sergio Valencia for assisting me with your expertise during my PhD. It was a great learning experience to analyze the mysterious data with you. I am glad we finally made it. You have been extremely supportive and understanding during the tough times I had during my PhD. Thank you for making me feel better when I was feeling down. Your sense of humor made the stressful beam-times so much better. A special thanks to Florian and Sergio for putting so much time and effort in correcting my thesis, preparing me for countless talks, and posters and always encouraging me during all these years. I have learnt a lot from both of you, not only work wise, but also how to maintain a nice work-life balance.

I am grateful to Prof. Oliver Rader for providing me the opportunity to work at Helmholtz Zentrum Berlin and the amazing world of the synchroton. I am thankful for your guidance and invaluable input during my PhD. I would like to thank Dr. Florin Radu and Dr. Chen Luo for making the samples for the experiments and providing the feedback for the manuscript. I am grateful to Dr. Ahmet Unal for his help during the experiments during beam-times and bringing positivity to the workplace. Sharing an office with you was a pleasure. I am thankful to Dr. Mohammed Mawass for his support and discussions during the beam-times. I am thankful to Dr. Konrad Siemensmeyer for helping me with the never ending SQUID measurements. I want to thank Lukas Gierster and Matteo Cialone for being amazing colleagues. I am thankful to Oliver Sandig for his contribution to the experiments, and also for being a kind friend. I am thankful to Dr. Lee Phillips for the insightful discussions and investing so much time to work on the paper. Your dedication towards work is very motivating.

Being new to a foreign country, it was challenging to settle down, finding apartment, filling countless forms and struggling with the German language. I am grateful to all the people, specially Annette and Gaurav, who helped me to make Berlin my home away from home. Living in Berlin could not have been so much fun if it wasn't for Kanika and Tanya. It has been an amazing experience exploring Berlin together, supporting, and tolerating each other through thick and thin. I have been blessed with wonderful long-distance friends Surabhi, Anubhuti, Karandeep, Vrinda, and Vivek who have always been there for me, no matter what. The long phone calls and skype sessions are much appreciated. I would like to thank Atul for living my PhD journey with me, helping me stay awake during the long hours of beamtime, for always encouraging and believing in me, and for being so supportive in every aspect of life. You inspire me everyday.

I am forever indebted to my parents and my brothers Anshul and Sahil for their unconditional love and support. Thank you for believing in me and sending me so far away from home. I hope I made you proud.

Contents

Introduction

Magnetic recording is one of the most successful data storage technologies. Magnetic storage media encodes bits in the form of magnetic domains with magnetization being anti-parallel for bits '0' and '1'. The conventional method for writing the information is by applying magnetic fields strong enough to set the desired bit to the '0' or '1' state [1]. Significant effort has been made for increasing the storage density of such devices by decreasing the area representing a bit. However, smaller bits have higher coercivity and thus require higher magnetic fields to switch the magnetization. The huge magnetic field generated by the current coil consumes enormous power. Heat dissipation in such devices is a major problem for the data storage industry.

Controlling magnetism without applying external magnetic fields is therefore important for the magnetic data storage devices with low power consumption. This emergent field of research in condensed matter physics addresses, among others, magnetization switching via spin-transfer torque [2], spin-polarized currents [3], external electric fields [4, 5], and circularly polarized femtosecond laser pulses [6]. Recent results have shown the possibility of controlling the magnetic anisotropy [7], magnetic domain pattern [6], domain wall motion [8, 9], critical temperatures [10, 11], exchange bias [12], spin polarization [13], magnetic ordering [14] and established 180° magnetization switching [15, 16] in magnetic materials without the need of magnetic fields. These pathways offer advantages over conventional read/write heads such as high switching speed and low heat dissipation. This thesis aims at exploring two of these alternative routes to manipulate the magnetization in magnetic materials without applying any external magnetic field, namely (i) via femtosecond laser pulses and (ii) by using electric fields. A more recent data storage technology, HAMR (Heat-assisted magnetic recording), uses laser pulses to locally heat up the magnetic sample and switch the local magnetization with a low magnetic field at elevated temperature. However, there are still some problems such as synchronization of the laser and magnetic field pulses, providing an efficient heat sink, focussing the laser spot below the diffraction limit [17]. An elegant way to get rid of magnetic fields is to use the recent discovery of all-optical helicity dependent switching (AO-HDS), where the helicity of the circularly polarized femtosecond laser pulses is used to deterministically switch the magnetization in ferrimagnetic thin films of rare-earth transition-metal (RE-TM) alloys [6]. It has been shown that the AO-HDS is a general phenomenon occurring in a wide variety of materials ranging from RE-TM ferrimagnetic alloys, multi-layers and heterostructures to ferromagnets [15,16]. AO-HDS is a promising candidate for future magnetic data storage since it offers a low-power consumption optical control of magnetization without

the need of any external magnetic fields. However, after abundant research efforts for a decade, some open questions remain that have inhibited the fundamental understanding and the technological realization of the AO-HDS in storage devices. For instance, the scalability of the switching process down to small laser spot sizes is poorly understood. In addition, the importance of laser heating and the fundamental mechanism behind the switching are also under debate.

The electric field contol of magnetic properties requires multiferroic systems with significant magnetoelectric (ME) coupling at room temperature [18]. Multiferroic materials are characterized by a simultaneous presence of different ferroic long-range orders such as magnetism and ferroelectricity. They have a great potential towards controlling the magnetic bits with external voltage provided that the ME coupling is strong enough. Early work searched for a single phase material possessing magnetic and ferroelectric ordering [19]. However these are mutually exclusive properties since ferroelectrics have empty d orbitals whereas magnetism requires partially filled d/f orbitals. Their coexistence is only found for materials that simultaneously break space-inversion and time-reversal symmetry [20]. In this case, the magnetoelectric coupling tends to be rather small and the coexistence of magnetic and ferroelectric phases is observed at temperatures far below room temperature (RT). In this context, artificial composite multiferroics have emerged to be a promising alternative as they offer the possibility to select the magnetic and FE components for designing heterostructures with strong ME behavior at temperatures close and above RT. Fe and $BaTiO_3$ (BTO) are two archetypal ferromagnetic and ferroelectric systems, respectively which received lot of interest when Duan *et al.* predicted a robust magneto-electric coupling at the interface of the Fe/BTO composite system leading to novel interface phenomena [21]. Some of these predictions were confirmed by the experimental observation of room-temperature magnetoelectric coupling at the Fe/BTO interface [13, 22]. In addition to the ferromagnetic properties of thin-film heterostructures, the superparamagnetic properties of non-interacting nanoparticles such as the blocking temperature have also been manipulated by changing the magnetic anisotropy with an electric field [10]. This suggests that for systems with interacting nanoparticles, it might be also possible to control the transition temperature between their superparamagnetic and superferromagnetic state by changing the magnetic anisotropy with an electric field. This electric field control of magnetism at nanometer scale has a tremendous potential for novel non-volatile storage media.

The first part of this thesis investigates the scalability of the helicity dependent switching process to small laser spot-sizes of few microns in TbFe. The second part of the

thesis focuses on investigating the ME coupling in an artificial multiferroic heterostructure consisting of an Fe wedge ($0.5 - 3$ nm) fabricated on a BTO [001] single crystal substrate. With the help of element selective magnetic imaging capabilities of XPEEM (X-ray photoemission electron microscopy), the laser and electric field induced changes in the magnetic properties of TbFe and Fe, respectively, are examined.
The thesis is divided into five chapters. It begins with an introduction to the fundamental concepts of magnetism and ferroelectricity in Chapter 1. Chapter 2 describes the X-ray spectroscopic techniques used in the measurements performed for this thesis. It is followed by Chapter 3 which describes the XPEEM experimental chamber at BESSY II. Chapter 4 deals with the motivation and the experimental results concerning the investigation of AO-HDS in TbFe alloys. Chapter 5 describes the state-of-the-art of experimental studies of magnetoelectric coupling in composite multiferroics and the results on electric field control of magnetism in Fe/BTO.

Chapter 1

Fundamentals

1.1 Magnetism

The magnetic moment of an atom arises from the angular momentum of the electrons. Classically, the orbital magnetic moment $\boldsymbol{m}$ is due to the rotation of the electrons around the nucleus and is given by,

$$\boldsymbol{m} = -\frac{e\mu_o}{2m_e}\boldsymbol{l} \tag{1.1}$$

where e is the electronic charge, m_e is the electron mass, $\mu_o = 4\pi \times 10^{-7}$ H/m is the permeability of vacuum and $\boldsymbol{l}$ is the classical orbital angular momentum. In quantum physics, spin angular momentum also contributes to the total angular momentum. The orbital angular momentum $\boldsymbol{L_i}$ and the spin angular momentum $\boldsymbol{S_i}$ of an electron is quantized. The square of orbital angular momentum and its projection along arbitrary z-axis (direction determined by external magnetic field) are given by,

$$|\boldsymbol{L_i}|^2 = l(l+1)\hbar^2 \tag{1.2}$$

$$L_z = m_l\hbar \qquad \text{with} \qquad m_l = 0, \pm 1, \pm 2, ... \pm l \tag{1.3}$$

where l is the orbital quantum number with $l \in \{0, 1, 2, \ldots, (n-1)\}$ where n is the principal quantum number and m_l is the magnetic quantum number. The square of spin angular momentum and its projection along the z-axis are given by

$$|\boldsymbol{S_i}|^2 = s(s+1)\hbar^2 \tag{1.4}$$

$$S_z = m_s\hbar \qquad \text{with} \qquad m_s = \pm s \tag{1.5}$$

where m_s is the secondary spin quantum number and s is the spin quantum number which exists only as a half integer $s = 1/2$ for an electron. For an atom with more than one electron, the spin and the orbital angular momentum is the sum of the contributions from individual electrons.

$$\boldsymbol{L} = \sum \boldsymbol{L_i} \tag{1.6}$$

$$\boldsymbol{S} = \sum \boldsymbol{S_i} \tag{1.7}$$

The total angular momentum $\boldsymbol{J}$ is the sum of contributions from the orbital and the spin angular momentum which is given by

$$\boldsymbol{J} = \boldsymbol{L} + \boldsymbol{S} \tag{1.8}$$

Similar to the spin and orbital angular momenta, the total angular momentum is also quantized. The square of the total angular momentum is given by,

$$|\boldsymbol{J}|^2 = j(j+1)\hbar^2 \qquad |l-s| < j < |l+s| \tag{1.9}$$

where j is the total angular momentum quantum number. The expectation value of the total magnetic moment can be written as,

$$< m_{total} >= -\frac{e\mu_o}{2m_e}(< l_z > + g_s < s_z >) = -\frac{\mu_B}{\hbar}(< l_z > + g_s < s_z >) \tag{1.10}$$

where μ_B is the Bohr magneton, g_s is the so-called Landé g-factor, and $< l_z >$ and $< s_z >$ are the expectation values of the z-component of the orbital and spin angular momentum, respectively.

The spin and the orbital components of the total angular momentum are not entirely independent and exhibit a 'spin-orbit coupling'. In the classical model, this can be intuitively understood by considering the orbital motion of an electron around the nucleus. In a circular orbit, an electron has an orbital momentum. In the rest frame of an electron, the nucleus revolves around the electron in a current loop. The magnetic field generated from this loop is seen by the spin of the electron, coupling the electron's orbital motion with its spin. The so-called $\boldsymbol{LS}$ coupling also affects the Hund's rules which define the minimum energy ground state of a multi-electron system. The third

Hund's rule is a consequence of the spin-orbit interaction. It states that the total angular momentum $\boldsymbol{J}$ equals $\boldsymbol{L}+\boldsymbol{S}$ for more than half full shell and $\boldsymbol{L}-\boldsymbol{S}$ for less than half full shell. For less than a half full shell, the lowest energy state is the one where the spin is anti-parallel to the orbital angular momentum. For more than a half-full shell, a parallel configuration is energetically favorable. Other interactions such as $\boldsymbol{JJ}$ coupling occur for heavier elements where the individual total angular momentum of electrons interact with each other.

1.2 Models for ferromagnetism

Ferromagnetism arises from a short-range 'exchange interaction' which enables the neighboring magnetic moments to align with each other. The Heisenberg model of ferromagnetism describes the exchange interaction with a Heisenberg Hamiltonian which is given by

$$H_{exch} = -J \sum_{i<j} \boldsymbol{S_i} \boldsymbol{S_j} \tag{1.11}$$

where $\boldsymbol{S_i}$ and $\boldsymbol{S_j}$ are neighboring atomic spins and J is the exchange integral that represents the strength of exchange interactions between the spins i and j. This model considers the localized nature of the electrons around the atom. An overlap between the electronic wave functions and a correlation between the electronic spins leads to a magnetically ordered state. However, the Heisenberg model leads to magnetic moment values which are integer multiples of μ_B and hence fails to explain the experimentally observed non-integer values of magnetic moment in transition metals like Fe, Co, or Ni. The reason behind the disagreement of this theory with experimental evidences is that this theory is based on localized electrons around atoms and does not take into account the itinerant electrons in metals.

This limitation is overcomed by the 'band theory' which suggests that the available energy states for electrons are in the form of continuous energy bands instead of discrete energy values. These energy bands are a consequence of the orbital interactions between the mobile electrons in a metal.

In a non-magnetic metal, there is an equal density of states ($D(E_F)$) of spin-up and spin-down electrons at the Fermi level. In the presence of an internal Weiss mean field ($\boldsymbol{H} = \lambda \boldsymbol{M}$) the centers of gravity of the states characterized by opposite spins exhibit an energy separation. Some of the electrons at the Fermi energy (E_F) undergo a spin-flip causing an imbalance of the so-called 'minority band' and the 'majority band' with 'spin-up' and 'spin-down', respectively (Figure 1.1). The spin-up and spin-down are defined with respect to a quantization direction which is chosen along the magnetic field

H used to align the magnetization of the sample. The number of electrons transferred from minority to majority band are $D(E_F)\delta E/2$ where δE is the energy gain per electron. The total gain in the kinetic energy with this flip is given by

$$\Delta E_{kin} = \frac{1}{2} D(E_F)(\delta E)^2 \tag{1.12}$$

and is also accompanied by a decrease in the potential energy.

$$\Delta E_{pot} = -\frac{1}{2}\mu_o \boldsymbol{M}\boldsymbol{H} \tag{1.13}$$

which, considering the Weiss mean internal field $\boldsymbol{H} = \lambda \boldsymbol{M}$, can be written as

$$\Delta E_{pot} = -\frac{1}{2}\lambda\mu_o |\boldsymbol{M}|^2 \tag{1.14}$$

The magnetization $\boldsymbol{M}$ is given by the difference in the number density of electrons (n_e) or holes (n_h) in the majority (maj) and minority bands (min), defined in Figure 1.1, according to,

$$|\boldsymbol{M}| = \mu_B(n_e^{maj} - n_e^{min}) = \mu_B(n_h^{maj} - n_h^{min}) \tag{1.15}$$

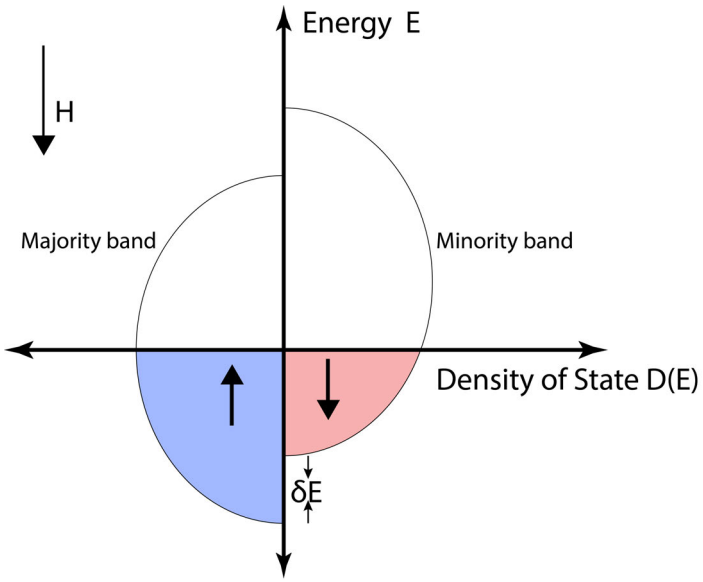

Figure 1.1: Schematic showing the density of states of $3d$ bands near Fermi level E_F in $3d$ transition metals. Splitting of spin-up and spin-down electron states at Fermi level giving rise to ferromagnetism.

The number density of holes in the majority and minority bands is given by

$$n_h^{maj}/n_h^{min} = \frac{1}{2}(n \pm D(E_F))\delta E \tag{1.16}$$

where n is the total number density of electrons in both bands.
Using equation 1.15 and 1.16 in equation 1.14, the potential energy can be expressed as

$$\Delta E_{pot} = -\frac{1}{2}\lambda\mu_o\mu_B^2 D(E_F)^2(\delta E)^2 \tag{1.17}$$

The total change in energy is the sum of the contributions from kinetic and potential energy terms and is given by

$$\Delta E = \Delta_{kin} + \Delta_{pot} = \frac{1}{2}D(E_F)(\delta E)^2 - \frac{1}{2}\lambda\mu_o\mu_B^2 D(E_F)^2(\delta E)^2 \tag{1.18}$$

Defining $I = \mu_o\mu_B^2\lambda$

$$\Delta E = \Delta_{kin} + \Delta_{pot} = \frac{1}{2}D(E_F)(\delta E)^2 - \frac{1}{2}ID(E_F)^2(\delta E)^2$$

$$\Delta E = \frac{1}{2}D(E_F)(\delta E)^2(1 - ID(E_F)) \tag{1.19}$$

The change in energy is negative and gives rise to ferromagnetism if

$$ID(E_F) > 1 \tag{1.20}$$

This condition is known as the Stoner criterion for ferromagnetism. Therefore, an imbalance between spin-up and spin-down electrons gives rise to ferromagnetism in transition metals as long as the Stoner criterion is fulfilled and there is sufficient density of states available at the Fermi level. The Stoner model explains the experimentally observed non-integer multiples of the value of magnetic moment for the transition metals.

Macroscopically, a magnetic material placed in a magnetic field ($\boldsymbol{H}$) experiences a magnetic force and becomes magnetized. This magnetization is represented by the magnetization vector $\boldsymbol{M}$, which is equal to the dipole moment per unit volume and is proportional to $\boldsymbol{H}$.

$$\boldsymbol{M} = \chi\boldsymbol{H} \tag{1.21}$$

where χ is known as the magnetic susceptibility.

Ferromagnetic materials are characterized by a non-zero spontaneous magnetization even in the absence of magnetic field. Unlike paramagnets and diamagnets, the magnetization of ferromagnets is not a linear function of magnetic field and exhibits a hysteretic behavior (see Figure 1.2). Increasing the strength of the magnetic field leads to an increase in the magnetization in a non-linear manner until H_s where the magnetization saturates (M_s).
Further increase of magnetic field has no effect on the magnetization since all the magnetic moments are already aligned along the magnetic field. When the field is reduced to zero from the positive value, the material retains some remanent magnetization M_r. To obtain a zero magnetization, the magnetic field further must be driven towards negative values. The critical field at which magnetization changes sign is known as the coercive field H_c of the ferromagnet.

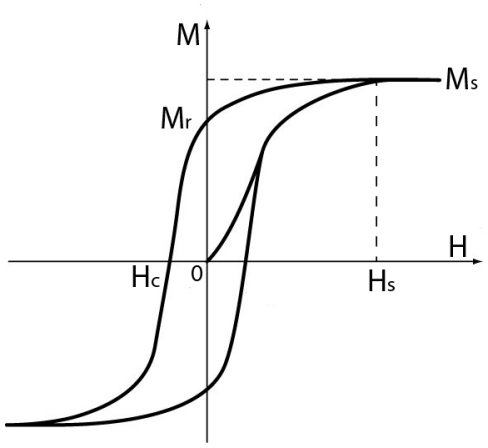

Figure 1.2: Schematic showing magnetic hysteresis loop of a ferromagnetic material.

The magnetization of a ferromagnet decreases with increasing temperature due to competition between the ferromagnetic order and the thermal energy. At a particular temperature known as the Curie temperature (T_c), the thermal energy dominates and the material undergoes a transition from ferromagnetic to paramagnetic behavior (see Figure 1.3). Such a transition can be understood as a competition between thermal energy and exchange interaction favoring disorder and parallel alignment of the magnetic moments, respectively.

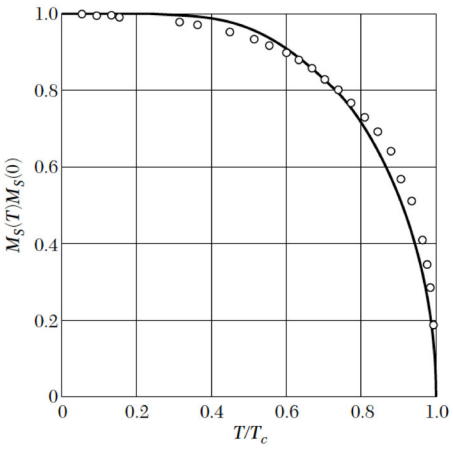

Figure 1.3: Plot showing the theoretically calculated (line) and experimentally measured (circles) saturation magnetization as a function of temperature for nickel. The magnetization vanishes at T_c. The figure is adapted from [23].

1.3 Magnetic domains

The hysteretic behavior of magnetization is due to the presence of so-called magnetic domains. Within each domain, the local magnetization is saturated. These domains are separated from one another by 'domain walls'. In general, the magnetization within different domains is not parallel. A zero macroscopic magnetization as that obtained at $\boldsymbol{H} = H_c$ can be understood as a random orientation of magnetization in the individual domains resulting in an average zero magnetization. At $\boldsymbol{H} = 0$, a finite macroscopic remanent magnetization exists because the magnetization orientation in the individual domains does not cancel out. Above H_s, all the moments in every domain orient along the field resulting in a saturation magnetization M_s.

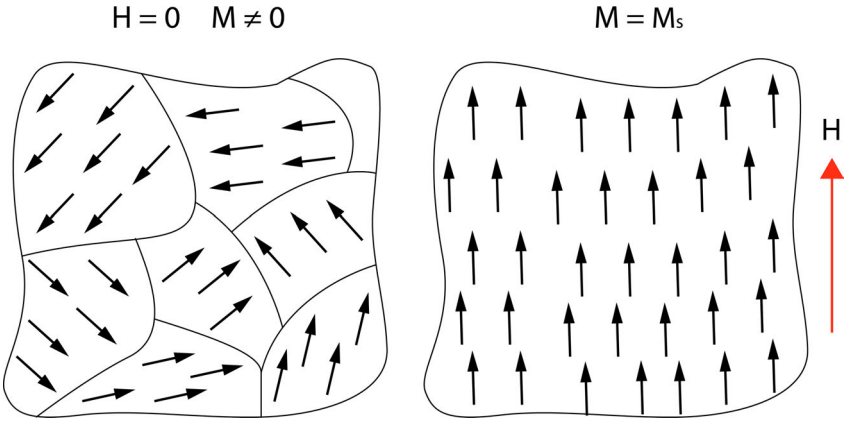

Figure 1.4: Schematic showing the magnetic domains and the spin orientations in zero and externally applied magnetic field H.

Ferromagnetic domains are formed as a compromise to minimize the overall energy of the system (E_{eff}) which is governed by the exchange energy (E_{exch}), magnetostatic energy (E_d), Zeeman energy (E_z) and the anisotropy energy (E_{anis}).

$$E_{eff} = E_{exch} + E_z + E_d + E_{anis} \tag{1.22}$$

The different energies compete with each other to orient the magnetization of a magnetic material in a certain direction. The final magnetization direction is determined by minimizing all these energy contributions described below.

1.3.1 Exchange energy

Exchange energy favors a collinear alignment of the spins. It is given by the Heisenberg Hamiltonian discussed in the previous section and depends on the relative orientation between the adjacent spins,

$$H_{exch} = -J \sum_{i<j} \boldsymbol{S_i} \boldsymbol{S_j} \tag{1.23}$$

where $\boldsymbol{S_i}$ and $\boldsymbol{S_j}$ are the neighboring spins. The sign of the exchange integral J gives the type of magnetic ordering: ferromagnetic for $J > 0$ and antiferromagnetic for $J < 0$. The exchange energy density is given by

$$E_{exch} = A(\nabla \boldsymbol{m})^2 \tag{1.24}$$

where $\boldsymbol{m} = \boldsymbol{M}/M_s$ is the magnetization unit vector and A is the exchange stiffness.

1.3.2 Magnetostatic energy

A uniformly magnetized sample generates a stray field outside the magnetic material and a demagnetizing field within itself. The strength of magnetic field generated by a dipole $\mathbf{m}$ at a distance $\mathbf{r}$ in space is given by

$$H_d(r) = \frac{1}{4\pi} \left(\frac{3\mathbf{r}\ (\mathbf{m}\ \mathbf{r})}{|\ \mathbf{r}\ |^5} - \frac{\mathbf{m}}{|\ \mathbf{r}\ |^3} \right) \tag{1.25}$$

In general, it is very complicated to solve the exact value of demagnetization field for a magnetic body. But for thin films with uniform saturated magnetization M_s perpendicular to the film's plane, the demagnetization magnetic field in the film opposes the direction of magnetization of the film and is given by $H_d = -M_s/\mu_o$. Beginning from a single domain state in Figure 1.5, magnetic domains are formed to reduce the

overall magnetic energy of the film. A competition between this magnetostatic energy and the anisotropy define the final size and shape of the magnetic domains.

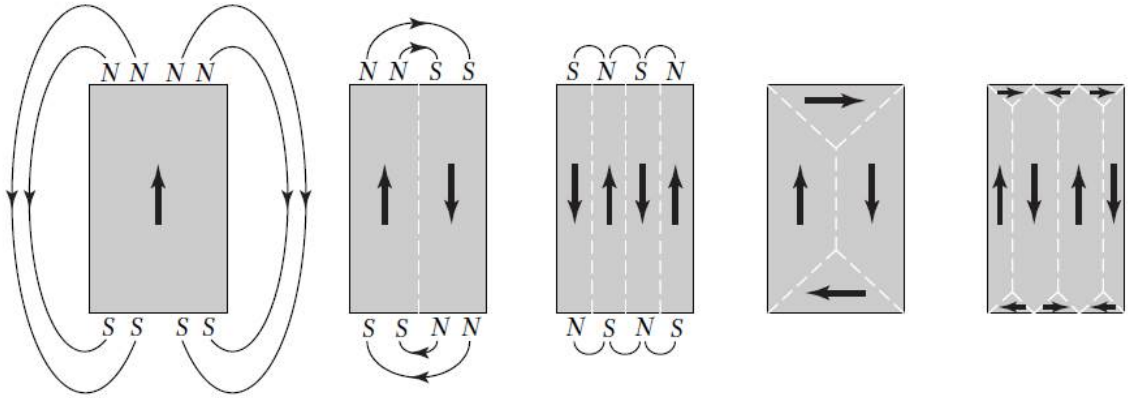

Figure 1.5: Schematic showing the origin of magnetic domains due to magnetostatic energy. The figure is adapted from [23].

1.3.3 Zeeman energy

Zeeman energy (E_z) is the potential energy of a magnetized material with volume V and magnetization $\boldsymbol{M}$ placed within an external magnetic field $\boldsymbol{H}$ and is given by,

$$E_z = -\mu_o \int \boldsymbol{M}\boldsymbol{H} dV \tag{1.26}$$

1.3.4 Anisotropy energy

Magnetic anisotropy in a ferromagnetic material preferentially orients the magnetization along certain axes known as the easy axis of magnetization. The different sources of anisotropy energy: magnetocrystalline anisotropy (E_K), shape anisotropy (E_s) and magnetoelastic anisotropy (E_{me}) are discussed below.

1.3.4.1 Magnetocrystalline anisotropy

Magnetocrystalline anisotropy results from the symmetry of the crystalline lattices and the elongated charge distribution around atoms due to the spin-orbit coupling. In an isolated atom, the electron charge distribution is spherically symmetrical which gives rise to an isotropic orbital angular momentum. However, in a crystal lattice, the electrostatic potential of the lattice affects the orbital angular momentum which is linked to the electron spin via a spin-orbit coupling. The orbital angular momentum energetically prefers certain crystal axes over others and this asymmetry is transferred

to the spin counterpart. Therefore, the magnetocrystalline anisotropy depends on the crystalline symmetry and the relative orientation of magnetization and crystal axes. For instance, in Fe with a cubic crystal, the easy axis is along [100] and the hard axis is along [111]. In the absence of crystal symmetry as in amorphous ferromagnetic materials, the magnetocrystalline anisotropy vanishes. However, polycrystalline films having randomly oriented grains may exhibit small magnetocrystalline anisotropy as the anisotropy of the individual grains averages out over macroscopic length scales. For a single domain particle with uniaxial anisotropy, the magnetocrystalline anisotropy energy is given by

$$E_K = KVsin^2(\theta) \tag{1.27}$$

1.3.4.2 Shape anisotropy

Shape anisotropy arises essentially from the demagnetization field H_d (discussed in section 1.3.2). Such long-range dipolar interactions also depend on the geometric shape of the ferromagnetic sample. This anisotropy is particularly crucial in samples with a characteristic shape such as thin films and nanowires which leads to a preferential orientation of the magnetization in the plane of the film or along the long axis of the rod, respectively.

1.3.4.3 Magnetoelastic anisotropy

A ferromagnetic material placed in a magnetic field experiences a change in its shape or dimensions. This effect is known as magnetostriction. Conversely, if a material is subjected to an applied stress, a change in the magnetization is observed, which is commonly known as 'inverse-magnetostriction' [24]. This magnetoelastic effect from inverse-magnetostriction is related to the magnetocrystalline anisotropy. Stress changes the relative distance between the ions of the lattice altering the overall lattice potential. Since the magnetization is coupled to the electrostatic lattice potential via spin-orbit coupling, magnetoelastic anisotropy is affected via external stress.
For crystalline films, the magnetoelastic anisotropy depends on the relative orientation of the applied strain to the crystal axes. In general, the magnetoelastic anisotropy energy for a crystalline system is given by

$$E_{me} = B_1(\alpha_1^2\epsilon_x + \alpha_2^2\epsilon_y + \alpha_3^2\epsilon_z) + B_2(\alpha_1\alpha_2\epsilon_{xy} + \alpha_2\alpha_3\epsilon_{yz} + \alpha_1\alpha_3\epsilon_{xz}) \tag{1.28}$$

In an polycrystalline material where the grains are randomly oriented, the magnetostriction is isotropic. The strength of the anisotropy is given by the magnetoelastic anisotropy constant K_{me} which depends on the stress σ and the magnetostriction of the material λ_s. For certain values of B_1 and B_2, the magnetoelastic anisotropy constant for polycrystalline films is given by,

$$K_{me} = \frac{3\sigma\lambda_s}{2} \tag{1.29}$$

The easy-axis of the material can either be oriented perpendicular or along the direction of the applied strain (ϵ). For positive magnetostrictive materials ($\lambda_s > 0$) under an uniaxial tensile strain ($\epsilon > 0$), the magnetoelastic anisotropy orients parallel to the direction of the strain. For the same material, a compressive strain ($\epsilon < 0$) will orient the magnetoelastic anisotropy perpendicular to the direction of the magnetization. Similarly, for negative magnetostrictive materials ($\lambda_s < 0$), uniaxial tensile and compressive strain orient the easy axis perpendicular and parallel to the direction of the strain, respectively.

1.4 Domain walls

Domain walls are the regions separating magnetic domains. Within them, the magnetization rotates continuously from the direction of magnetization of one domain to that of the other. The width of the domain walls depends on the exchange energy which prefers a parallel alignment of spins and on the demagnetization energy which prefers the formation of domains. Gradual rotation of magnetization inside a domain wall is favorable over a sudden reversal in the magnetization because of lower exchange energy. Below a certain exchange length, the exchange energy dominates over the magnetostatic energy and domain wall formation does not take place. This exchange length l_{ex} is given by,

$$l_{ex} = \sqrt{\frac{A}{\mu_o M_s^2}} \tag{1.30}$$

where A is the exchange stiffness.

1.5 Superparamagnetism

When the total size of the magnetic sample is lower than a critical value, domain formation is not energetically favorable and the material exists in a single domain

state [25–27]. The direction of the magnetization in this single domain state is given by the anisotropy of the particle. An effective uniaxial anisotropy energy (E) for an elliptical magnetic particle with volume V is given by

$$E = KVsin^2(\theta) - \mu Hcos(\alpha - \theta) \tag{1.31}$$

where K is the anisotropy constant, V is the volume of the particle, H is the external magnetic field, θ is the angle between magnetic moment and easy axis and α is the angle between the easy axis and the magnetic field. In the absence of an external magnetic field, the two energy minima for the magnetic moment corresponding to $\theta = 0°$ and $180°$ are separated by an energy barrier KV (see Figure 1.6)) [28].
Below a certain particle size, the energy generated by the ambient thermal noise overcomes the anisotropy energy barrier. In this case, the magnetization direction of the particle fluctuates spontaneously between both directions $\theta = 0°$ and $180°$. This is known as superparamagnetism [29].

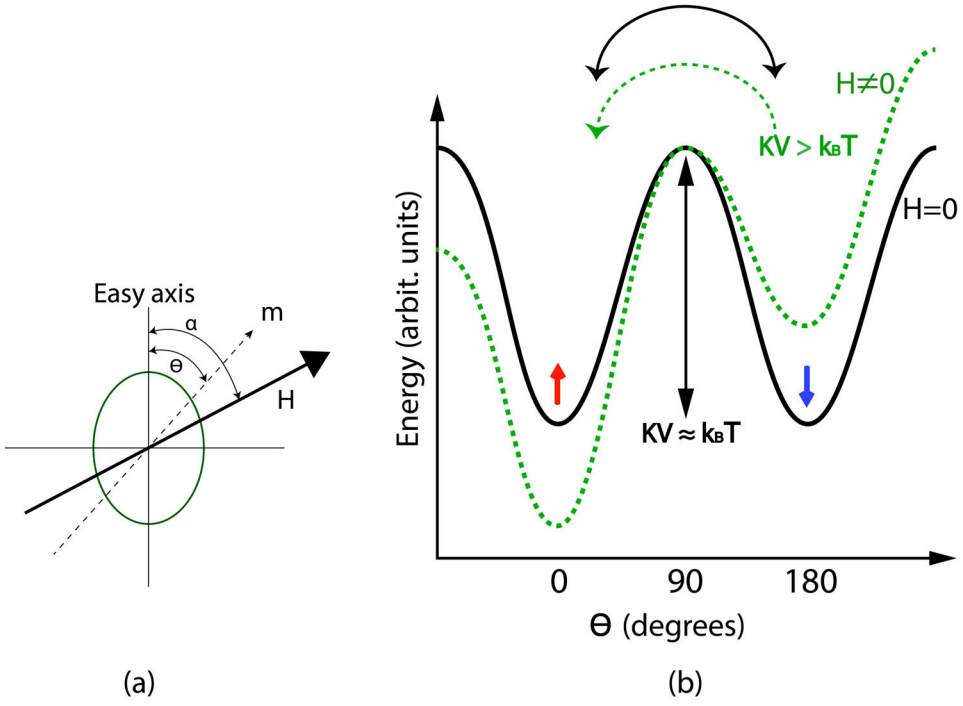

Figure 1.6: Schematic showing (a) relative orientation of easy axis, external magnetic field H and magnetic moment m of a single domain particle and (b) angular dependence of energy barrier in zero (solid black) and non-zero (dotted green) external magnetic field.

The relaxation of the magnetization is described by an Arrhenius law given by

$$M(t) = M_o \exp(-t/\tau_N) \tag{1.32}$$

where M_o is the initial magnetization and τ_N is the Neel relaxation time between the two flips. τ_N is dependent on the energy barrier and temperature and is given by

$$\tau_N = \tau_o \exp(KV/k_BT) \tag{1.33}$$

where k_B is the Boltzmann constant, T is temperature, and τ_o is material dependent ranging between 10^{-9}-10^{-10} s [28].

Assuming that the individual particles are separated from each other and have no interaction between them, the magnetization of each particle is defined independently. When the magnetization of a non-interacting system of superparamagnetic particles is measured, its observed value depends on the measurement time τ_m of the experimental technique which varies from 100 s (magnetometry experiments) to 10^{-8} s (Mössbauer spectroscopy). If $\tau_m > \tau_N$, the measured magnetization is zero as the magnetization flips randomly during the measurement time. In this state, the particles are termed to be in a 'superparamagnetic' state. If $\tau_m < \tau_N$, the magnetization of each particle is stable within the measurement time scale and a finite magnetization is measured. Such particles are termed to be in a 'blocked' state. The separation between the superparamagnetic and the blocked state is defined by the blocking-temperature T_b ($\tau_m = \tau_N$) and is given by,

$$T_b = \frac{KV}{k_B ln(\tau_m/\tau_o)} \tag{1.34}$$

Below T_b, the thermal energy is low and the magnetization of each particle is frozen with respect to the time scale of the measurement.

On applying a magnetic field, the energy barrier increases for the direction parallel to the field while it decreases for the anti-parallel one. Consequently, the magnetization of the particle is constrained to the magnetization direction with the lower energy as shown in Figure 1.6. When a magnetic field is applied in a superparamagnetic state, the magnetization orients along the magnetic field and the particles behave as a typical paramagnet. If the magnetic field is applied while cooling below T_b (field cooling), the particles are blocked with magnetization oriented along the field direction. In case of cooling in zero magnetic field (zero field cooling), the particles are blocked in a random orientation with small net magnetization. On the other hand, above T_b, superparamagnetic behavior exists with zero magnetization in the absence of magnetic field.

At a constant temperature T_o and a typical $\tau_m = 100$ s, the critical volume of the particles below which the particles exist in a superparamagnetic state is given by,

$$V_c \approx \frac{25 k_B T_o}{K} \tag{1.35}$$

For a particle with constant volume V_o and a typical $\tau_m = 100$ s, T_b is given by,

$$T_b \approx \frac{K V_o}{25 k_B} \tag{1.36}$$

The previous section considered a system of non-interacting particles. However, if the particles are brought close enough, inter-particle interaction affects the macroscopic magnetic properties of the system. The anisotropy of the individual particles is modified by the interaction which alters the energy barrier. The total free energy of the interacting system is then considered a relevant parameter rather than the energy barrier of a single particle. Different types of interactions between the particles can occur: dipolar, exchange interaction, RKKY (Rudermann-Kittel-Kasuya-Yosida) and super-exchange [30]. It is rather difficult to comprehensively study the effect of these interactions in real systems as the resultant effect is a convolution from different interactions, size, shape, anisotropy axes and surface effects of the system [28].
However, it has been observed that inter-particle interactions can induce a 'superferromagnetic' ordering in a concentrated system at a critical temperature which otherwise would have been 'superparamagnetic' if the particles were non-interacting [31]. This superferromagnetic ordering is characterized by a long-range ferromagnetic ordering of the 'super-spin' of the particle alike to the microscopic coupling of spins in ferromagnetic systems. The inter-particle interactions induce a stronger anisotropy in the particles which lead to magnetic ordering between them [32].

1.6 Ferrimagnets

A ferrimagnetic system is composed of two or more different ions that are antiferromagnetically coupled to each other. Similar to ferromagnets, they also possess a spontaneous magnetization and T_c above which they become paramagnetic. Some examples of natural ferrimagnets include magnetite Fe_3O_4, iron garnets like $Y_3Fe_5O_{12}$, and mineral spinel $MgAl_2O_4$. In this thesis, the experiments are performed on rare-earth transition-metal (RE-TM) alloys with RE = Tb and TM = Fe where the two sublattices of RE and TM are anti-ferromagnetically coupled to each other. Tb is a RE heavy metal with more than half filled $4f$ orbital and Fe is a $3d$ transition metal. Tb exhibits an anti-ferromagnetic coupling with Fe ($J_{FeTb} < 0$) as known for heavy RE-TM

alloys [33]. A strong coupling between nearby Fe atoms leads to an almost collinear orientation of their magnetization ($J_{FeFe'} > 0$). Tb ($J_{TbTb'} > 0$), on the other hand has a weak exchange coupling ($J_{TbTb'} << J_{FeFe'}$) and a strong distribution of local anisotropy resulting in a fanning cone of Tb moments [33, 34]. This behaviour is shown in Figure 1.7 displaying angular distribution γ_{Fe} and γ_{Tb} of Fe and Tb moments [35]. The magnetization of the two individual sublattices varies with temperature. Depending on their composition, RE-TM ferrimagnets can exhibit a magnetization compensation temperature T_M where the net magnetization of the RE and TM sublattices cancel each other.

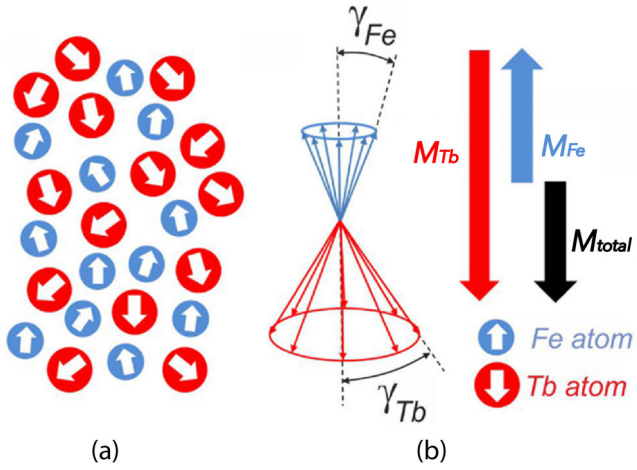

Figure 1.7: (a) Antiferromagnetically coupled distribution of Fe and Tb moments in amorphous TbFe film. (b) The behavior of Fe and Tb moments showing the fanning cone. This figure is adapted from [35].

The net magnetization $\boldsymbol{M}_{total}$ is a sum of magnetization $\boldsymbol{M}_{Fe}$ and $\boldsymbol{M}_{Tb}$ arising from Fe and Tb moments, respectively. Above T_M, $\mid \boldsymbol{M_{Fe}} \mid > \mid \boldsymbol{M_{Tb}} \mid$ and the net magnetization aligns in the direction of Fe moments. In this state, Fe is the dominant sublattice. Similarly, below the T_M, $\mid \boldsymbol{M_{Fe}} \mid < \mid \boldsymbol{M_{Tb}} \mid$ and Tb is the dominant sublattice as the net magnetization of the film is parallel to Tb moments. The T_M is dependent on the composition of the alloy and the thickness of the film [35]. Therefore, by varying the alloy composition or film thickness, one can tune the position of T_M and choose the dominant sublattice at room temperature.

1.7 Ferroelectricity

Similar to ferromagnets, ferroelectric materials exhibit a spontaneous ferroelectric polarization $\boldsymbol{P}$ that can be switched via external electric field $\boldsymbol{E}$. Ferroelectrics display a

hysteretic behavior of polarization with electric field analogous to ferromagnetic hysteresis as shown in Figure 1.2, with ferroelectric equivalent saturation polarization P_s, remnant polarization P_R, and coercive field E_c. While ferromagnetism arises from electron's spin angular momentum and exchange interaction, ferroelectricity is related to the structural symmetry of the crystal. Above a critical Curie temperature T_c, ferroelectrics lose their spontaneous polarization and become paraelectric.
All ferroelectric materials are piezoelectrics like $BaTiO_3$ (BTO) but not all piezoelectric are ferroelectrics with quartz as counter example. The polarization of a piezoelectric material can be written as:

$$\boldsymbol{P} = \boldsymbol{\sigma} d + \boldsymbol{E}\chi' \tag{1.37}$$

where $\boldsymbol{\sigma}$ is the stress, d is the piezoelectric constant, $\boldsymbol{E}$ is the electric field vector and χ' is the dielectric susceptibility. An applied stress $\boldsymbol{\sigma}$ in the crystal alters the electric polarization as shown in Figure 1.8 and conversely, an electric field $\boldsymbol{E}$ applied to the crystal generates strain.

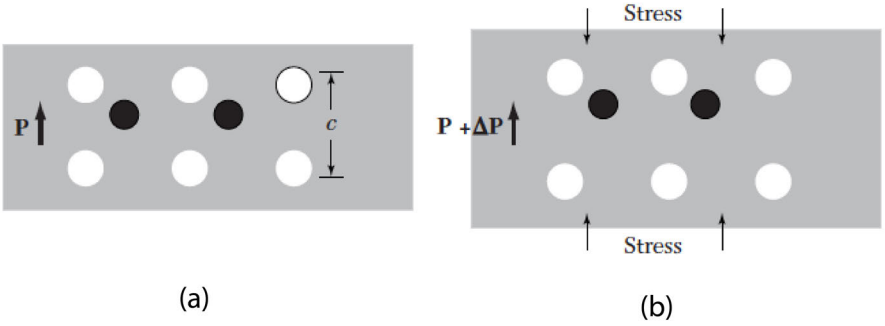

Figure 1.8: (a) Ferroelectric crystal with zero strain and spontaneous polarization $\boldsymbol{P}$. (b) Stress induces a polarization ΔP in the ferroelectric crystal. Bright and dark circles represent the atoms arranged in a crystal lattice. The figure is adapted from [23].

Ferroelectricity can originate from numerous sources. It can be due to lone pair as in $BiFeO_3$ [36], due to charge ordering as in $TbMn_2O_3$ [37], geometric ferroelectricity as in hexagonal magnetites [38] or covalent bonding between $3d$ transitional metal and oxygen as in $BaTiO_3$. Since this thesis concentrates on the control of magnetic properties of polycrystalline Fe deposited on BTO single crystal substrate, the ferroelectric properties of BTO are described in detail.

1.7.1 Barium Titanate

Barium Titanate is a perovskite oxide which exhibits ferroelectric, piezoelectric and ferroelastic properties. The centrosymmetric cubic perovskite ABO_3 structure is shown in Figure 1.9.

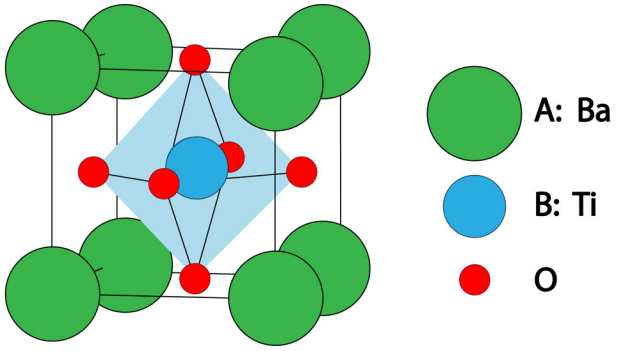

Figure 1.9: Schematic showing the cubic perovskite structure ABO_3 of barium titanate.

BTO has a T_c of 393 K, above which it possesses a centrosymmetric cubic structure and exhibits paraelectric properties. Below T_c, BTO sustains ferroelectric properties while it undergoes multiple phase transitions (tetragonal (300 K), orthorhombic (250 K) and rhombohedral (170 K)) causing structural changes in the unit cell as temperature decreases (see Figure 1.10) [39–41]. The unit cell parameters change from: a = b = c = 4.001 Å in the cubic phase to c = 4.035 Å, a = b = 3.991 Å in the tetragonal phase to a = b = 4.018 Å, c = 3.987 Å in the orthorhombic phase to a = b = c = 4.004 Å in the rhombohedral phase. Each phase transition results from a distortion in the crystal lattice resulting in an elongation of the cell along a certain axis. Such distortions are associated with a relative shift in the position of ions resulting in an electric polarization along the direction of lattice elongation.
In the tetragonal phase, the Ti^4+ ion is displaced in the opposite direction with respect to the O^2- ions resulting in an electric polarization due to a separation of positively charged Ti and negatively charged O octahedron. In tetragonal phase, there are three equivalent directions for lattice elongation (edges of a cell $[100]_{pc}$, $[010]_{pc}$, and $[001]_{pc}$ where '*pc*' stands for a pseudo-cubic notation) which leads to 6 possible polarization directions. The polarization of BTO is around 0.26 C/m^2 at room temperature and the lattice elongation is around 1.1% (c-a/a) [41].

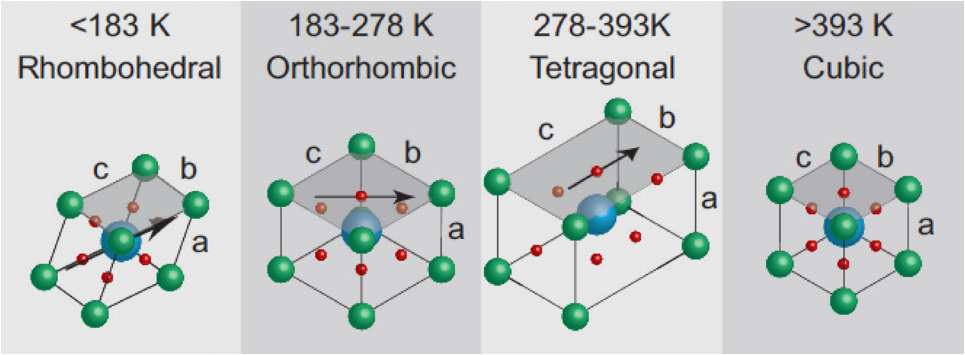

Figure 1.10: Schematic showing the structure of the unit cells of $BaTiO_3$ as a function of temperature. The arrows indicate the direction of the displacement of the Ti ion and the net polarization. The figure is adapted from [39]

The second phase transition occurs at 278 K where the BTO structure changes from tetragonal to the orthorhombic phase [40]. The long-axis of lattice elongation and the polarization direction rotates from $[100]_{pc}$ in the tetragonal phase to face diagonal $[110]_{pc}$ in the orthorhomic phase (Figure 1.10). The third phase transition occurs at 183 K where the structure changes from orthorhombic to rhombohedral phase [40]. The polarization orients along the body diagonal $[111]_{pc}$ in the rhombohedral phase. For orthorhombic and rhombohedral phases, there are 12 and 8 possible polarization directions that correspond to the face diagonals and body diagonals of the crystal, respectively.

1.7.1.1 Ferroelectric domains

Like ferromagnets, ferroelectrics also form domains with uniformly polarized regions which are formed as a consequence of depolarizing field to minimize the electrostatic energy. The orientation of the ferroelectric polarization corresponds to the direction of the elongation of the unit cell. For a BTO $[001]_{pc}$ single crystal in the tetragonal phase, the domain in which the polarization direction orients out-of-plane are termed as c domains corresponding to the lattice elongation along $[001]_{pc}/[00\bar{1}]_{pc}$. The in-plane domains are of two types: a_1 and a_2 with ferroelectric polarization and lattice elongation along $[010]_{pc}$ and $[100]_{pc}$, respectively. The cell parameter of BTO $[001]_{pc}$ single crystal are: c = 4.035 Å, a = b = 3.991 Å. A large uniaxial tensile ferroelastic strain c-a/a = 1.1% exists along $[010]_{pc}$ and $[100]_{pc}$ for a_1 and a_2 domains, respectively [42]. The c domain, on the contrary, is isotropic and does not experience any in-plane strain.

In the tetragonal phase, three 90° domain pattern exist: a_1-a_2, a_1-c, and a_2-c. The first in-plane domain configuration a_1-a_2 domain pattern is shown in Figure 1.11(a). Ferro-

electric domain walls are aligned at 45° with respect to the polarization directions of a_1 and a_2 along $[\bar{1}10]_{pc}$. The polarization direction in a_1-a_2 domains orients head-to-tail to minimize the charge accumulation at the interface. An equivalent domain configuration of a_1-a_2 can also exist with domain walls along $[110]_{pc}$. The second 90° domain, the a_1-c domain pattern comprises alternating in-plane a_1 and out-of-plane c domains as shown in Figure 1.11(c). The domain wall orients along $[100]_{pc}$ making an angle of 90° with respect to both a_1 and c polarization directions. An inclination of about 0.5° on the topography exists at the domain wall because of the mismatch between the out-of-plane lattice parameter of a_1 and c domains. The polarization direction in a_1-c domains also orients head-to-tail to minimize the charging at the domain wall. Similar to a_1-c pattern, another a_2-c pattern is also possible where the domain wall orients along $[010]_{pc}$ as shown in Figure 1.11(c). Such multi-domain patterns have been experimentally observed by several groups [8, 43–45].

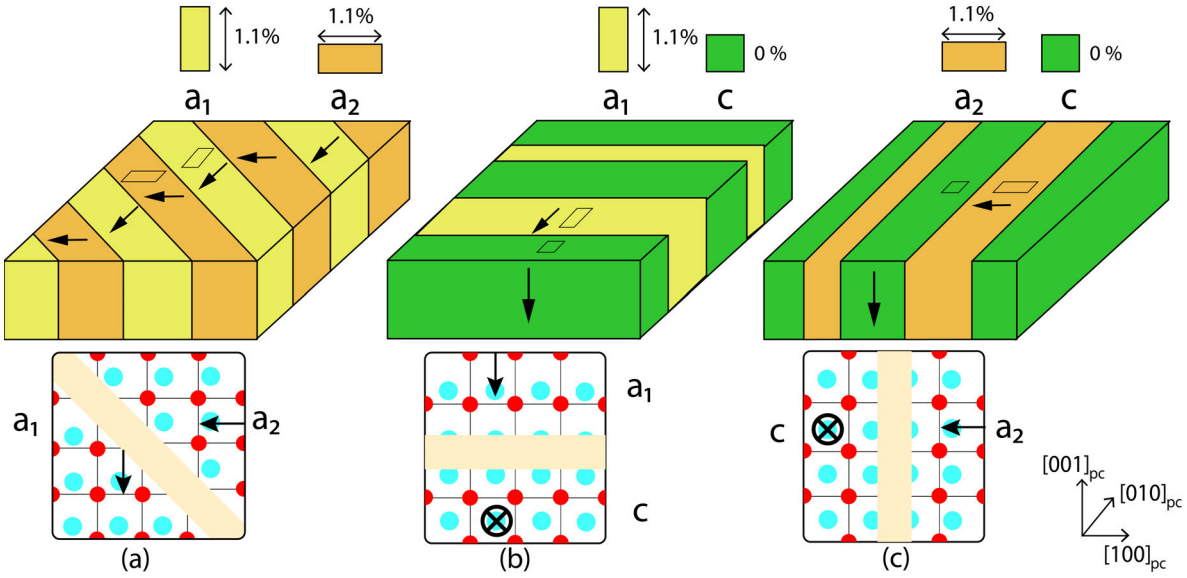

Figure 1.11: Schematic showing the domain pattern in $BaTiO_3$ (a) a_1-a_2 domain (b) a_1-c domain (c) a_2-c in the tetragonal phase. The lower panel shows the top-view of the structural changes at the domain wall. The red and the blue circles are Ba and Ti ions, respectively. The black arrows represent the local polarization direction.

Figure 1.12 shows the ferroelectric domain evolution and its position (red dots) on the corresponding hysteresis loop measuring the net macroscopic polarization with an out-of-plane electric field for a BTO single crystal. Beginning from an a_1-a_2 pattern at the origin (Figure 1.12(a)), the application of an out-of-plane electric voltage transforms the domain pattern into a_1-c pattern (Figure 1.12(b)). Here, the a_1 and a_2 domains experience a uniaxial compressive strain along $[010]_{pc}$ and $[100]_{pc}$, respectively to convert

to the c domain. Some of the a_2 domain convert to a_1 after experiencing compressive and tensile strain along $[100]_{pc}$ and $[010]_{pc}$, respectively. Further increasing the voltage decreases the a_1 domain fraction and the BTO eventually evolves into a full c domain (Figure 1.12(c)) [8]. On decreasing the voltage, the domain pattern does not go back to a_1-a_2 but remains in a_1-c state (Figure 1.12(d)). The hysteresis loop in Figure 1.12(e) shows the position of different domain patterns (a-d) marked by the red dots. Figure 1.12(f) shows a schematic of the different domain transformations (a_1 to c, a_2 to c, and a_2 to a_1) after application of an out-of-plane voltage.

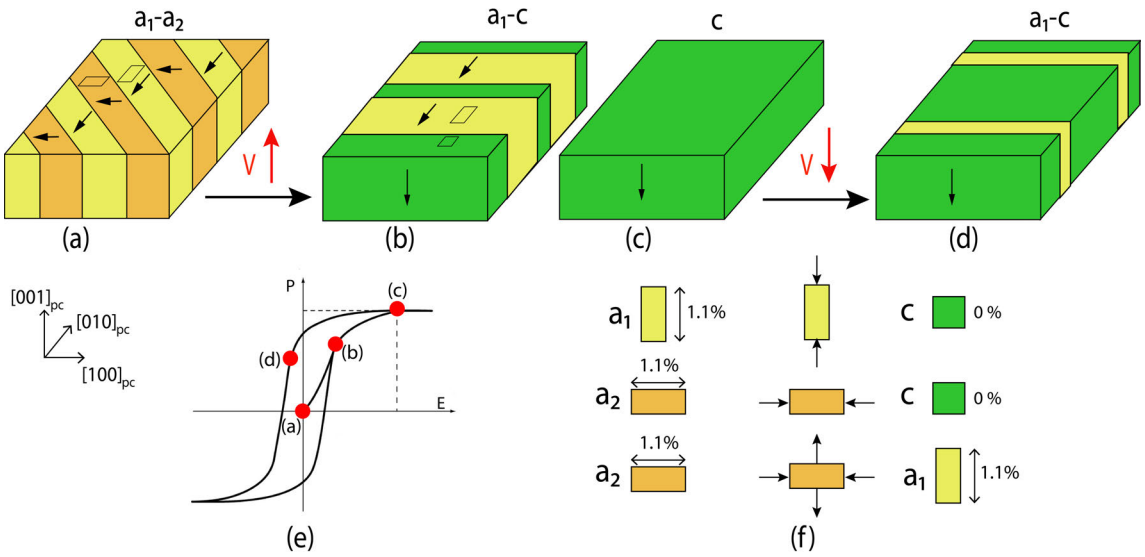

Figure 1.12: Schematic showing the (a) initial a_1-a_2 FE domain pattern of BTO that changes to (b) a_1-c and eventually to (c) c domain after application of an out-of-plane voltage. On decreasing the voltage, the domain pattern relaxes to an a_1-c pattern. (e) Hysteresis loop showing the position of different domain patterns marked by the red dots in a macroscopic P vs E measurement. (f) Schematic showing the different transformations (a_1 to c, a_2 to c, and a_2 to a_1) and the applied strain directions when the a_1-a_2 pattern in (a) converts to a_1-c (b).

1.8 Multiferroicity

Multiferroics materials exhibit more than one ferroic order parameter simultaneously [46]. The most technologically appealing multiferroics are materials possessing magnetic and ferroelectric ordering with two order parameters: magnetization and electric polarization [47]. If the magnetoelectric (ME) coupling is strong, their magnetic and electric properties can be controlled by external electric and magnetic fields. Such materials are extensively studied because of their immense technological potential in

devices such as electrical transformers, sensors, data storage media and integrated circuits [48–50]. The potential application of a single material with both magnetic and ferroelectric properties has resulted in numerous research efforts. However, the existence of magnetic and ferroelectric properties have contradictory requirements, thus preventing the co-existence of the two ferroic orders at first sight [51]. Conventional ferroelectric systems of transitional metals have d^0 electronic configuration whereas magnetism is mediated by partially filled d orbitals. In addition, most ferroelectrics are insulators in nature since conductive materials would result in charge flow instead of a resultant polarization. Ferromagnets, on the other hand, are conductive due to partially filled d orbitals. Even with these restrictions, single phase multiferroics exist but are scarce. Coexistence of magnetism and ferroelectricity is plausible when the ferroic orders have different origins (Type 1 multiferroics) such as geometric ferroelectric $YMnO_3$ [38] and lone-pair ferroelectrics $BiMnO_3$ [52]. A consequence of the different origin for magnetic and electric ordering is a ME coupling where the transition temperatures do not coincide. $BiFeO_3$ is another example of Type 1 multiferroic that posseses multiferroicity at room temperature with ferroelectricity and anti-ferromagnetism upto $T_c = 1100$ K and $T_N = 640$ K, respectively [36]. Another possiblity of coexistence arises when the ferroelectric order in a material originates via magnetism by breaking space-inversion symmetry (Type 2 multiferroics) as observed in spiral magnets such as $TbMnO_3$ [53, 54]. In general, single-phase multiferroic materials exhibit weak ME coupling and only at low temperatures.

Despite all the research efforts, the realization of a single-phase multiferroic displaying strong and robust ME coupling with ferromagnetic ordering at room temperature is still missing [55, 56]. A promising alternative to single-phase multiferroics are artificial multiferroic heterostructures made of two different components, one having ferroelectric order and the other magnetic order. Unlike single-phase multiferroics, the ME coupling between magnetic and ferroelectric orders in heterostrucrures is not intrinsic and arises via proximity of the two materials. The strength of the ME coupling depends on the individual components. This allows engineering of artificial multiferroic systems with substantial ME coupling and T_c close to or above room temperature. The first multiferroic heterostructure was crafted from ferroelectric $BaTiO_3$ and ferromagnetic $CoFe_2O_4$ in 1972 by Van Suchtelen [57]. Thin film heterostructures are more promising than bulk composites as the two magnetic and ferrolectric phases at the interface are in direct contact with each other resulting in a stronger ME coupling. The potential of the multiferroic thin films lies in the devices such as sensors, high-density storage devices and spintronics.

Chapter 2

X-ray spectroscopy

X-ray spectroscopy has been widely used to study thin film systems, interfaces, and heterostructures. Depending on the spectroscopic technique, magnetic, electronic and/or crystallographic information can be extracted by studying the interaction between the incident radiation and the matter. The experiments in this thesis are performed with soft X-rays. In particular, X-ray Absorption Spectroscopy (XAS) has been used to study chemical properties of the thin films and artificial heterostructures of TbFe and Fe/BTO, respectively. X-ray Circular Magnetic Dichroism (XMCD) has been primarily used to probe the magnetic contrast for investigating magnetic properties of TbFe and Fe thin films. Section 2.1 provides a brief overview to absorption spectroscopy. The basic principles of XAS and XMCD are discussed in section 2.2 and 2.3, respectively.

2.1 Absorption spectroscopy

The interaction between an atom and radiation is given by the Hamiltonian H,

$$H = H_P + H_R + V_I \tag{2.1}$$

where H_P, H_R and V_I are the Hamiltonians of the particle, photon, and the particle-photon interaction, respectively. Within the time-dependent perturbation theory [58], the interaction V_I can be treated as a perturbation to the Hamiltonian $H_o = H_P + H_R$. On absorbing a photon, the electron is excited from the initial state i to the final state f with the corresponding eigenstate $|\phi_i\rangle$ and $|\phi_f\rangle$, respectively. The absorption cross-section σ_{abs} is defined by dividing the transition probability per unit time of a transition (from the initial state $|\phi_i\rangle$ to the final state $|\phi_f\rangle$) by the incoming photon flux I_{ph}.

$$\sigma_{abs} = \frac{\sum_f W_{i\to f}}{I_{ph}} \tag{2.2}$$

Here, $W_{i\to f}$ is the probability of transition per unit time from $|\phi_i\rangle$ to $|\phi_f\rangle$, and is given by the Fermi Golden rule,

$$W_{i\to f} = \frac{2\pi}{\hbar}|\langle\phi_f|T_I|\phi_i\rangle|^2\delta(E_f - E_i - \hbar\omega) \tag{2.3}$$

where the transitional operator T_I, associated with V_I contributing to the absorption events, ω is the frequency of the photon, and E_i and E_f are the energies of the electron in the state $|\phi_i\rangle$ and $|\phi_f\rangle$, respectively.

The electric dipole-approximation is used to further simplify equation 2.3. The so-called 'dipole-selection rules' appear when the matrix element in equation 2.3 is calculated according to the Wigner-Eckart theorem. The dipole-selection rules restrict the allowed electronic transitions so that the quantum numbers between the initial state $|\phi_i\rangle$ and final state $|\phi_f\rangle$, can only differ by,

$$\Delta j = 0, \pm 1; \Delta l = \pm 1, \Delta m_l = 0, \pm 1, \Delta m_s = 0 \tag{2.4}$$

When the photon energy $\hbar\omega$ is equal to the $E_f - E_i$, the delta function term in equation 2.3 leads to a resonance in absorption. At this particular photon energy (commonly known as the absorption edge), the absorption is maximum and corresponds to the excitation from the initial core level electron to the final state in the valence band. The absorption of a photon results in the formation of a core-hole which is highly unstable with a lifetime of about 1 fs [59]. The de-excitation process of the core-hole can take a radiative fluorescent path or a non-radiative Auger decay path. In fluorescence, a different electron with a higher energy (in the valence band) fills the core hole and the energy difference is emitted as electromagnetic radiation (photon). On the other hand in Auger decay, the photon energy emitted from the filling of a core hole by a valence electron excites a third valence (Auger) electron. While passing through the solid, the primary Auger electrons experience multiple inelastic scattering initiating a low energy secondary electron cascade.

Most often, instead of measuring the absorption in transmission, electron yield detection mode is used where all the electrons with different energies escaping the sample are collected ranging from direct photoelectrons, down to low energy secondary electrons. Depending on the type of technique and information to be extracted, either secondary, or Auger, or direct photoelectrons are used for spectroscopy.

2.2 X-ray absorption spectroscopy (XAS)

Within the soft X-ray energy regime, the resonant energies of L-edges of the $3d$ transition metals ($2p$ to $3d$ transitions) and M-edges of the rare-earth metals ($3d$ to $4f$ transitions) are accessible. XAS spectra are recorded by sweeping the photon energy in steps across the absorption edges of the element (in the sample) in consideration. Besides element selectivity, XAS also offers information about the oxidation state and local chemical environment by analyzing the spectral shape and peak position of the absorbing element. Figure 2.1(a) shows an example of XAS spectra measured at the $L_{3,2}$-edge of Fe and Fe-oxides for different materials: Fe metal, FeO, Fe_2O_3, and α-Fe_3O_4 [60]. The spectral features for all the four Fe compounds are different (Figure 2.1(b)) because of their different oxidation states. This technique is extremely advantageous in probing the samples comprising different elements or a sample with a heterogeneous spatial distribution.

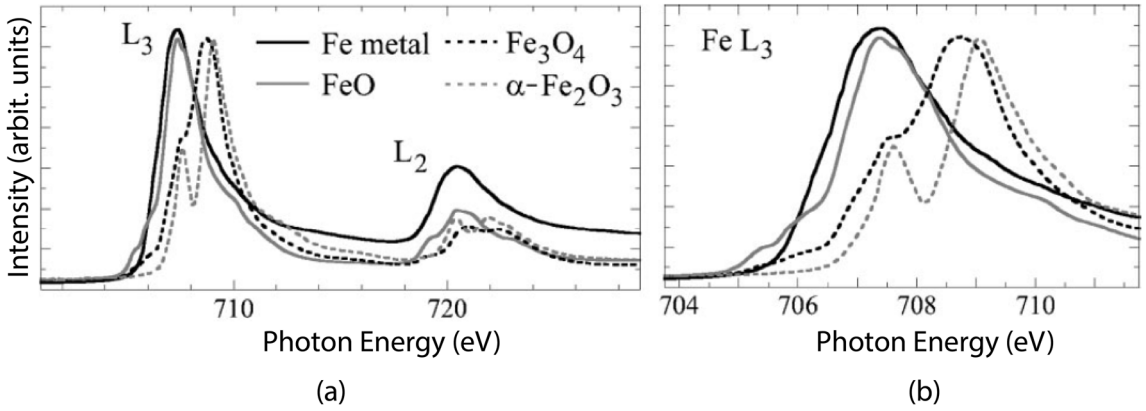

Figure 2.1: (a) XAS spectra of Fe metal, FeO, Fe_2O_3, and α-Fe_3O_4 at L_3 and L_2-edge. (b) XAS spectra showing the spectral features at L_3 Fe edge. The figure is adapted from [60].

Figure 2.2(a) shows the XAS spectra of Fe recorded with two circular X-ray polarization $c+$ and $c-$ displaying the intensity as a function of the incident photon energy. The difference in the resonance at the $L_{3,2}$ absorption edges from the two circular X-ray polarization plotted in the lower panel of Figure 2.2(a) is the consequence of the dichroic effect discussed in the next section.

2.3 X-ray Magnetic Circular Dichroism (XMCD)

The phenomenon of XMCD has been widely used to study magnetic properties of magnetic materials. Being derived from XAS, XMCD takes advantage of spin-dependent

absorption process of circularly polarized X-rays [61–63]. Here, the term 'dichroism' refers to a difference in the absorption intensities by incident circularly polarized photons of opposite polarization. XMCD can be understood by so-called 'two-step' model initially developed by Stöhr and Wu *et al.* [64]. In the first step, the photon transfers its angular momentum to the electron. Circularly polarized $c+$ and $c-$ photon helicities impart opposite angular momentum, $\hbar$ and $-\hbar$, respectively to the electrons. If the excited photo-electron originates from a spin-orbit split level such as $p_{3/2}$, the angular momentum from the photon is transferred to the total angular momentum $\boldsymbol{J} = \boldsymbol{L} + \boldsymbol{S}$ which is partially transferred to the spin via spin-orbit interaction [65]. The spin moment of the photo-electrons is either parallel or anti-parallel to the beam direction depending on the helicity of the photons and the spin-orbit interaction at the core level (for $2p_{3/2}$ and $2p_{1/2}$ levels, the total angular momentum is given by $(L+S)$ and $(L-S)$, respectively). Therefore, the absorption of a circularly polarized photon by a spin-orbit split core level electron generates an internal spin-polarization.

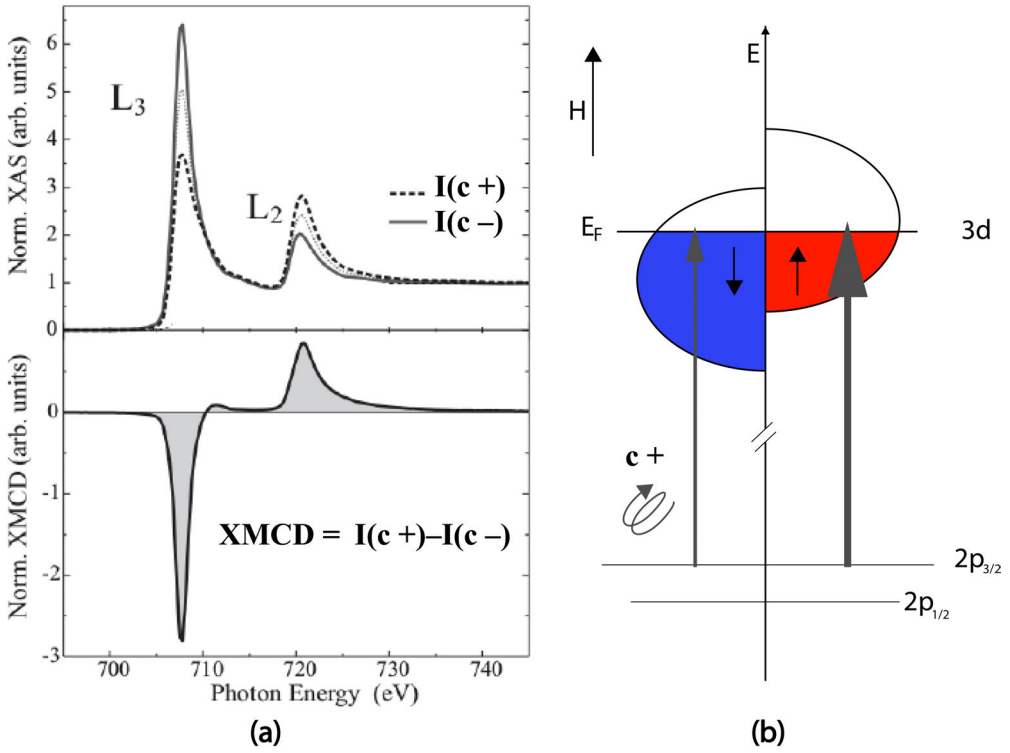

Figure 2.2: (a) Schematic showing normalized XAS spectra recorded by opposite circular X-ray polarization ($c+$ and $c-$) and the corresponding XMCD signal in the lower panel. (b) Schematic showing excitation of core $2p$ electrons to the $3d$ valence empty states on absorption of circularly polarized photons.

In the second step, the spin polarization is detected by the valence band of the magnetic materials. In non-magnetic materials, the density of states for spin-up and spin-down

states at the Fermi level is equal and the electrons excited with opposite circular helicity are absorbed in a similar way. Ferromagnetic materials have an imbalance of spin-up and spin-down states at the Fermi level which defines the net magnetization. Spin-flips in the transition are forbidden due to dipole-selction rules given in equation 2.4, implying that the spin-up and the spin-down core electrons will fill the spin-up and spin-down valence states, respectively. Therefore, the imbalance in the valence shell acts as a detector for the excited core electrons. The absorption intensity due to excitation of spin-up/spin-down core electrons is proportional to the number of available empty up/down valence states. The difference between the absorption intensity by two helicities ($I(c+) - I(c-)$) at a particular absorption edge is directly proportional to the imbalance between spin-up and spin-down electrons and is therefore magnetization sensitive. For a fixed magnetization of the sample, the absorbed intensity is different for the two opposite circular polarization of the X-ray. Conversely, for a fixed photon polarization the absorption of the circular polarization of the X-rays is magnetization dependent [62].
Figure 2.2(a) shows the different absorption intensities $I(c+)$ and $I(c-)$ for Fe $L_{3,2}$-edges. The XMCD signal is given by,

$$XMCD = I(c+) - I(c-) \tag{2.5}$$

As observed in the lower panel of Figure 2.2(a), the XMCD signal has opposite sign at L_3 and L_2 edges due to the opposite spin-orbit coupling at the two absorption edges. XMCD is a very powerful technique which besides allowing an element selective magnetic contrast, enables to extract the individual contribution from the orbital and the spin components. This is carried out by applying the so-called 'sum-rules', initially given by [66, 67] relate the experimentally observed features in the XMCD spectra to the spin ($m_s = -2\frac{\mu_B}{\hbar}\langle S_z\rangle$) and orbital ($m_l = -\frac{\mu_B}{\hbar}\langle L_z\rangle$) component of the total magnetic moment.

Chapter 3

Magnetic imaging via X-ray Photoemission Electron Microscopy

X-ray Photoemission Electron Microscopy (XPEEM) is a well-established surface sensitive imaging technique that has been widely used to study magnetic systems and their interactions [68, 69]. The initial photon sources in the 1930s were mostly limited to UV light. However, the availability of high energy synchrotron radiation in the soft X-ray regime has facilitated this technique to become element selective. By tuning the photon energy to the absorption edge of the element of interest, one can obtain element selective information. The imaging in XPEEM is carried out by collecting the low-energy secondary electrons created by the in-elastic scattering of Auger electrons. The mean-free path of the secondary electrons limits the information depth of the technique to a few nanometers below the surface. XPEEM provides a high spatial resolution with magnetic contrast (by XMCD) and chemical sensitivity (by XAS) which is extremely suitable to study magnetism in thin films and interfaces. Section 3.1 discusses the technical aspects of the imaging via XPEEM. Section 3.2 provides a brief outlook on the various contrast mechanisms active in the imaging. Section 3.3 and 3.4 focuses on the femtosecond laser set-up and the various sample holders used in experiments performed in this thesis, respectively. Section 3.5 discusses the data acquisition and analysis.

3.1 Technical aspects

The space resolved spectroscopic and magnetic characterization experiments described within this thesis were performed with the XPEEM set-up (based on an Elmitec III instrument) stationed at the UE 49PGMa beamline at synchrotron radiation facility

BESSY-II of the Helmholtz-Zentrum Berlin [70]. The incoming photon energy can be varied between 80 eV to 1800 eV with a spectral resolution of approximately 10^4 at 700 eV and full polarization control of photons, i.e. linear, elliptical, and circular helicity. The photon flux obtained at the surface of the sample ranges between 10^{11} to 10^{13} ph/s per 100 mA ring current. This instrument is operated in an ultra-high vacuum chamber with a pressure of about 10^{-10} mbar. The X-rays are incident at a grazing angle of 16° to the sample's surface. The X-ray beam size on the sample is focused to about 20 μm (horizontal) $\times$10 μm (vertical).

PEEM uses secondary electrons in the electron yield for magnetic imaging and spectroscopy [69]. The secondary electrons originate from a shallow layer below the sample surface and its intensity is proportional to the absorption coefficient [71]. On absorption of X-rays, the electron emission depends on the local work function, topography, and chemistry of the sample. The emitted electrons from different regions of the sample are passed through an electron-optical column and magnetic or electrostatic electron lenses. A lateral electron distribution is imaged and projected on a fluorescence screen. Figure 3.1 shows a schematic of XPEEM consisting of an electron-optical column with an objective lens, a contrast aperture, some intermediate lenses, an energy analyzer, a projective lens, an image intensifier and a screen. The sample is kept at a high voltage of 10 kV close to the objective lens which is capable of accepting electrons from a large solid angle. The electrostatic potential between the sample and the lens accelerates the emitted electrons into the microscope. Due to chromatic aberration, the electrons originated from a particular sample position but with different kinetic energy might end up at different positions on the screen. The contrast aperture in the back-focal plane of the objective lens reduces the aberration and improves the lateral resolution by controlling the intensity of the transmission into the column. The size of the aperture is selected according to the experiment. A small sized aperture increases the spatial resolution but decreases the transmitted intensity. The 180° hemispherical energy analyzer acts as a band-pass filter to select electron trajectories with a narrow spread of kinetic energies and further reduces the chromatic aberration. The electrons are selected with an energy resolution of less than 0.2 eV. The projective lens finally magnifies the signal on a multi-channel plate which creates a corresponding lateral image of the secondary photoelectron intensity on a screen. A CCD camera transfers the obtained image to the computer for further analysis. The XPEEM at the SPEEM station provides a high spatial resolution of about 25 nm. A picture of the PEEM set up is shown in Figure 3.1 (b).

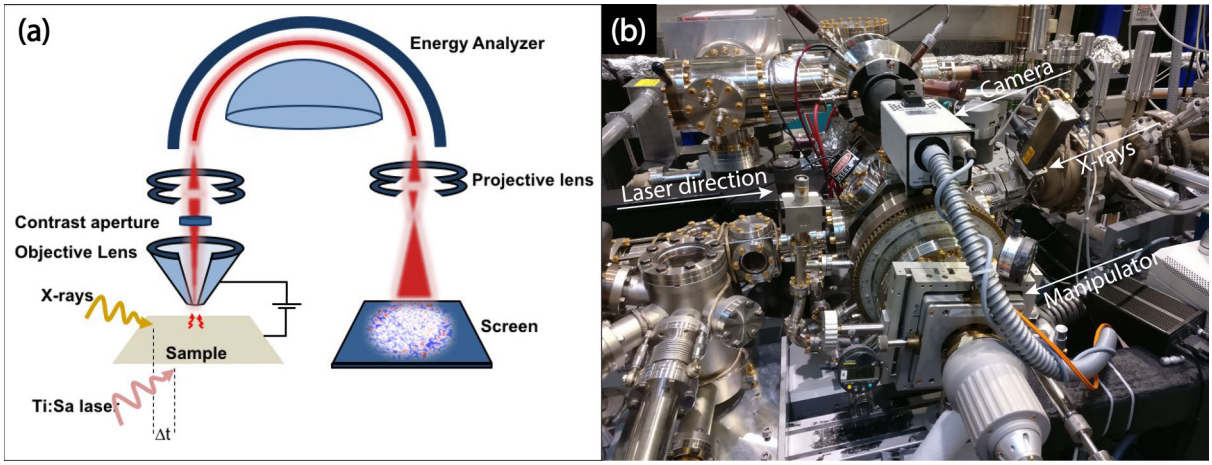

Figure 3.1: (a) Schematic and (b) picture showing the PEEM set-up at the SPEEM station at BESSY-II.

A preparation chamber (Figure 3.2(a)) is attached to the XPEEM set-up and vacuum connected to allow the transfer of the sample to the XPEEM chamber without breaking the vacuum. It is equipped with several evaporators where thin films can be deposited on substrates mounted on the sample holder. The growth rate of the thin films is calibrated by a quartz balance prior to deposition. A schematic of the PEEM instrument at the SPEEM station is shown in Figure 3.2(b).

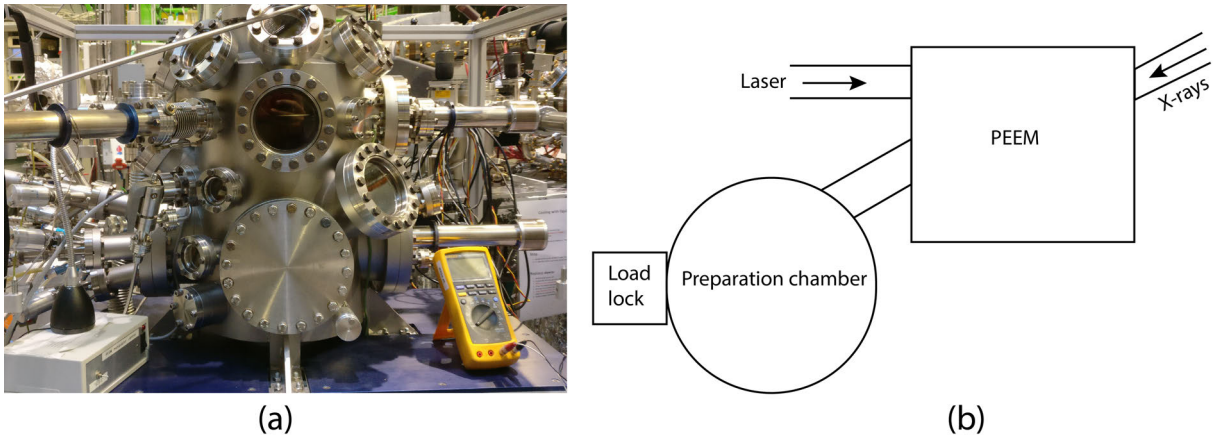

Figure 3.2: (a) Picture showing preparation chamber and (b) a schematic of the overall PEEM instrument at the SPEEM station at BESSY-II.

3.2 Contrast mechanisms

A sample might contain topographic defects or scratches with sharp boundaries that may affect the electron trajectories by local electrostatic micro-fields. The topographic contrast originates from the local distortions of the accelerating field at the edges of

geometrical structures on the sample. Parameters such as shape and size of the defect, the acceleration field and position of the contrast aperture determine the contrast by the topographic structures on the sample (Figure 3.3).

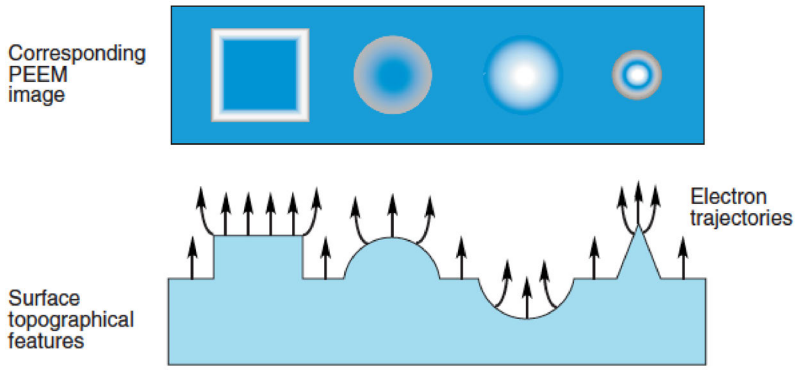

Figure 3.3: Contrast in XPEEM created by topographic structures on the sample that induce electrostatic field distortions. The figure is adapted from [72].

The work function of the sample is correlated with its chemical and structural environment. In a heterogeneous sample comprising of different elements, the local contrast of the image directly depends on whether the incident photon energy is higher/lower than the work function of the corresponding element. Such contrast only provides qualitative information about the chemical composition of the sample.
With the help of tunable synchrotron radiation, the photon energy can be tuned to the absorption edges of different elements in consideration. In a chemically heterogeneous sample, if a particular element is present/absent in a sample region, the absorption from the particular region is higher/lower. A spatial distribution of the involved elements can be generated by examining the sample with different photon energies.
The magnetic contrast in XPEEM is obtained by means of XMCD, i.e. by using circularly polarized X-rays. As discussed in section 2.3, for a fixed magnetization, the absorption by a circularly polarized photon is helicity dependent. Magnetic domain imaging is carried out by recording the 'PEEM' images at an absorption edge with sizable XMCD with opposite circular helicity of X-rays ($c+$ and $c-$). The magnetization is proportional to the XMCD relation given by equation 2.5. In PEEM, instead of plotting the XMCD (equation 2.5), it is more common to plot its asymmetry in XMCD (A_{XMCD}) to correct for the inhomogeneity in the sample illumination. It is given by,

$$A_{XMCD} = \frac{I(c-) - I(c+)}{I(c-) + I(c+)} \tag{3.1}$$

A PEEM image recorded with circularly polarized X-rays from a magnetic sample comprises of the contrast from both magnetic (M) and non-magnetic (M) sources.

$$I(c-) = I(c-, M) + I(c-, NM) \qquad \text{for } c- \tag{3.2}$$

$$I(c+) = I(c+, M) + I(c+, NM) \qquad \text{for } c+ \tag{3.3}$$

Unlike the non-magnetic contrast, the magnetic contrast reverses with polarization.

$$I(c-, M) = -I(c+, M) \qquad \text{and} \qquad I(c-, NM) = I(c+, NM) \tag{3.4}$$

Therefore, the magnetic contrast is proportional to the difference of the images recorded with $c+$ and $c-$ while the non-magnetic contrast is proportional to the average.

$$I(M) = \frac{I(c-) - I(c+)}{2} \qquad I(NM) = \frac{I(c-) + I(c+)}{2} \tag{3.5}$$

Thus, the asymmetry in the XMCD can be rewritten as,

$$A_{XMCD} = \frac{I(M)}{I(NM)} \tag{3.6}$$

The maximum XMCD contrast is observed when the X-ray beam is either parallel or anti-parallel to the magnetization direction. The magnitude of the XMCD signal is proportional to the projection of magnetization $\boldsymbol{M}$ along $\boldsymbol{k}$, i.e. XMCD $\propto |\boldsymbol{M}|$ cos($\boldsymbol{kM}$). The X-rays are incident to the sample at a grazing angle of 16°, resulting in a strong sensitivity to in-plane magnetization proportional to cos(16°). The out-of-plane magnetization has a three times smaller contrast (proportional to sin(16°)) as compared to the in-plane magnetization along the beam direction. The domains with $\boldsymbol{M} \perp \boldsymbol{k}$ result in zero XMCD. In order to distinguish between the absence of ferromagnetism and $\boldsymbol{M} \perp \boldsymbol{k}$, an azimuthal rotation of the sample is generally performed. While the non-magnetic region show zero XMCD independent of the chosen azimuthal angle, the domains with $\boldsymbol{M} \perp \boldsymbol{k}$ change contrast according to the cosine dependence. Within this thesis, the strength of the XMCD is displayed using the color code shown in Figure 3.4. The blue/red color represents the component of the total magnetization projected along the beam direction in a parallel/anti-parallel manner. For example, Figure 3.5(a) and (b) show PEEM images recorded with $c+$ and $c-$ X-ray helicity, respectively at Fe L_3 edge. The corresponding XMCD image which displays the asymmetry given by equation 3.1 is shown in the Figure 3.5(c).

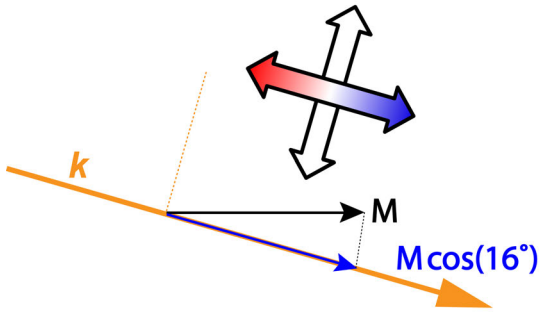

Figure 3.4: Schematic showing the projection of in-plane magnetization along the X-ray beam direction. The blue and the red color represents the parallel and the anti-parallel projection along the beam.

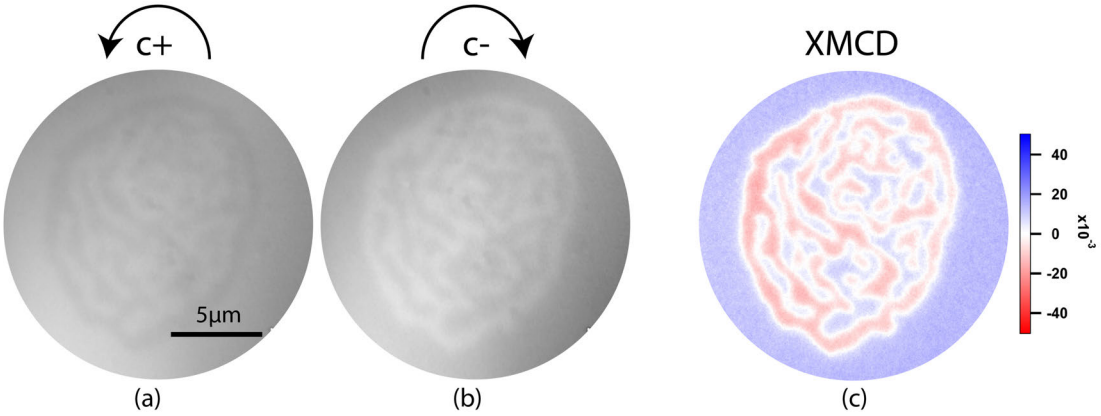

Figure 3.5: (a,b) Spatial photoemission intensity map or PEEM images recorded by circular polarization of X-rays $c+$ and $c-$, respectively. (c) XMCD image displaying the normalized difference of PEEM images shown in (a) and (b).

3.3 Laser set-up

A laser with a Femtolasers Scientific XL Ti:sapphire oscillator with a central wavelength of $\lambda = 800$ nm generating pulses at 5 MHz is attached to the PEEM instrument. The pulse duration of the pulses is around 60 fs. A pulse picker (Femtolasers Pulsfinder) adapts the repetition rate of the laser pulses from 2.5 MHz down to a single pulse. A neutral density filter in combination with a polarizer and a $\lambda/2$ plate is used to change the pulse intensity. A $\lambda/4$ plate provides circularly polarized laser pulses. The total fluence reached to the sample is assumed to undergo a loss of approximately 50% due to the reflections and absorption from the mirrors and lenses used in the measurement set-up.

For pump-probe measurements, the repetition rate of the laser pulses is altered in order to match the frequency of the electron storage ring of the synchrotron light source. The

measurements on TbFe films were carried out in the BESSY-II single-bunch mode of operation where the photon pulse derived from this bunch is repeated with 1.25 MHz frequency and a time interval of 800 ns between the consecutive pulses. The laser pulses are synchronized to the X-ray pulses by changing the repetition rate of the pulses to 1.25 MHz. The time delay line between the X-ray and the laser pulses can be continuously varied over 2 ns by a trombone and in further steps of 2 ns to cover the full range of the possible delays. The time resolution is limited to about 30 ps due to the duration of X-ray pulses.

3.4 Sample holder

Several customized sample holders developed by the SPEEM group provide a versatile sample environment such as in/out-of-plane magnetic field, out-of-plane electric field, and a femtosecond laser exposure [70, 73]. A wide temperature range of $42 - 600$ K is accessible with the help of an in-built liquid He cryostat and a heating element installed in the sample holders. For the measurements performed in this thesis, two different sample holders were used. The sample holder used for all-optical helicity dependent switching experiments provides an integrated laser optics that focus the laser on the back of the sample at normal incidence with a diffraction limited spot size [73]. The schematic and the picture of the sample holder is shown in Figure 3.6(a) and (b), respectively. The laser enters the sample holder and undergoes a reflection by a mirror where it is focused on the sample after passing through a focussing lens. Figure 3.6(c) shows a PEEM image recorded during laser illumination on a reference sample. The photon energy of the laser is around 1.55 eV at 800 nm wavelength which is not enough to excite the photoelectrons from the sample by single photon photoemission. It is assumed that these photoelectrons originate from nonlinear processes, such as three-photon photoemission process or collective excitation by surface plasmon. This photoemission intensity is used to locate the laser position on the sample. A line profile across the laser spot in Figure 3.6(d) shows that the laser spot has a Gaussian shape and about $3 - 5\mu$m spot size (FWHM in long and short axis). The laser position with respect to the sample is fixed, but a small tilt correction in the alignment of the sample with the instrument allows to laterally displace the laser spot by a few microns. More information about the sample holder can be found in [73].

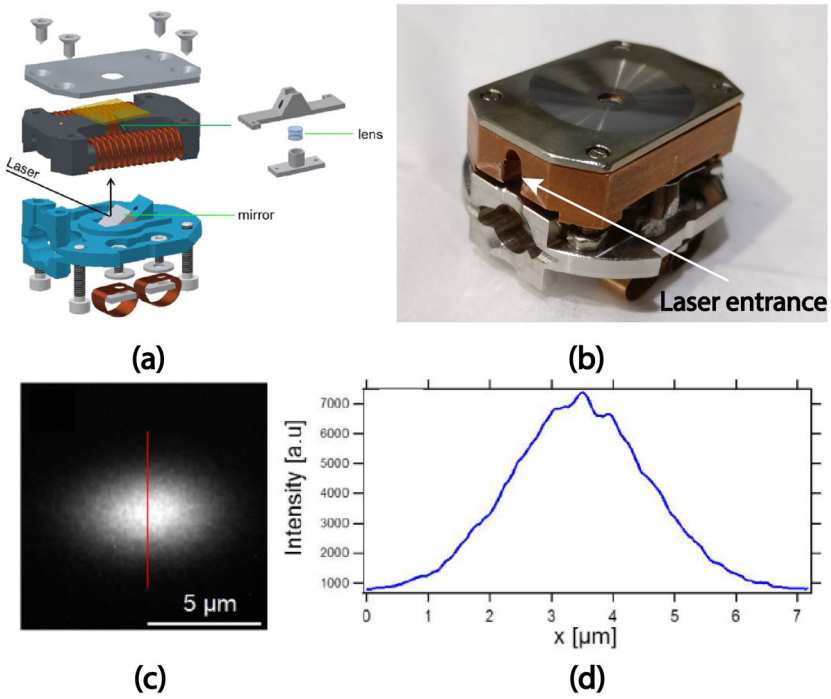

Figure 3.6: Schematic (a) and (b) a picture of the sample holder where a mirror and a lens focus the laser light from the back side on the sample. (c) Direct photoemission from the laser spot measured by PEEM. (d) Profile across line on the laser spot in (c). The figure is adapted from [73].

The second sample holder is optimized for ferroelectric samples and is capable of simultaneously providing an out-of-plane electric field, an in-plane magnetic field, heating (with a tungsten wire), and temperature control (by reading the temperature via Pt-100 resistive sensor) [74]. Figure 3.7(a),(b) shows a picture and a schematic of the side-view of the sample holder. A spring beneath the sample avoids the sample damage by compensating for the mechanical stress generated in the ferroelastic substrate post application of an electric voltage.

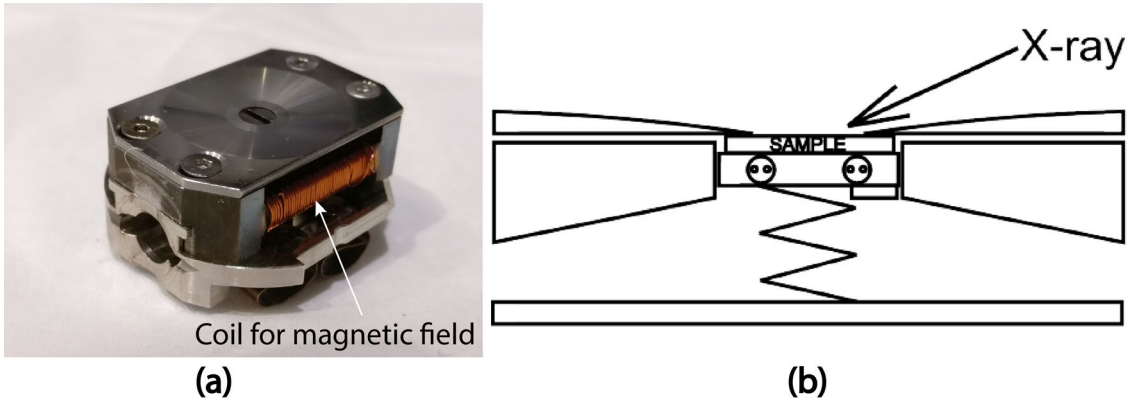

Figure 3.7: (a) Picture and (b) schematic showing the sample holder used to mount the ferroelastic substrates. The figure is adapted from [74].

3.5 Data acquisition

Spectroscopy is performed in XPEEM by recording a series of PEEM images at different photon energies in small steps of 0.2 eV across the absorption edge of the element under consideration. All the acquired images are stacked together and are normalized with a reference image that shows the state of the screen and is recorded beforehand in the de-focused condition of the microscope. This normalization procedure removes the variations in detection efficiency and the blind spots/defects of the screen from the PEEM images. A reference defect on the sample (whose contrast is independent of X-ray helicity) is used to correct the lateral drift within the individual images caused by the instrument/sample environment during the measurement. From this stack of normalized and drift corrected images, the local contrast is extracted from a selected region of interest (see Figure 3.8). The magnitude of the contrast intensity is plotted with the corresponding photon energy used to record the image. The local variations in the chemical and structural environment can be studied by analyzing the shape, size, and peak positions of the resonant absorption peaks.

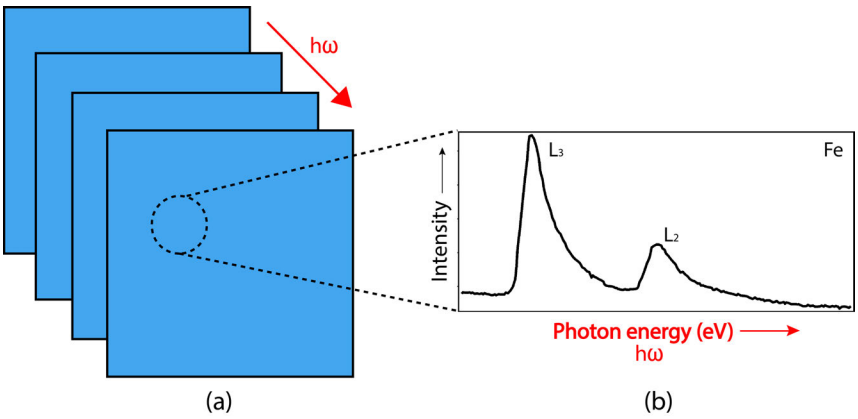

Figure 3.8: Schematic showing (a) PEEM images stacked together and the dotted region of interest. (b) The XAS spectra extracted from a local region of interest marked by dotted circle in (a).

Element selective XMCD is used to carry out the space-resolved magnetic imaging in XPEEM. The photon energy is tuned to the absorption resonance of the element of interest and the PEEM images are recorded with the opposite circular polarization ($c+$ and $c-$) of the X-rays. Typically, 30 images with $c+$, followed by 30 images with $c-$ are recorded, each with 3 second exposure time. After the normalization and drift correction of the stack, the images with $c+$ and $c-$ are separated and averaged individually. The XMCD image (Figure 3.5(c)) is obtained by calculating the asymmetry between the two X-ray polarization normalized by their sum (equation 3.1). All the data analysis is performed via Igor Pro (version 6.34).

Chapter 4

Spatially resolved AO-HDS in TbFe alloys

In this chapter, the phenomenon of the all-optical helicity dependent switching (AO-HDS) is investigated using a stationary femtosecond laser spot in TbFe alloys. Section 4.1 gives an introduction to the research field of optical control of magnetization via a femtosecond laser, with a focus on AO-HDS. Section 4.2 characterizes the magnetic properties of TbFe samples grown with variable alloy composition and film thickness. Section 4.3 describes the laser-induced switching in two different modes of measurement: single pulse and pulse train. Section 4.4 reports on the observation of AO-HDS in the pulse train mode and the impact of laser heating on the switching process. The relaxation effects influencing AO-HDS after removing the laser from the sample are discussed in section 4.5. Section 4.6 provides the magnetic field equivalent strength of AO-HDS followed by thickness dependent measurements in section 4.7. The dynamic nature of laser-induced magnetization switching is described in section 4.8. The presented results are discussed in section 4.9.

4.1 Optical control of magnetization: an overview

The interaction between light and magnetism has been studied for several decades, but the interest in the field of femtosecond magnetism was triggered by a pioneering experiment by Beaurepaire *et al.* showing sub-picosecond ultra-fast demagnetization with a 60 fs laser pulse in Ni [75]. A phenomenological 'three-temperature model' was introduced which suggested that the laser-induced change in temperature can be distributed across three different reservoirs: the electron system, the spin system and the

lattice system [75]. The motivation of the scientific community to pursue this magneto-optical interaction was to induce magnetization switching optically. Even though the observed demagnetization was not a magnetization switching (180° reversal), it was shown that an external magnetic field during demagnetization could induce a complete magnetization reversal [76–78]. However, it was accompanied by a major disadvantage of time-varying magnetic fields to access both magnetic states.

Two different mechanisms have been proposed to explain this ultra-fast magneto-optical interaction. The first one is based on thermal or heat-driven effects, which account for the absorption of a photon by the magnetic material and subsequent heat distribution amongst electrons, spins, and phonons, for instance, an ultrafast demagnetization process by Beaurepaire *et al.* [75, 79, 80]. The second mechanism is based on non-thermal effects, described by an 'optomagnetic' mechanism based on the transfer of angular momentum from light to magnetic material via the Inverse Faraday Effect (IFE), microscopically functioning as a spin-flip stimulated Raman-like process [81–83]. The faraday effect is a magneto-optical phenomenon originating from the interaction of light and magnetic materials with non-absorbing properties. Linearly polarized light can be decomposed in equal left and right circularly polarized components: $\sigma+$ and $\sigma-$. The $\sigma+$ and $\sigma-$ experience different refractive indices and thus propagate at a slightly different speed in magnetic media. This causes a change in the phase difference between $\sigma+$ and $\sigma-$ with respect to the incoming light that leads to a rotation (known as the Faraday rotation) of the polarization plane of the light. IFE induces an effective static magnetization $M(0)$ when a circularly polarized light with an oscillating electric field and its complex conjugate (E and E^*) with frequency ω transmits through a magnetic medium [84–86]. The induced magnetization is given by,

$$M(0) = \frac{\chi}{16\pi}[E(\omega) \times E^*(\omega)] \tag{4.1}$$

where χ is the magneto-optical susceptibility. The cross-product in equation 4.1 shows that the magnetization $M(0)$ is induced along $\mathbf{k}$ (the wave vector of the light). The $\sigma+$ and $\sigma-$ laser helicity at a frequency ω induces an equal and anti-parallel static magnetization. Therefore, like an externally applied magnetic field, circularly polarized light can also generate a magnetization in a magnetic material. Kimel *et al.* demonstrated that ultrashort circularly polarized femtosecond laser pulses could optically and non-thermally excite and control the spin oscillations in a weak ferromagnet $DyFeO_3$ [81] by IFE as shown in Figure 4.1. A sudden change in the Faraday rotation is followed by spin oscillations which were assigned to magnetization precession due to induced magnetic field by $\sigma+$ or $\sigma-$.

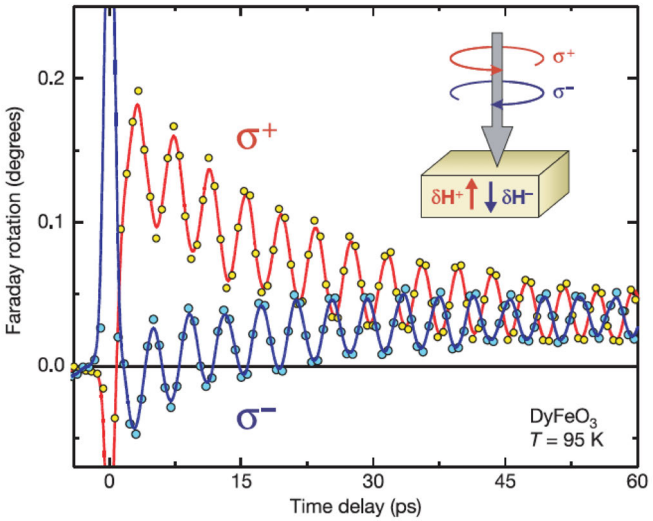

Figure 4.1: Figure showing temporal evolution of the Faraday rotation in $DyFeO_3$ for two circularly polarized pump pulses of opposite helicities $\sigma+$ and $\sigma-$. The figure is adapted from [81].

In another experiment, a non-thermal interaction between circularly polarized laser and ferrimagnetic GdFeCo was studied by Stanciu *et al.* in 2007 [83]. Here, the IFE was understood to be an ultrafast non-thermal interaction between photon angular momentum with the magnetic system that does not require absorption of light, based on Raman-like coherent optical scattering process [82,87]. The IFE was also questioned by some groups which argued that the photon angular momentum is not enough to be able to induce changes in the magnetization [88].

It was anticipated that the circularly polarized laser light could behave as an external magnetic field parallel to the direction of light via IFE [81,89]. The $\sigma+$ and $\sigma-$ pulses would then act as a magnetic field of anti-parallel orientations. The breakthrough occurred with the discovery of all-optical helicity dependent (AO-HDS) switching when circularly polarized femtosecond laser pulses were used to deterministically switch the magnetic state of ferrimagnetic Gd_{22} $Fe_{74.6}$ $Co_{3.4}$ [6]. The switching was only observed in a narrow window of laser fluence. The experiments were performed on an amorphous ferrimagnetic alloy of GdFeCo with thickness 20 nm (having perpendicular magnetic anisotropy) which is used in magnetic recording and possesses strong magneto-optical properties. A Ti:sapphire laser with a wavelength of 800 nm, FWHM = 40 fs and repetition rate of 1 kHz was swept across the alloy and imaged under a Faraday microscope. Figure 4.2(a) shows the initial magnetic domains before laser exposure on the sample. The dark (M^+) and bright areas (M^-) are the two out-of-plane magnetic orientations with magnetization 'up' and 'down', respectively. The laser beam was swept from left

to right with different laser polarization. Figure 4.2(b) shows the effect of laser sweep on magnetic domains with three different polarizations, positive circularly polarized ($\sigma+$), linear polarized (L) and negative circularly polarized ($\sigma-$) laser light.

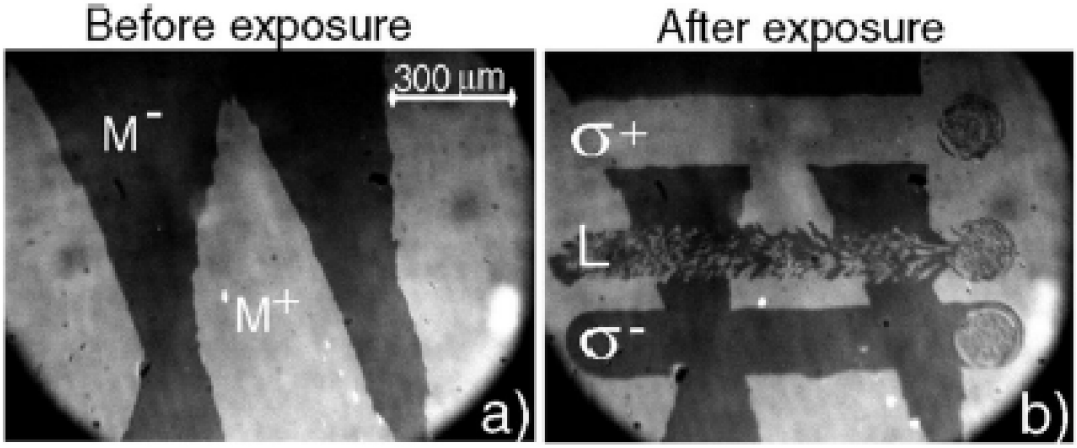

Figure 4.2: (a) Initial magnetic state of the sample before laser exposure with M^+ (bright) and M^- (dark) regions as 'up' and 'down' magnetization orientation. (b) Domain pattern obtained after sweeping the laser beam with positive circularly polarized laser ($\sigma+$), linear polarized laser (L) and negative circularly polarized laser ($\sigma-$), with fluence of about 11.4 mJ/cm^2. The figure is adapted from [6].

As shown in Figure 4.2, the $\sigma-$ and $\sigma+$ helicity resets the magnetic state of the sample to M^- and M^+, respectively. On the other hand, the linear polarization L leads to a random multi-domain magnetic pattern due to demagnetization above T_c and subsequent cooling in the absence of any magnetic field without favoring any particular magnetic orientation. The explanation for this preferential helicity dependent switching behavior was suggested to be a combination of two effects: the absorption of laser energy into the magnetic system increasing the temperature close to Curie temperature (T_c) and circularly polarized light simultaneously behaving as a magnetic field for switching the magnetization. The presence of AO-HDS was also observed in other RE-TM ferrimagnets like TbFe and TbCo [90].
While heat-driven effects were considered unfavorable in some cases, other theoretical and experimental investigations showed that AO-HDS in GdFeCo alloy films is a two-fold process, which consists of quenched magnetization by ultrafast laser-induced heating within 1 ps followed by a helicity-dependent relaxation to an equilibrium state (few tens of ps) arising from IFE [91]. However, shortly after the discovery of AO-HDS in GdFeCo, it was demonstrated that switching via single heat pulses alone could act as a sufficient stimulus to switch the magnetic state reversibly in GdFeCo, independent of laser helicity [92]. The nature of such a switching process was demonstrated

by Radu *et al.* who discovered the formation of a transient ferromagnetic-like state in the ultrafast spin reversal mechanism of antiferromagnetically coupled GdFeCo alloy [93]. The switching mechanism in GdFeCo is a special case and is different from switching in other RE-TM alloys such as TbFe and TbCo. The difference arises from the independent demagnetization dynamics of Gd and Fe sublattices on significantly different time scales (1.5 ps for Gd sublattice and 0.3 ps for Fe sublattice) that put the initial ferrimagnetic system into a transient ferromagnetic state. Gd has a half-filled $4f$ orbital and thus zero orbital angular momentum. The spin-orbit coupling is weak in Gd-based alloys which has a significant effect on the demagnetization dynamics via laser pulse. Figure 4.3 shows the switching between 'up' and 'down' magnetization via a sequence of five consecutive single laser pulses of linear polarization for GdFeCo alloy. Beginning from an initial anti-parallel uniform magnetization in Figure 4.3(a) and 4.3(b), the area of the sample interacting with the laser is switched in the opposite direction with each incoming laser pulse.

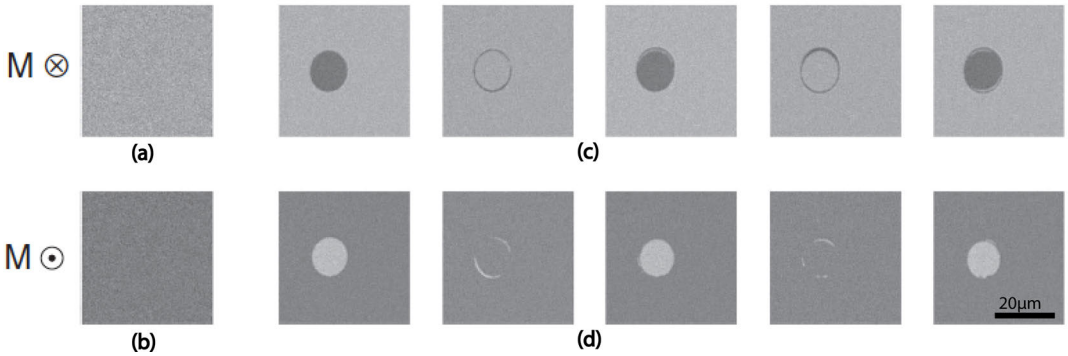

Figure 4.3: (a,b) Initial uniformly magnetized state of $Gd_{24}Fe_{66.5}Co_{9.5}$ film with magnetisation 'up' and 'down' respectively. (c,d) The film after an excitation with N (N = 1, 2..5) laser pulses with linear polarisation and laser fluence of 2.3 mJ/cm^2. The figure is adapted from [92].

In a temperature dependent study of magnetization reversal by laser pulses, Hohlfeld *et. al.* argued that all-optical switching is an athermal process with higher efficiency at low temperatures [94]. The importance of heat driven effects could not be undermined since the switching was observed in multiple shot laser exposure which accumulates heat on the sample [95]. A practical implication of such thermally assisted magnetization switching process was also proposed in HAMR (Heat-assisted magnetic recording) technology in magnetic recording devices [96]. To investigate the importance of heating in the switching process, Alebrand *et al.* performed repetition-rate dependent experiments where they measured the minimum fluence F_{min} required to switch the sample as a function of the repetition rate of the laser [80]. The result is shown in Figure

4.4(a) where F_{min} decreases with the repetition rate of the laser. This observation indicates that the higher repetition rate leads to significant heat accumulation on the sample, thus requiring lower laser fluence to switch the sample. To disentangle the interplay of heating and helicity effects, they carried out a pump-probe experiment called $\sigma - \pi$ heating in $Gd_{24}Fe_{66.5}Co_{9.5}$. Here, the incoming laser excitation was divided into a linearly polarized π pulse inducing only sample heating and a circularly polarized σ pulse introducing the helicity information with a certain time delay between them. Figure 4.4(b) shows that switching was observed for both negative and positive time delays and the width of the delay window (yellow region in Figure 4.4(b)) depends on the fluence of the π-pulse. They showed that the threshold fluence for switching is not only determined by the number of circularly polarized photons but a minimum amount of heating is also necessary for the switching process [80]. They concluded that the switching process could not take place entirely from non-thermal origins.

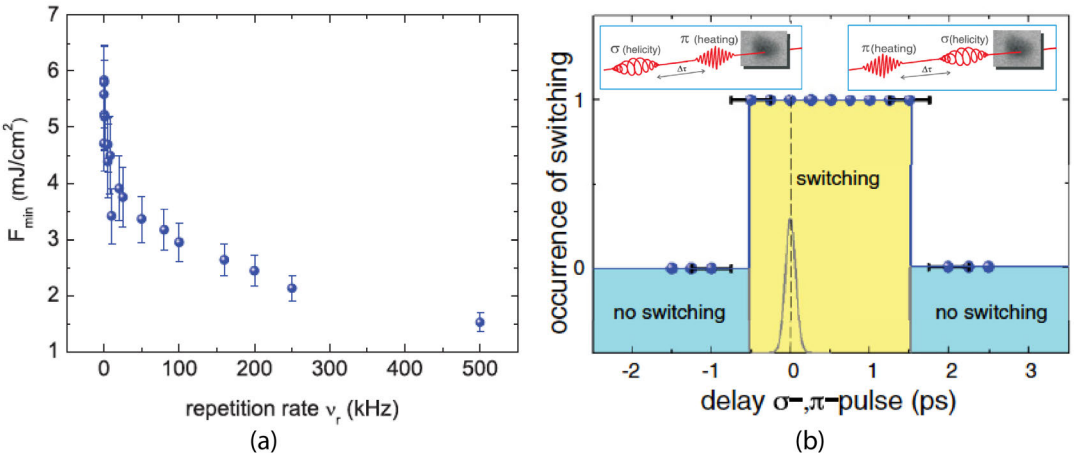

Figure 4.4: (a) Plot showing the decreasing trend of minimum threshold fluence with increasing repetition rate. (b) $\sigma - \pi$ switching experiment showing switching for positive (σ arrives before π pulse) and negative (π arrives before σ pulse) delays. The figure is adapted from [90].

Another approach to study the temperature-dependent efficiency of AO-HDS was carried out by Hassdenteufel *et al.* where the temperature of the sample was increased using an external resistor [97]. They stressed on the importance of laser-induced heating and low-remanent magnetization of the material for observing AO-HDS. The necessity of heat accumulation was also depicted in another study where the authors used a heat diffusion model on large time scales of microseconds to quantify the deposited heat in multi-shot experiments in different substrates of silicon and glass [98].
A thermally driven fundamental mechanism of magnetic circular dichroism (MCD) was proposed by Khorsand *et al.* to explain the microscopic physics behind the AO-HDS

[99]. The MCD effect refers to the differential absorption of the laser energy depending on the polarization of the laser and magnetic orientation of the sample. This leads to a preferential heating of one magnetic orientation with a particular helicity. Khorsand *et al.* provided quantitative explanations for the presence of an intensity window for AO-HDS due to MCD in GdFeCo alloy. It was estimated that a dichroic effect of about $0.5 - 2\%$ is enough to induce AO-HDS. Figure 4.5(a) shows the switching probability of the sample as a function of laser fluence for three different polarizations for a fixed laser wavelength. As shown, the sample can be switched with all three polarization but with different laser fluence with $F_{\sigma-} < F_L < F_{\sigma+}$. Materials like GdFeCo have strong magneto-optical properties and therefore experience different absorption for left and right circular polarization ($\sigma+$ and $\sigma-$) with a particular magnetization orientation. Thus, the difference between the threshold switching fluence $F_{\sigma-}$ and $F_{\sigma+}$ as shown in Figure 4.5 is proportional to the difference between the absorption of $\sigma+$ and $\sigma-$ helicity. The MCD effect is calculated in terms of the absorption of laser $A_{\sigma+}$ and $A_{\sigma-}$ by $\sigma+$ and $\sigma-$, respectively and is given by,

$$MCD = \frac{A_{\sigma+} - A_{\sigma-}}{\frac{1}{2}(A_{\sigma+} + A_{\sigma-})} \tag{4.2}$$

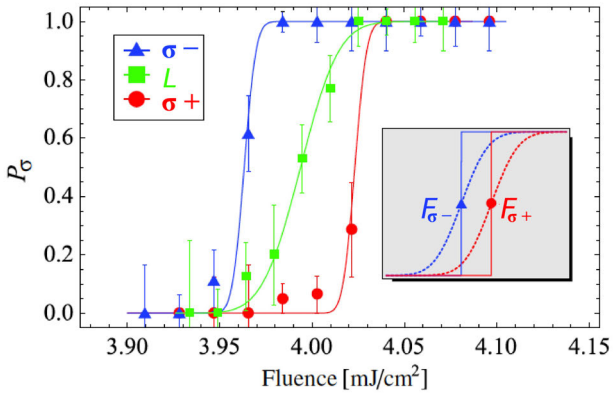

Figure 4.5: (a) Switching probability P_σ as a function of laser fluence at $\lambda = 700$ nm for three different laser polarisations $\sigma+, \sigma-$and L. The inset shows the threshold laser fluence $F_{\sigma+}$ and $F_{\sigma-}$ for switching via $\sigma+$ and $\sigma+$, respectively. The figure is adapted from [99].

Another major advancement occurred when it was shown that AO-HDS is rather a general phenomenon which is not limited to selected RE-TM alloys but also observed in a much wider variety of materials including heterostructures, multilayers and even ferromagnets [15, 16]. This observation suggested a common origin for AO-HDS in all such different materials. These results questioned the previous conclusions obtained

for ferrimagnets based on a relevant role of magnetization compensation temperature T_M on AO-HDS as ferromagnetic systems such as Co/Pt and Co/Ni do not show any T_M at all [16]. Therefore, the fundamental mechanism behind the switching process was still unclear.

The phenomenon of AO-HDS is considered the most promising candidate for magneto-optics and spintronics, offering a promising insight into a deterministic optical control of magnetic state without applying any external magnetic field. However, even after two decades of intensive research, there are numerous open questions in this field that need to be addressed. Most experiments in the literature have been performed via a laser spot size of tens to hundreds of microns. However, from an application point of view, it is essential to study the scalability of the switching process down to small laser spot sizes. When the laser spot size is reduced, significant dipolar field effects are reported to play a dominant role influencing the magnetization switching process [100]. The lack of high spatial resolution imaging techniques in most of the previous studies did not draw attention to dipole-dipole interactions which play a significant role in switching via small laser spot sizes. The role of heat accumulation and temperature dependence of the switching process has been explored by various publications in the literature but an unambiguous picture to explain its importance is still missing. With the numerous explanations for the microscopic mechanism of AO-HDS, the scientific debate has not been conclusive. To address these critical issues, this thesis aims to investigate the scalability of the AO-HDS process to small laser spot sizes, the role of laser heating and temperature in magnetization reversal, influence of dipolar field effects, and the microscopic origin of AO-HDS via in-situ experiments by means of photoemission electron microscope (PEEM). The switching mechanism is studied by imaging the magnetic state of the sample during the laser interaction. This way the relaxation effects after removal of the laser exposure are minimum. With the high spatial resolution, element selectivity and the extraordinary capability to image the modification in the magnetization caused by the laser pulses while the laser interacts with the sample, a comprehensive investigation of AO-HDS without any interference from relaxation effects is performed.

4.2 Sample characterization

A series of amorphous Tb_xFe_{1-x} (TbFe) films were fabricated by magnetron sputtering on MgO substrates (0.5 mm thick) at room temperature. The MgO [100] substrates were double-side polished and transparent to the laser wavelength (800 nm) used for AO-HDS experiments. The samples were prepared by the group of Florin Radu in

a magnetron sputtering chamber MAGGSY at Helmholtz Zentrum Berlin. The TbFe films were grown with a Ta (5 nm) buffer layer and capped with 1.8 nm of Pt to prevent oxidation. The fabricated samples included two alloy compositions: 22% (10, 20, 40, 60, and 80 nm) and 30% (10, 15, and 20 nm) with different thickness. In this thesis, the samples are referred to as TbXY where X specifies the Tb concentration in % (either 22 or 30), and Y specifies the thickness of TbFe magnetic alloy in nanometers.

As described in section 1.6, below(above) compensation temperature T_M, the total magnetization of the alloy orients along the Tb(Fe) sublattice and hence the alloy posses a 'Tb(Fe) dominant' sublattice. The T_M of ferrimagnetic thin films such as TbFe can be altered by varying the alloy composition as well as the film thickness [35, 101, 102]. Above a threshold 'effective' Tb concentration (depending on the film thickness), the ferrimagnetic alloy loses its magnetization at T_c before it reaches T_M. In such cases, T_M does not exist and the alloy posseses a Tb dominant sublattice for $T < T_c$ [35].

The magnetic properties and T_M of TbFe samples were characterized by Superconducting Quantum Interference Device (SQUID) magnetometry. The hysteresis loops were measured at different temperatures up to 390 K using a SQUID-VSM with magnetic field applied perpendicular to the sample's surface. The hysteresis loops for Tb2210, Tb2220, Tb3010 and Tb3020 are plotted in Figure 4.6(a), (b), (c), and (d), respectively. All samples exhibited a strong perpendicular magnetic anisotropy as evident by the square shape of the hysteresis loops. The T_c for the TbFe thin films between 20-30% Tb concentration is reported to be around $380 - 400$ K [35, 101, 103]. From coercivity and remanence values in Figure 4.6(a), T_M for Tb2210 is found to be approximately around 250 K where it transforms from Tb dominant sublattice below 250 K to Fe dominant sublattice above it. Increasing the film thickness to 20 nm and above results in Tb dominance over the entire range of temperature until it reaches T_c at 380 K (no T_M). For 30% concentration, the hysteresis loops for samples Tb3010 and Tb3020 are plotted in Figure 4.6(c) and (d), respectively. Both samples posses Tb dominant sublattice with no T_M.

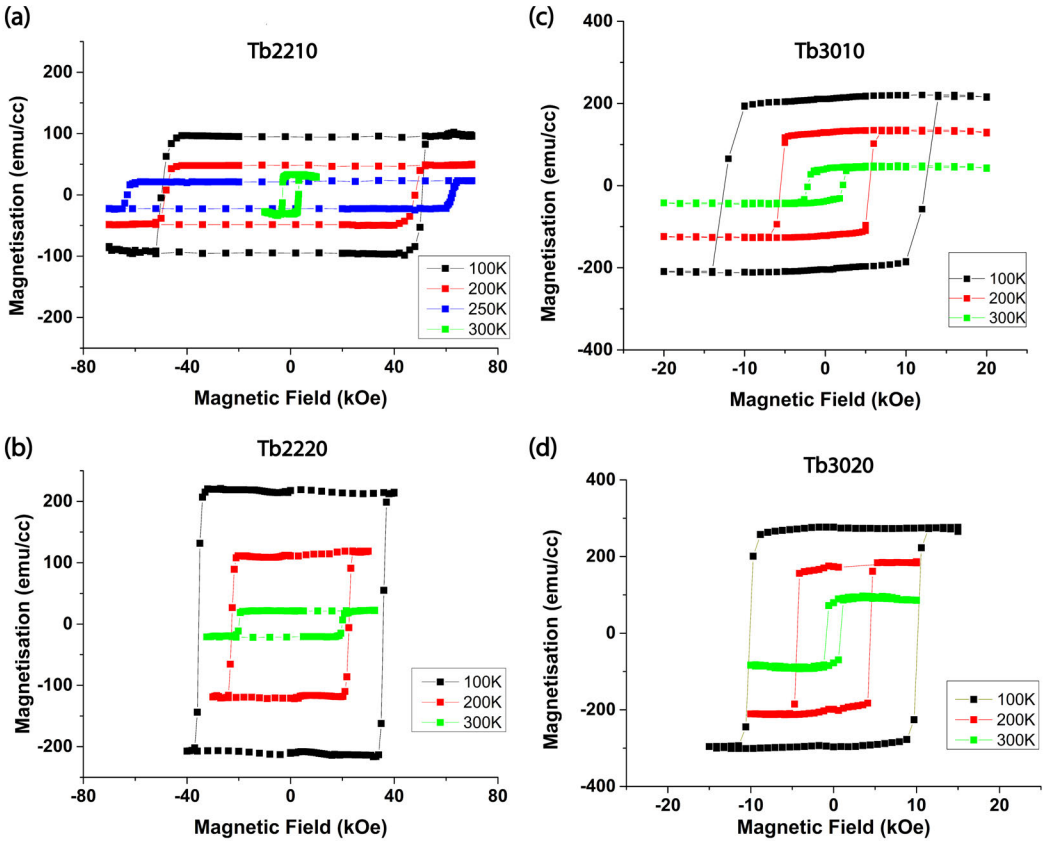

Figure 4.6: Hysteresis loops in an out-of-plane configuration measured for (a) Tb2210 (b) Tb2220 (c) Tb3010, and (d) Tb3020 samples.

Prior to PEEM experiments, all the samples were ex-situ out-of-plane magnetized with a permanent magnet in order to have a homogeneous magnetic domain state before mounting on the sample holder. Before laser exposure, the chemical and magnetic characterization was performed via PEEM. Figure 4.7(a) shows Fe XAS spectra with L_3 and L_2 absorption edges of the Tb2210 sample. Similarly, the Tb M_5 and M_4 absorption edges and XAS spectra are shown in Figure 4.7(b). The XAS spectra show the expected spectral features for both Fe $L_{3,2}$ and Tb $M_{5,4}$ edges confirming a good sample quality. No sign of oxidation is observed in XAS spectra implying that the protective capping layer on the sample is sufficient. The photon energy was set to the resonant peak of the Fe L_3 edge (707.3 eV) and the magnetic contrast of the Fe sublattice was probed by recording a XMCD image as shown in Figure 4.7(c). The Tb sublattice was probed by recording the XMCD image at the photon energy corresponding to the M_5 absorption edge (1236.5 eV) as shown in Figure 4.7(d). XMCD images obtained at 707.3 eV and 1236.5 eV in Figure 4.7(c) and (d) show magnetic contrast of opposite sign (blue and red) as expected from the antiferromagnetic coupling between the Fe and Tb sublattices.

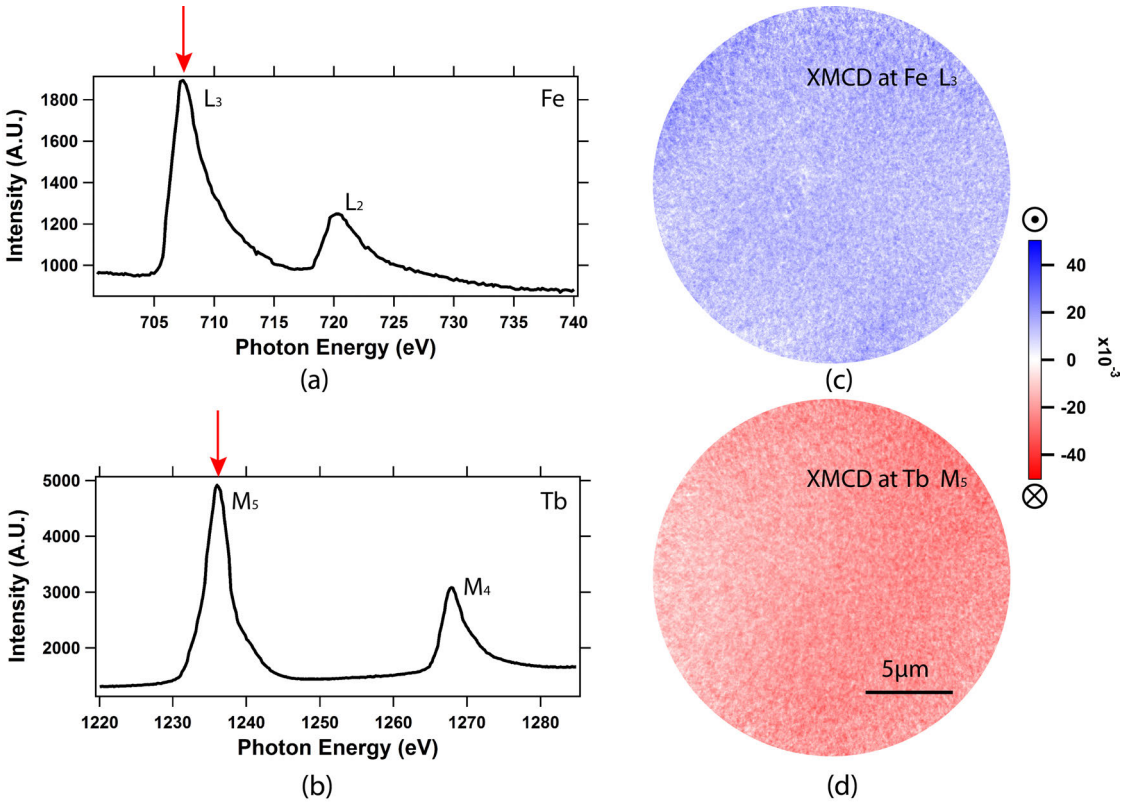

Figure 4.7: (a, b) XAS spectra showing the Fe $L_{3,2}$ edge and Tb $M_{5,4}$ edge for Fe and Tb, respectively. (c, d) XMCD image recorded at Fe L_3 and Tb M_5 absorption edge. The opposite blue and red contrast signifies the antiferromagnetic coupling between Fe and Tb sublattice.

4.3 AO-HDS in different modes of measurement

The femtosecond laser can be operated in two different modes: Single pulse and Pulse train mode. In the latter, the laser pulses illuminate the sample with a specific repetition rate which can be set by the pulse picker. The effect of single pulses and pulse trains on the magnetization of TbFe alloy is discussed in this section.

Single pulse mode

There are different scenarios in which a single pulse can affect a uniformly magnetized saturated sample. Below a threshold laser fluence (Case I), the laser pulse heats the sample without any alteration in the magnetization as shown in the XMCD image in Figure 4.8(a).

As the fluence is increased above this threshold, the laser pulse switches the magnetization by forming a small bubble domain in the illuminated area (Case II). The formation

of such a bubble domain is dominated by the strong dipolar field of the surrounding region with saturated magnetization. The dynamics of the bubble domain was traced by Gierster *et al.* where the growth and decay of the bubble domain is resolved in a stroboscopic experiment [73]. In the absence of pinning centers such as defects, the bubble domain vanishes after the laser pulse and the magnetization is unaltered. Therefore, it is not possible to observe it in a static mode. However, it can be visualized in a pulse-train as shown in Figure 4.8(b) where the domain collapses when the laser exposure is stopped in Figure 4.8(c). The XMCD image in Figure 4.8(b) is obtained by averaging over the formation and collapse of the bubble domain for millions of single laser pulses, resulting in a faint red contrast in the bubble domain.

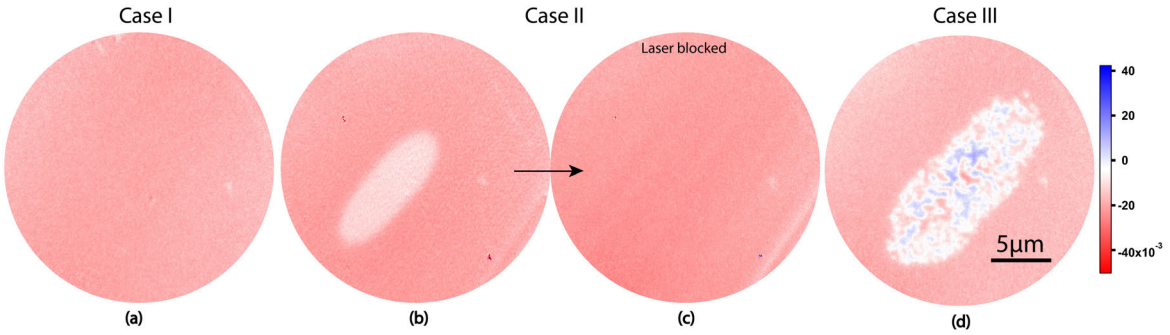

Figure 4.8: XMCD images recorded at Fe L_3-edge in Tb3020 alloy with $\sigma+$ helicity showing (a) homogeneous out-of-plane red magnetic contrast for laser fluence below the threshold, (b) bubble domain visualized by averaging over millions of laser pulses in a pulse train, (c) uniform magnetic contrast after the collapse of bubble domain (when the laser exposure is stopped), and (d) random multi-domain pattern after a single laser pulse of $\sigma-$ helicity with high laser fluence. The red and blue magnetic contrast represents anti-parallel out-of-plane magnetic orientations.

At high laser fluence above the threshold, a laser pulse causes local demagnetization of a larger area where the dipolar fields from the surrounding film are weaker (Case III) [104]. Consequently, the demagnetized area (larger than the correlation length scales) breaks into randomly oriented magnetic domains after quenching to the base temperature. Figure 4.8(d) shows XMCD images after illuminating the sample with single laser pulses with high laser fluence. As observed, the initial saturated magnetization of the sample disintegrates into a multi-domain pattern with 'up' and 'down' out-of-plane magnetization. Further increasing the laser fluence increases the demagnetized area formed after the single pulse (see Figure 4.9) [73].

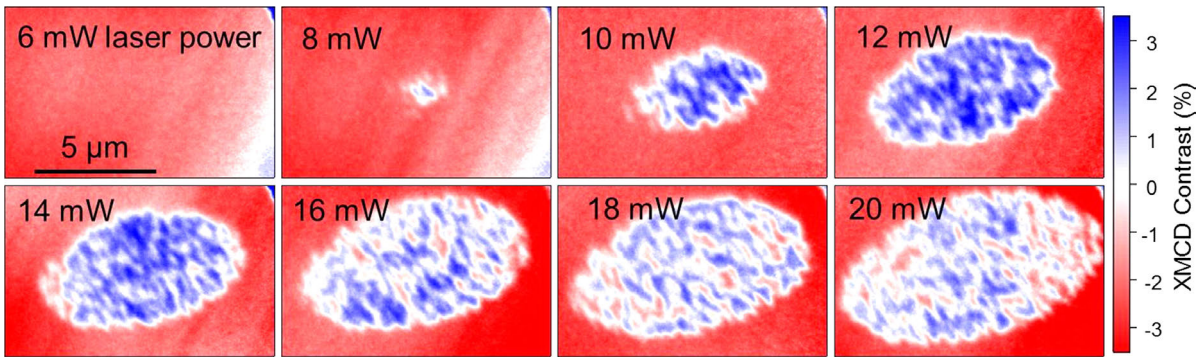

Figure 4.9: XMCD images showing the magnetic contrast of TbFeCo film at Tb M_5-edge after exposing the film to the single laser pulses. The same area of the sample is excited consecutively with higher laser powers. While no change in magnetic contrast is observed at 6 mW, the demagnetized area is formed above 8 mW which grows in size on increasing the laser power. The figure is adapted from Gierster *et al.* [73].

The sample area affected by a single laser pulse also depends on the base temperature of the sample. Figure 4.10(a-d) show XMCD images at different base temperatures 100 K, 140 K, 260 K, and 300 K after illumination with a single pulse of constant laser fluence. A domain marked in black defines the position of the illuminated area with respect to the sample's domain pattern. At a constant laser fluence, the area of the sample affected by laser illumination increases with the base temperature of the sample. In addition to the laser affected sample region, the individual domain size formed after demagnetization also increases with the base temperature. Such a difference in domain size arises because at higher base temperatures domains have higher thermal energy k_BT to overcome the magnetostatic energy. Their mobility and the ability to form bigger domains increases with base temperature. In addition, the threshold fluence required for magnetization switching decreases. This is because at higher base temperatures lower threshold fluence is required to reach T_c.

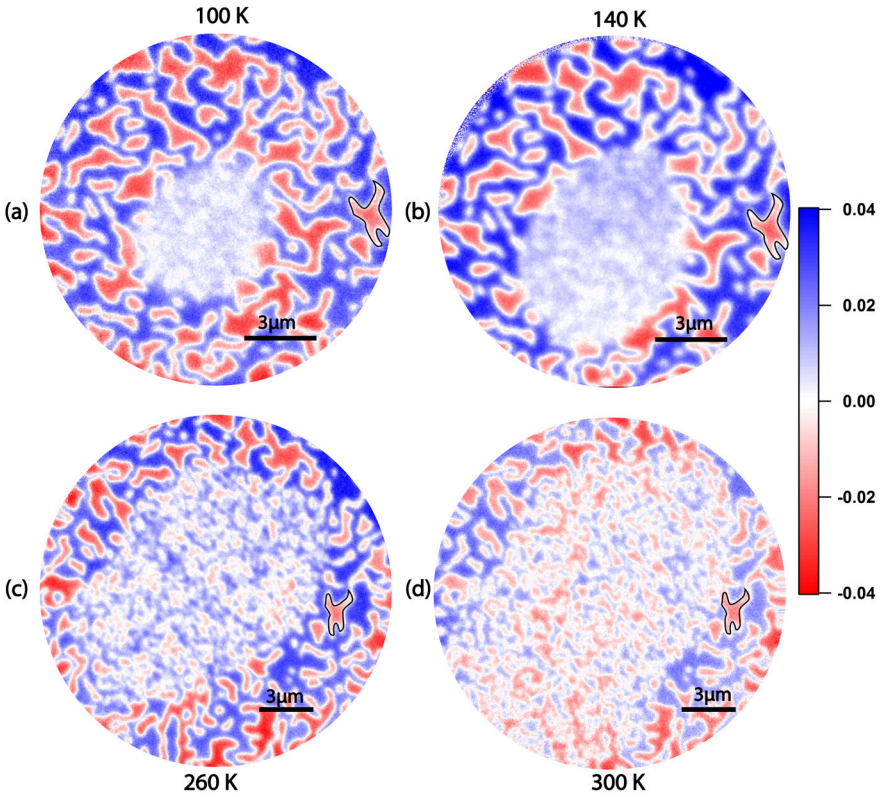

Figure 4.10: (a-d) XMCD images showing magnetic contrast of Tb2510 recorded at Fe L_3-edge showing random multi-domain structure after a single laser pulse, recorded at different base temperatures of 100 K, 140 K, 260 K and 300 K respectively. The field of view is 15 μm and 20 μm in (a,b) and (c,d), respectively. The domain marked in black is used as a reference for all the images.

Pulse train mode

To study the switching behavior with minimum interference from the relaxation effects after the laser exposure, the magnetization was imaged via XMCD in the pulse train mode while the laser interacts with the sample. In this case, the magnetic contrast probed via XMCD displays a temporal average over millions of laser pulses. Figure 4.11(a) shows XMCD image with $\sigma+$ laser helicity recorded in a pulse train mode with a repetition rate of 2.5 MHz. The interaction between the laser and the magnetic sample can result into three different regions marked by 1, 2 and 3 in Figure 4.11 [100]. The outermost region (marked by 3) is dominated by the dipolar fields of the surrounding region. The saturated red magnetic contrast of the surrounding region creates an inverse field that puts a blue contrast in the outer ring region of the illuminated spot. The inner-most region with white contrast marked by 1 is the 'thermally demagnetized' region where the laser has the highest intensity in a Gaussian shaped laser spot. Here, the sample gets, at least temporarily, demagnetized with each incoming single

pulse having a random magnetization in between consecutive pulses. Since the magnetic contrast in the XMCD image is a temporal average over millions of such laser pulses, an average over a full pulse train results in a zero (white) averaged XMCD. The thermally demagnetized region is surrounded by a 'ring-shaped' magnetic region (see Figure 4.11(a)) where the helicity dependent switching is observed. This ring-shaped region is not prominent in Figure 4.11(a) because the dipolar fields for this sample dominate at such small laser spot size. However, the ring-shaped region (marked by 2) is clearly visualized in Figure 4.11(b) which displays a difference between the two XMCD images obtained for opposite laser helicities $((\sigma+)-(\sigma-))$.

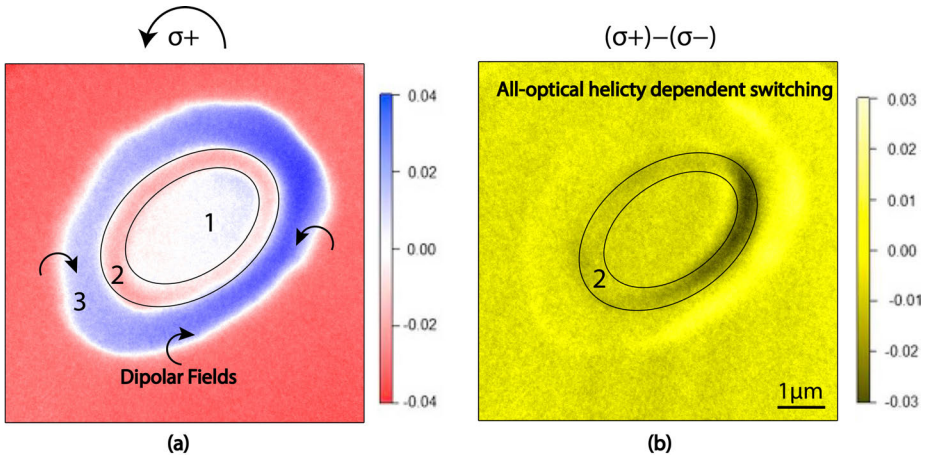

Figure 4.11: (a) XMCD image in a pulse train mode with $\sigma+$ helicity in TbFeCo alloy recorded at Fe L_3-edge depicting three different regions with: (1) Thermal demagnetization, (2) AO-HDS and (3) Dipolar field effects. (b) Difference between the XMCD images of opposite laser helicities $((\sigma+)-(\sigma-))$ displaying a ring-shaped region where AO-HDS (marked by 2) takes place. The figure is adapted from Gierster *et al.* [100]

The magnitude of the dipolar fields depends on the saturation magnetization of the film. This can be controlled by changing the intrinsic material parameters like film composition and film thickness or external conditions such as the base temperature. Many experiments performed in the literature use large laser spot sizes (tens of microns) to study AO-HDS [6, 15, 16, 105–107] where the effect of dipolar fields has not been significant. Dipolar fields are larger in micron-sized laser spots and could potentially interfere with helicity dependent switching [100]. Therefore, it is important to limit their influence on AO-HDS to study the switching behavior. In the experiments within this thesis, the contribution of dipolar fields is minimized by demagnetizing the illuminated spot by a high laser fluence single laser pulse so to have an initial random multi-domain state. This ensures a zero stray field from the surrounding saturated region which otherwise would influence the switching process.

4.4 AO-HDS occurs at the threshold of thermal demagnetization

The previous section identified three different characteristic regions established as a consequence of laser interaction with a TbFe thin film in the pulse train mode. In this section, the onset of AO-HDS and the essential conditions for an efficient helicity dependent switching in TbFe alloy are explored. As discussed in section 4.3, a single laser pulse above a threshold laser fluence facilitates thermal demagnetization and creates a random multi-domain pattern on the illuminated spot. Figure 4.12(a,b) shows a multi-domain pattern due to thermal demagnetization by single laser pulses of opposite laser helicity ($\sigma+$ and $\sigma-$) with a laser fluence of 6.25 mJ/cm^2.

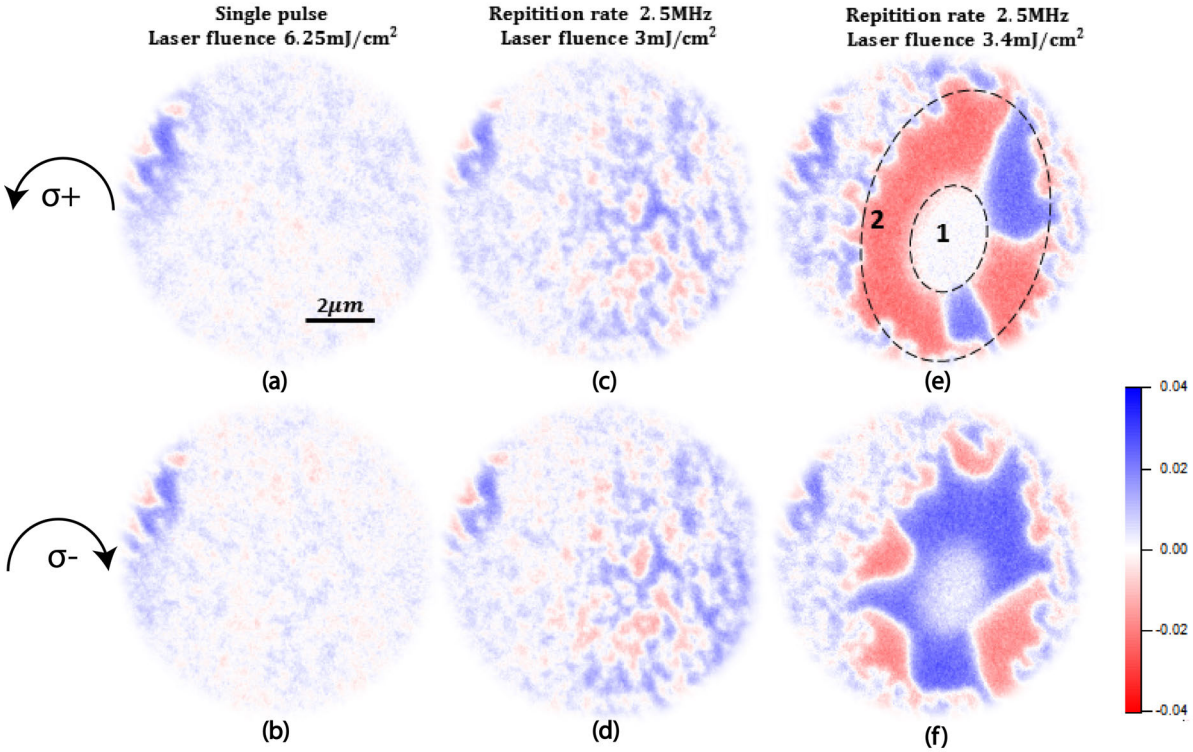

Figure 4.12: XMCD images showing magnetic contrast in Tb3010 for (a,b) single pulse measurements with $\sigma+$ and $\sigma-$, (c,d) laser pulse trains applied below the threshold power with $\sigma+$ and $\sigma-$, and (e,f) laser pulse trains above threshold with $\sigma+$ and $\sigma-$ showing thermal demagnetization (marked by 1) and AO-HDS in the ring region (marked by 2).

Starting from a multi-domain initial state, measurements at increasing laser fluence were performed with 2.5 MHz repetition rate to observe helicity dependent switching. The XMCD images recorded with opposite laser helicities are shown in Figure 4.12(c)

and (d). At a laser fluence of 3.0 mJ/cm^2, an increase in the magnetic domain size is observed because of local heat accumulation. However, no apparent helicity dependent switching is observed. By further increasing the laser fluence from 3.0 to 3.4 mJ/cm^2, the threshold of thermal demagnetization is surpassed at the center of the laser spot where a region with white magnetic contrast emerged (Figure 4.12(e) and (f)). The white region (marked by 1) in the center is correlated with the 'thermally demagnetized' region as also observed in Figure 4.11(a). The preferential contrast of red/blue in Figure 4.12(e)/(f) in a ring region (surrounding the thermally demagnetized region) on the basis of laser helicity $\sigma+$ and $\sigma-$ is attributed to AO-HDS. Thus, AO-HDS is observed to be a local effect within the illuminated laser spot that occurs in the vicinity of thermal demagnetization.

To investigate how the ring region adjacent to the thermally demagnetized region is switched by the laser, the laser helicity was flipped from $\sigma-$ to $\sigma+$ and the changes in the ring region were observed. The initial XMCD image was recorded with $\sigma-$ helicity (Figure 4.13(a)). Thereafter, the helicity was reversed to $\sigma+$ and XMCD images were recorded continuously without changing any other parameter. Figure 4.13(b) shows a transient domain state whereas Figure 4.13(c) is the final domain state recorded with $\sigma+$ helicity. After the helicity reversal, the magnetic domains change within the timescale of the XMCD image. Changing the laser helicity causes a domain wall motion that changes the magnetic contrast in the ring region from predominantly blue in Figure 4.13(a) to red in Figure 4.13(c). The temporal evolution of the domain wall motion can be traced by extracting the individual PEEM frames (see Figure 4.13(b1-b3)) from the intermediate state (Figure 4.13(b)). The white lines highlight the domain walls and the green lines (in Figure 4.13(b2-b3)) highlight the domain wall changes with respect to the previous image. The red domains grow at the expense of blue domains in the ring region when helicity is flipped from $\sigma-$ to $\sigma+$. The helicity dependent switching in the ring region occurs via thermally activated domain wall motion.

Further, the effect of the repetition rate of the laser on the switched ring region was investigated for a fixed laser helicity (Figure 4.14). The XMCD images were recorded at laser repetition rate of 125 kHz and 0.125 kHz with $\sigma-$ laser helicity that switches the ring region to blue. The area addressed by the laser helicity (blue ring region) decreases as the repetition rate is reduced from 125 kHz to 0.125 kHz as shown in Figure 4.14(a) and (b), respectively. Changing the repetition rate does not affect the energy per pulse imparted by the laser but increases the temporal distance between two consecutive pulses thus modifying the DC heat offset established by the laser. Figure 4.14(c) shows a schematic describing the DC heat accumulation in the two extreme cases of high and low repetition rates.

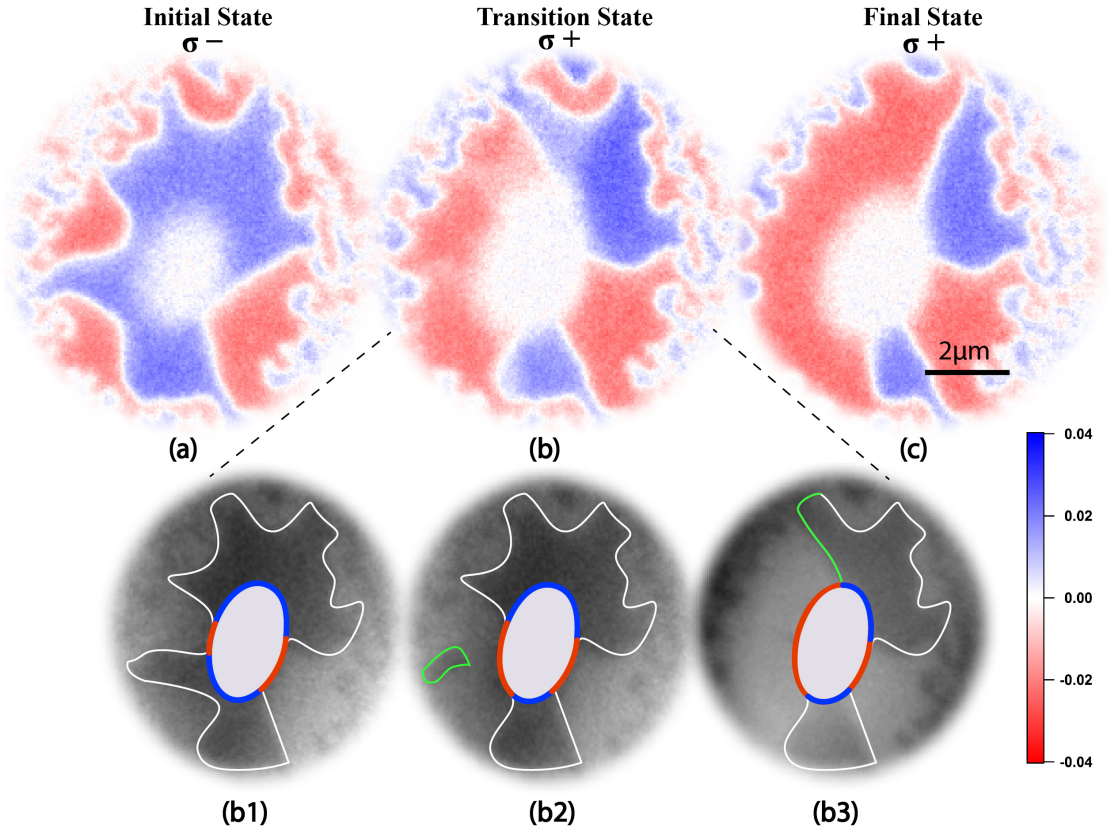

Figure 4.13: XMCD images recorded at Fe L_3 edge showing magnetic domains in Tb3010 around thermally demagnetized region when laser helicity is flipped from $\sigma-$ in (a) to $\sigma+$ in (b,c). (b1-b3) show PEEM images showing thermally induced domain wall motion. White boundaries mark the magnetic domains and the green boundaries mark the recent changes with respect to the previous image.

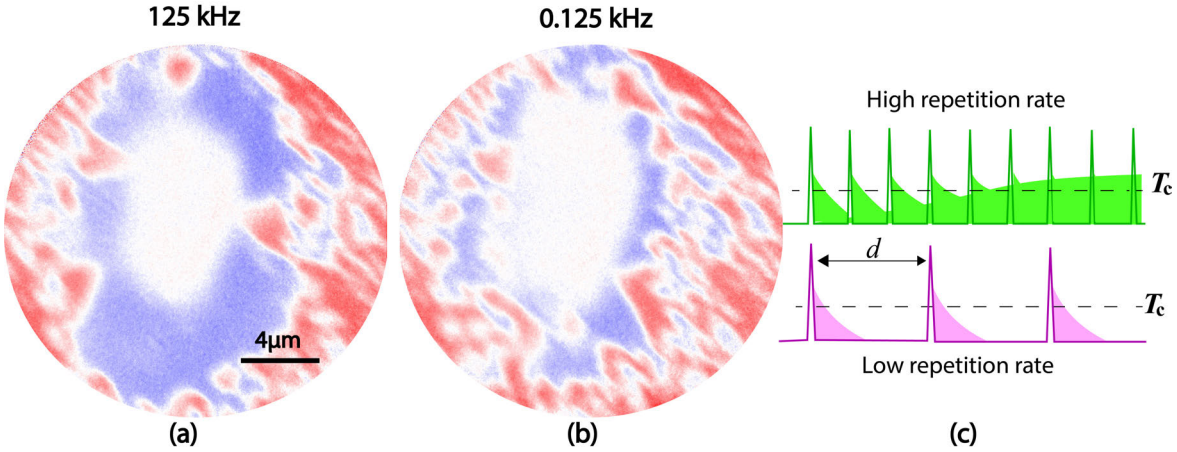

Figure 4.14: XMCD images recorded at Fe L_3 edge showing the modulation in the ring region with the repetition rate (a) 125 kHz and (b) 0.125 kHz of the laser in Tb3015. (c) Schematic showing laser pulses and heat transport in two extreme scenarios of high and low repetition rate.

The modulation in the width of the switched ring region with repetition rate indicates that the switching process is sensitive to the thermal energy in the ring region. To provide an estimate of the domain mobility due to thermal energy, Figure 4.15(a) shows an XMCD image with magnetic domains after a single pulse at 300 K. Increasing the temperature to 330 K without any laser exposure leads to domain wall depinning and a significant increase in domain size as observed in Figure 4.15(b). In this case, a mere increase by 30 K is enough for the domain walls to move around and form bigger domains.

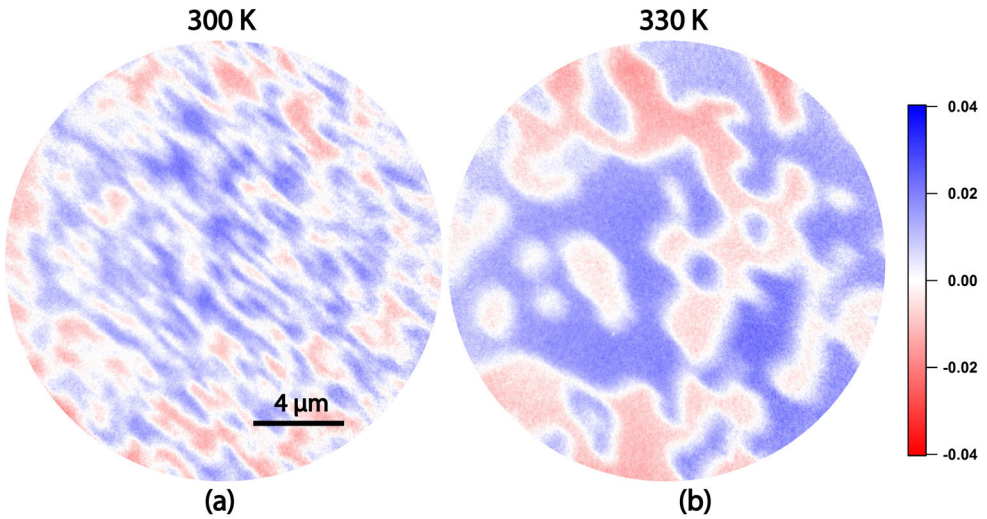

Figure 4.15: (a) XMCD images recorded at Fe L_3 edge showing magnetic domains after a single laser pulse at 300 K in Tb3015. (b) XMCD image showing the same region as in (a) with larger magnetic domains as a result of increased temperature of 330 K without any laser exposure.

The switching in the ring region is therefore understood in terms of a local heat profile established by the repetitive pulses of the laser. Each laser pulse causes local heating and if the next laser pulse arrives before the base temperature is reached by heat dissipation, then a DC offset in temperature is established. This local heat profile in the ring is dependent on the repetition rate of the laser. Figure 4.16(a) shows a schematic of the variation of temperature at the center of the illuminated region with each incoming pulse. Figure 4.16(b) shows this heat profile projected on the illuminated spot. The temperature in the demagnetized region rises above T_c and AO-HDS takes place at the region where the temperature is close to T_c. The local heat profile established in the irradiated spot is expected to lower the magnetic moment and increase the magnetic susceptibility of the sample. In such a state, a small stimulus is enough to promote the domain wall motion which can lead to the formation of bigger and stable domains.

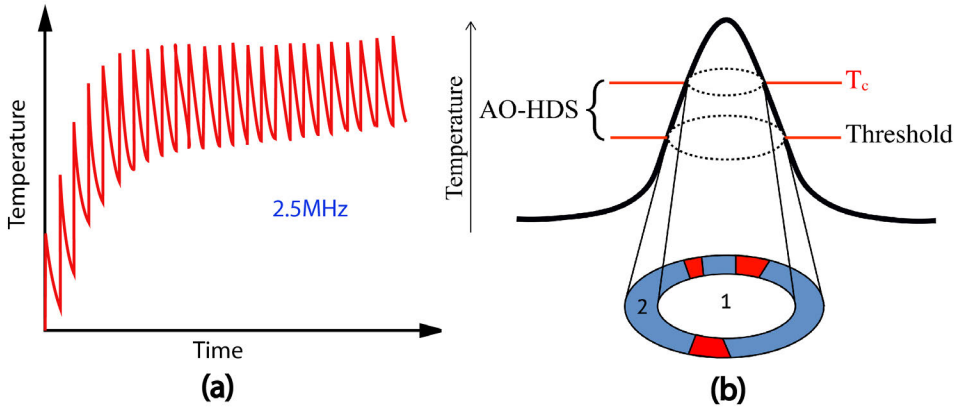

Figure 4.16: (a) Schematic showing temperature profile at the center of the laser illuminated spot as a function of time (laser pulses). (b) AO-HDS and the local temperature profile established on the sample in the pulse train mode.

In the previous studies, the switching process along a track (see Figure 4.17 (b)) where the laser beam was swept across the sample, can be understood as a domain wall motion [6, 16, 108]. This thesis aimed to examine the switching process via a stationary laser spot. However, if one considers the laser sweeping scenario, the domain wall motion observed in Figure 4.13 would lead to similar switched tracks. The magnetization would be switched in three steps: First, the inner core of the laser pulse (which results in thermal demagnetization for a stationary laser spot) would erase the magnetization by forming a demagnetized state and a local heat profile around it. This would be followed by switching in the outer ring region in accordance to the laser helicity. The moving laser would then drag the domains in the direction of the laser beam because of the high thermal energy in the ring. At the end of these sweeping tracks a thermally demagnetized region with a surrounding ring structure is expected (Figure 4.17(a)). Such demagnetized state are also observed in numerous experiments as shown in Figure 4.17 [6, 16, 108]. In essence, the domain wall motion plays an important role in the formation of these switched tracks.

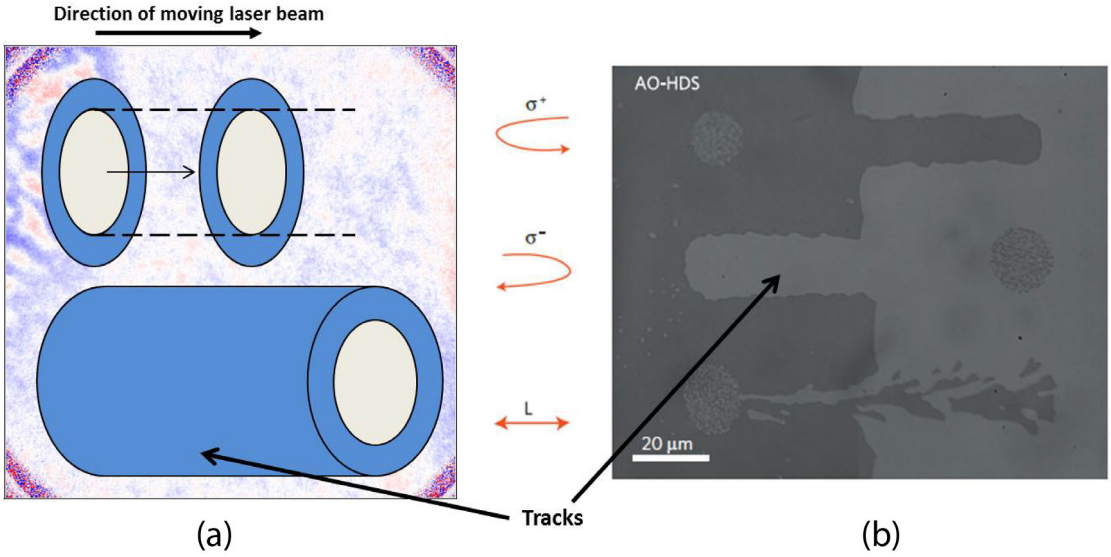

Figure 4.17: (a) Schematic showing the laser sweep tracks as observed in (b) which shows the magneto-optical image after the laser is swept on the sample with polarisation: from top to bottom, right circularly polarized light $\sigma+$, left circularly polarized light $\sigma-$ and linearly polarized light L. The dark and bright contrast refers to the two out of plane anti-parallel magnetic orientations. The figure on the right is adapted from [15].

AO-HDS is a local effect occurring in the vicinity of thermal demagnetization. The role of thermal demagnetization and laser heating is therefore undeniably an important parameter that severely affects the switching dynamics and efficiency of AO-HDS. It is essential to explore the effect of base temperature that is an important parameter for the total thermal energy of the sample. Two samples with different magnetic properties, Tb3010 and Tb3020 were investigated to study the impact of base temperature on the AO-HDS efficiency. Since the threshold fluence for AO-HDS decreases with increasing base temperature, the laser fluence was adapted to keep the maximum temperature reached at the center of the laser spot constant and independent of the base temperature. This was ensured by maintaining a constant spatial size of the thermally demagnetized region as a function of temperature during each measurement. Figure 4.18 (a,b) and (c,d) show AO-HDS by laser of opposite helicities in a ring shaped region at 300 K and 220 K respectively for Tb3020. Similarly, Figure 4.18(e,f) and (g,h) show AO-HDS by laser of opposite helicities in a ring region at 260 K and 180 K, respectively, for Tb3010. As shown in the figure, the efficiency of AO-HDS decreases at a lower temperature where the contrast in the switched ring region starts to disintegrate into random magnetic domains.

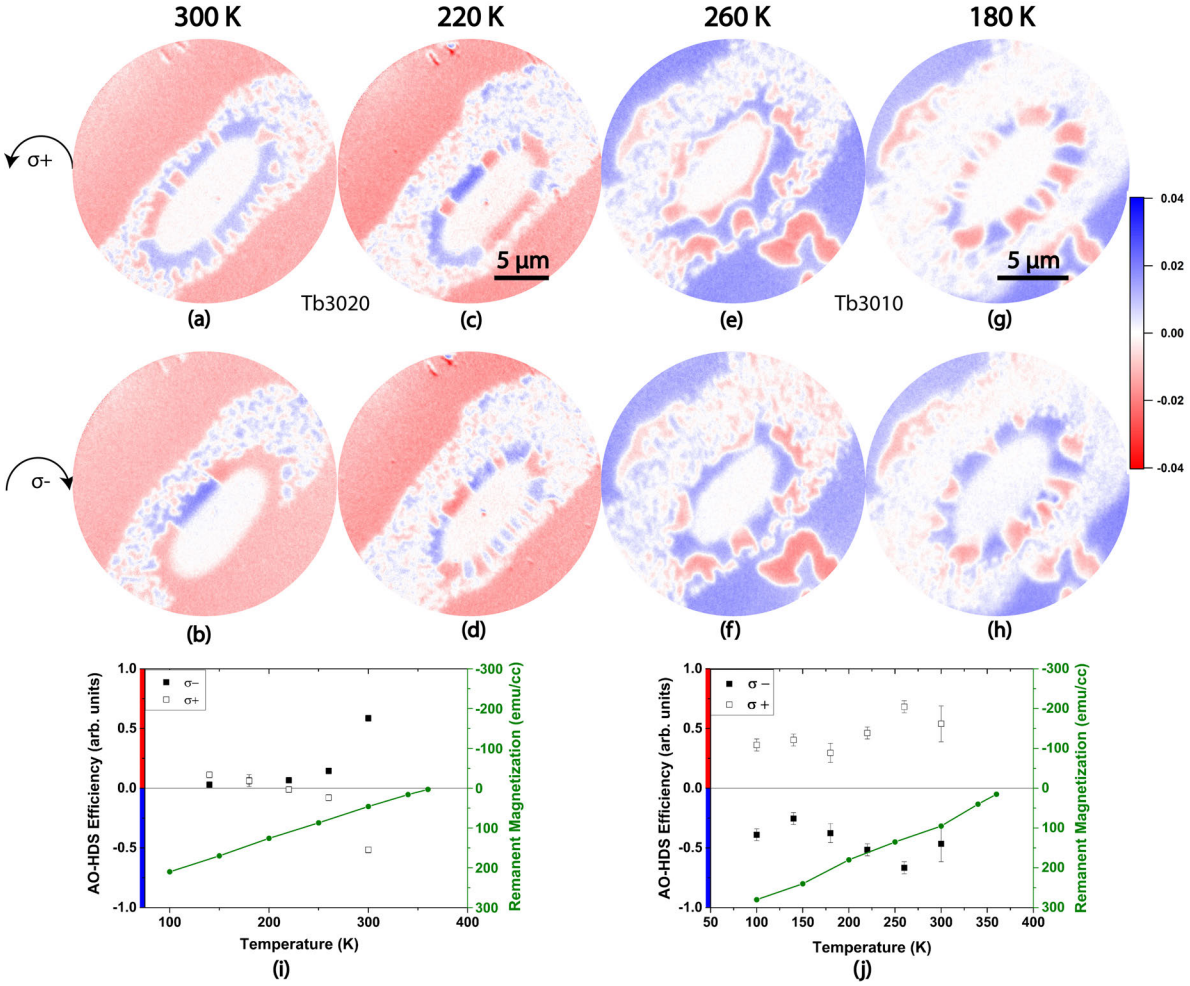

Figure 4.18: (a,b), (c,d) XMCD images recorded at Fe L_3 edge showing AO-HDS with opposite helicities at 300 K and 220 K respectively for Tb3020 film. (e,f), (g,h) XMCD images showing AO-HDS with opposite helicities at 260 K and 180 K, respectively, for Tb3010. (i,j) Plots showing the AO-HDS efficiency as a function of base temperature and the corresponding remanent magnetization (green axis) for Tb3020 and Tb3010, respectively.

To quantify the efficiency of AO-HDS at different base temperatures, the ratio of the difference between the length of the circumference (L) of the ring covered in blue and red domains normalized to the total ring circumference is evaluated:

$$\text{Efficiency} = \frac{L_{red} - L_{blue}}{L_{red} + L_{blue}} \tag{4.3}$$

where L_{red} and L_{blue} are the length of the circumference of the ring covered by red and blue contrast, respectively. An efficiency ratio of 1(-1) would imply that the whole ring is surrounded by red (blue) magnetization, i.e. a 100% AO-HDS efficiency. If the ratio

is 0, this would imply a $50-50\%$ distribution of red and blue magnetization accounting for a purely random switching behavior.
The temperature dependent efficiency of AO-HDS is plotted in Figure 4.18(i) and (j) for Tb3020 and Tb3010, respectively. Filled and the open squares represent opposite laser helicities.
For pulse trains, the local heat profile around the demagnetized region is significantly affected by the base temperature. The thermal gradient across the ring is determined by the peak temperature reached by the laser in the center and the base temperature of the sample. Changing the thermal gradient by the base temperature influences the domain size and domain wall mobility. The disintegrated domains in the ring structure at low base temperatures are a consequence of higher thermal gradient. It was argued by Hassdenteufel *et al.* that the materials with low remanence have higher switching efficiency [97]. In this context, the efficiency data is compared with remanent magnetization vs. temperature data measured by SQUID-VSM. The green axis in Figure 4.18(i) and (j) shows the remanent magnetization data vs. temperature for Tb3020 and Tb3010, respectively. For the Tb3020 film, a reasonable agreement between the AO-HDS and remanence is observed as its remanent magnetization decreases at a higher temperature. However, for Tb3010, no clear correlation between the temperature dependence of AO-HDS efficiency and remanent magnetization is observed. This disagreement is not too surprising considering that AO-HDS occurs only in a ring-shaped region around the demagnetized region. Inside the ring region the temperature is at least temporarily just below T_c after each laser pulse. Thus the remanent magnetization at base temperature would have little impact on the switching behavior. For initiating a helicity dependent switching process, a higher base temperature is favorable as it facilitates domain wall motion.

4.5 Relaxation effects

Till now in this thesis, imaging in the pulse train measurements was carried out while the laser was still interacting with the sample. However, in order to have a technological application, the switched magnetic state is required to be stable even after the laser is removed from the illuminated spot. In the presence of the laser, the switched ring state is embedded in a local heat profile with a thermally demagnetized region in the center. After blocking the laser exposure, the local temperature relaxes to the base temperature of the surrounding film. This relaxation affects the switched ring region as the domain formation takes place in a previously demagnetized spot.

The laser exposure is obstructed by mechanically blocking the laser from illuminating the sample. Figure 4.19 depicts the relaxation effect in Tb3010 sample. The red and blue ring region (marked with black boundary) observed with $\sigma+$ and $\sigma-$ helicities, respectively (Figure 4.19(a,c)) are preserved (Figure 4.19(b,d)) after blocking the laser. In addition, a random multi-domain pattern is formed as shown in Figure 4.19(b,d) within the previously thermally demagnetized region.

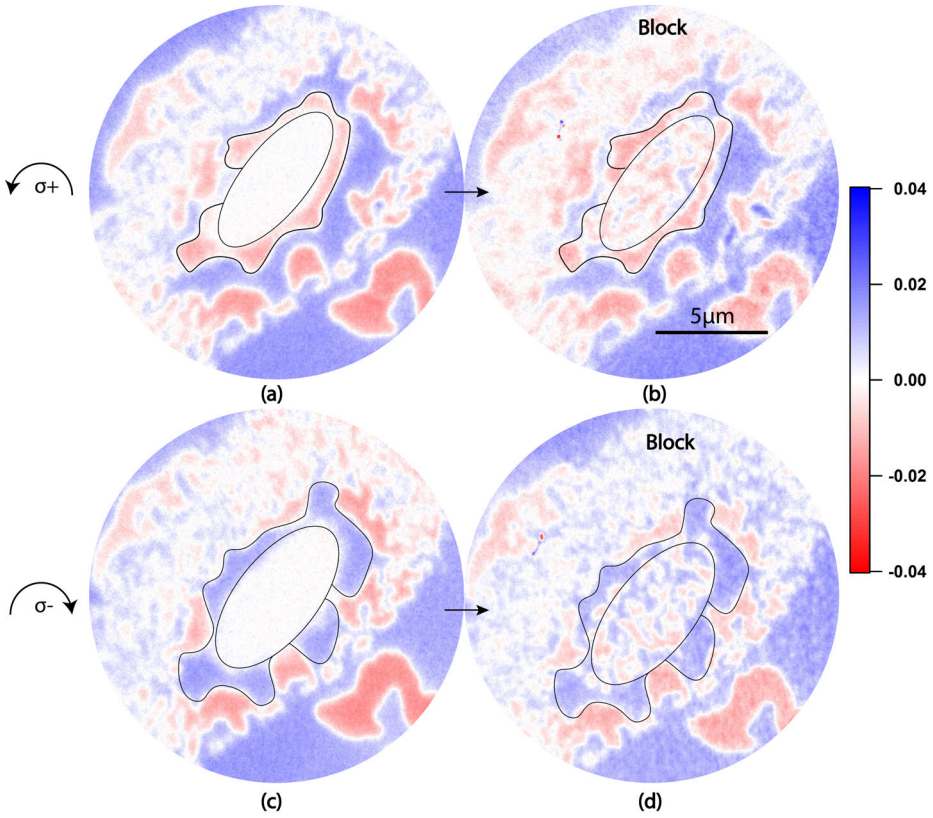

Figure 4.19: (a,c) XMCD images recorded at Fe L_3 edge showing the initial state with pulse train laser exposure (b,d) XMCD images showing the relaxation effects after blocking the laser in sample Tb3010.

Domains established in the ring region are preserved after blocking the laser. An abrupt blocking of the laser exposure forms small domains in the previously thermally demagnetized region which do not have enough energy to coalesce into each other. However, if the laser fluence is slowly decreased to zero instead of an abrupt blocking of the illumination, the thermal energy decreases in a gradual manner allowing the domains to drag and merge. Such an example is shown in Figure 4.20(a) where the inner region in the initial state is entirely switched to blue in Figure 4.20(b) after the laser fluence has been 'swept' to zero. Please note that the domains highlighted by the dotted curves in the ring region are preserved.

In general, the relaxation effect does not hamper the domains in the switched ring region. The final state depends on the cooling time of the sample. In an abrupt cooling process, a random multi-domain formation takes place within the demagnetized region. A slower cooling process allows the domain walls drag to form larger switched domains. The cooling process is directly related to the sample parameters like the thickness of the films and heat conductivity across the sample. In addition, the magnetic properties of the sample like remanent magnetization and demagnetization energy are also influential.

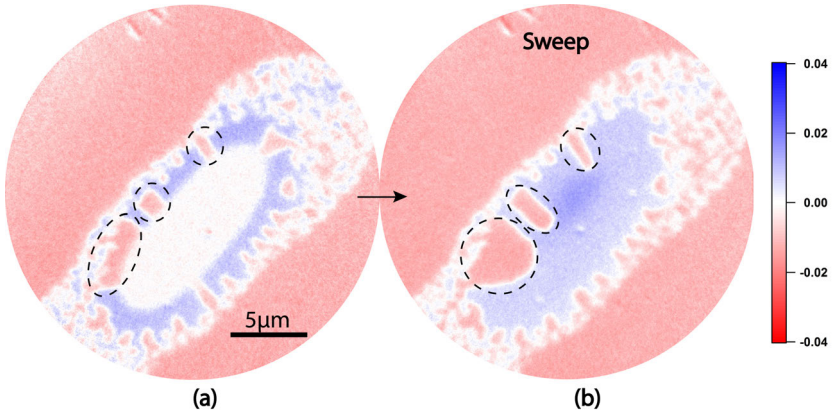

Figure 4.20: (a) XMCD images recorded at Fe L_3 edge showing the initial state with pulse train laser exposure (b) XMCD images showing the relaxation effects after sweeping the laser fluence to zero in sample Tb3010.

4.6 Equivalent magnetic field of AO-HDS

AO-HDS switches the magnetization of the sample deterministically according to the circular helicity of the laser pulses. Essentially, it replaces the conventional stimulus of a magnetic field with laser helicity to control the magnetization orientation. Therefore, it is essential to estimate the magnitude of the magnetic field required to negate the effect of laser helicity in AO-HDS. For this purpose, PEEM measurements were carried out in an out-of-plane DC magnetic field in the pulse train mode. Prior to every measurement, the magnetic state was reset to a random multi-domain pattern via a single laser pulse with high laser fluence. The DC magnetic field was applied throughout the measurement whereas the sample was exposed to laser for merely 60 fs for each pulse in the pulse train mode. Figure 4.21(a,b) shows XMCD images depicting AO-HDS with preferential magnetic contrast of blue and red in the ring region with opposite helicities $\sigma+$ and $\sigma-$ in zero external magnetic field. On application of +16 Oe, the magnetic contrast in the ring region changes to blue in Figure 4.21(c,d), irrespective

of the laser helicity. Similarly, an opposite magnetic field of −16 Oe facilitates the switching orientation to red in the ring region in Figure 4.21(e,f).
Lambert *et al.* showed that an external magnetic field of ∼ 700 Oe is required to suppress the effect of laser helicity in a 15 nm FePtAgC granular film [16]. However, as observed in Figure 4.21, a modest field of 16 Oe is enough to negate the effect of laser helicity in TbFe thin films. The coercive field for Tb3010 is around 3000 Oe at room temperature. The significantly lower value of magnetic field to negate the effect of laser helicity suggests that a small bias is required to switch the magnetization at elevated temperatures near T_c.

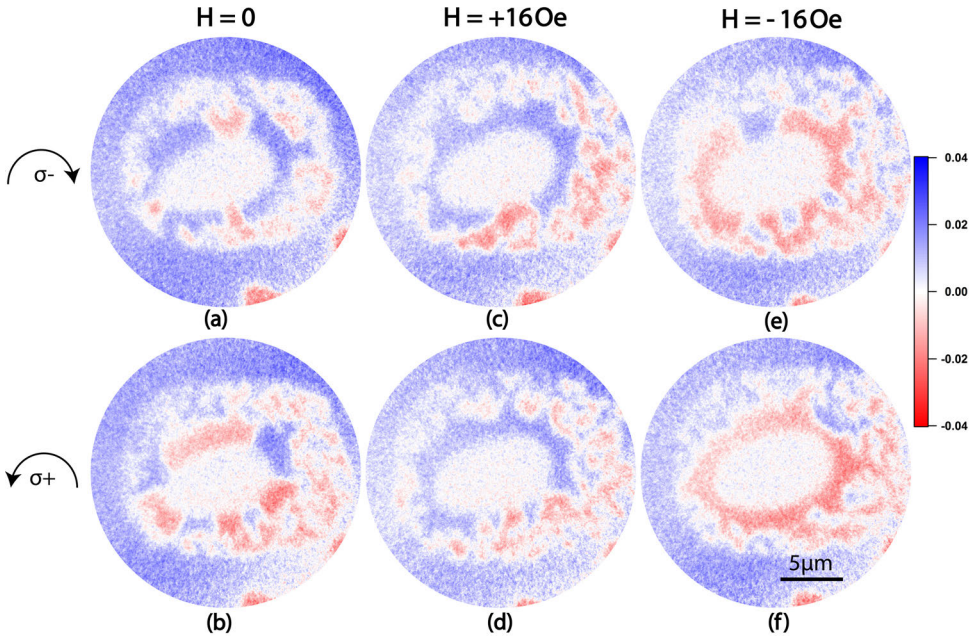

Figure 4.21: (a,b), (c,d), (e,f) XMCD images recorded at Fe L_3 edge showing AO-HDS in presence of external out-of-plane magnetic field H = 0, +16 Oe ,−16 Oe, respectively with opposite laser helicity. The application of +16 Oe/−16 Oe favors the formation of blue/red magnetic contrast in the ring region. A single pulse is applied prior to every measurement.

4.7 Thickness dependent magnetization reversal in AO-HDS

To study the sample thickness dependence of AO-HDS efficiency, switching experiments were performed on two thin films of same alloy composition (30% Tb) but with different film thickness (10 nm and 20 nm): Tb3010 and Tb3020. Both samples were exposed to laser pulses with a repetition rate of 2.5 MHz. Figure 4.22 shows XMCD images

showing the switched ring region in pulse train mode for Tb3020 (a,b) and Tb3010 (c,d) by opposite circular laser helicities $\sigma+$ and $\sigma-$. The switching orientation in the ring region for $\sigma+(\sigma-)$ reverses from mostly red(blue) (Figure 4.22(a,b)) to mostly blue(red) (Figure 4.22(c,d)) as the film thickness is increased from 10 nm to 20 nm. This inversion of the switching orientation with film thickness is a novel observation and has not been reported before. For a better understanding of this intriguing thickness dependence, the switching behavior was investigated for samples with a different Tb concentration of 22%: Tb2210, Tb2220, Tb2240, Tb2260 and Tb2280 which have different film thickness and thus different magnetic properties. As shown in Figure 4.23, the switching orientation with a particular laser helicity ($\sigma+$) inverts at a threshold film thickness between 10 and 20 nm.

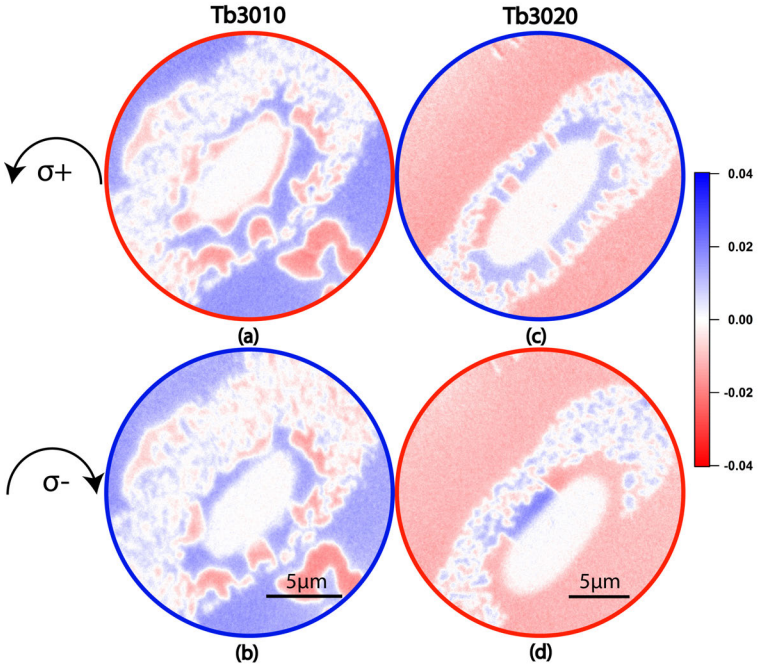

Figure 4.22: (a,b) XMCD images recorded at Fe L_3 edge depicting AO-HDS for 20 nm thick film of Tb3010 illuminated by $\sigma+$ and $\sigma-$ respectively. (c,d) XMCD images depicting AO-HDS for 10 nm thick film of Tb3020 illuminated by $\sigma+$ and $\sigma-$, respectively.

The observed thickness dependent inversion is independent of alloy composition since the same inversion of switching orientation was also observed for samples with 22% Tb concentration. Despite the variance in the dominant sublattice at room temperature, T_M, magnitude of remanent magnetization and coercivity, the switching direction seems to only depend on the film thickness.

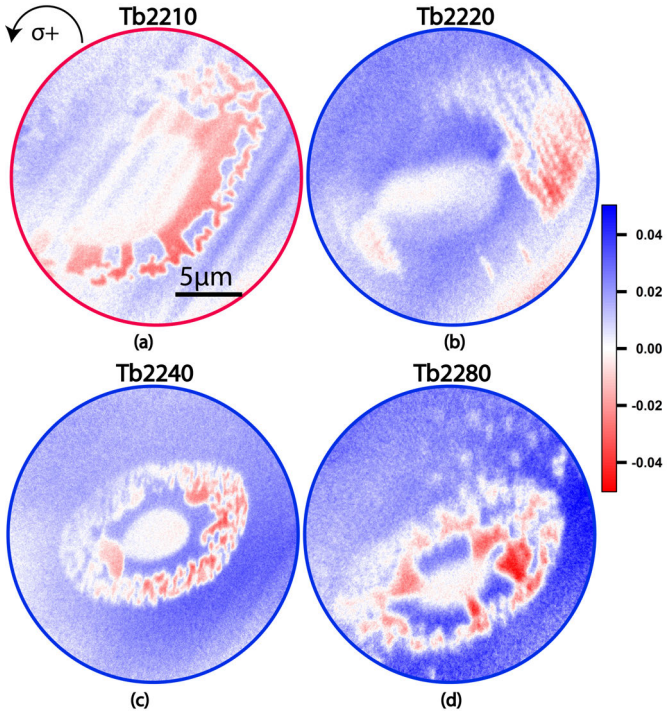

Figure 4.23: (a-d) XMCD images recorded at Fe L_3 edge depicting AO-HDS illuminated by $\sigma+$ for samples Tb2210, Tb2220, Tb2240, and Tb2280 respectively. The switching orientation with a particular helicity inverts above a threshold film thickness between 10 and 20 nm.

Figure 4.24 enlists all the investigated samples with variable thicknesses and their respective switched directions with $\sigma+$ laser helicity measured at the Fe L_3-edge. This shows a clear inversion in switching orientation depending only on film thickness. It is indeed remarkable that a clear switching in the ring region in films with thickness as high as 80 nm is observed even though the demagnetization energy is expected to increase in thicker films.

σ+	$Tb_{30}Fe_{70}$	$Tb_{22}Fe_{78}$
10 nm	Red	Red
15 nm	Red	
20 nm	Blue	Blue
40 nm		Blue
60 nm		Blue
80 nm		Blue

Figure 4.24: The table shows the switching direction for different samples measured at Fe L_3 edge for a fixed laser helicity $\sigma+$.

To investigate the origin of the thickness dependent behavior, the magnetization dependent changes on transmission (T) and reflectivity (R) for TbFe samples at room temperature were measured by a separate laser experiment. The individual contribution of transmission and reflectivity in TbFe samples are plotted as a function of film thickness in Figure 4.25. The resulting total MCD effect is calculated in terms of absorbed laser energy by subtracting the reflected and transmitted parts from the total incoming intensity. Although the MCD is expected to be higher for thinner films, the total MCD signal decreases as a function of the film thickness. The laser fluence in the PEEM experiments was much higher than that in reflectivity measurements. Therefore, near T_c, the variation of MCD with film thickness might differ in AO-HDS.

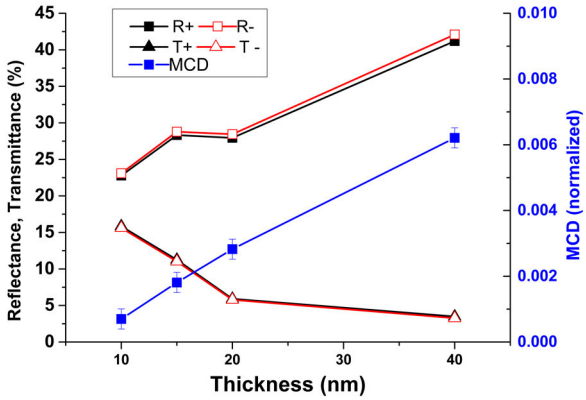

Figure 4.25: Plot showing the measured reflectivity, transmission and asymmetry in absorbed laser power for opposite magnetization due to total MCD effect as function of sample thickness.

4.8 Space-time-resolved AO-HDS

To study the dynamics of the switching mechanism, space and time-resolved pump-probe measurements were performed. The laser pulses were synchronized with X-ray pulses and XMCD images were recorded as a function of time delay between laser and X-ray pulse. The laser was operated at a repetition rate of 1.25 MHz where the duration between two consecutive pulses is 800 ns. Figure 4.26 shows XMCD images recorded at negative and positive time delays at two temperatures 350 K and 300 K in an out-of-plane magnetic field of 10 Oe and zero field, respectively.

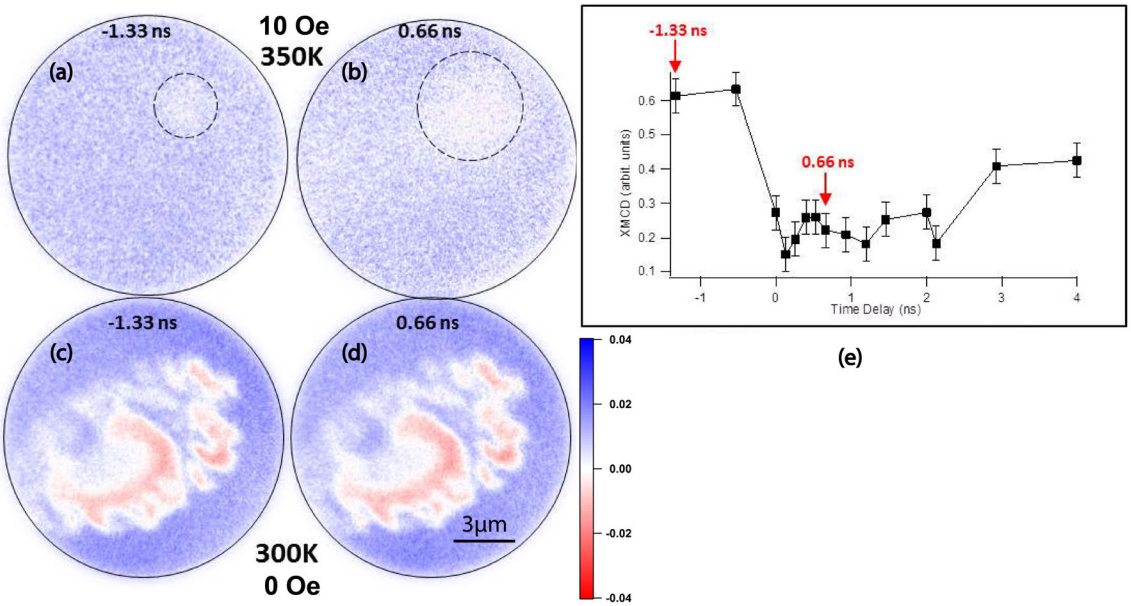

Figure 4.26: (a,b) XMCD images recorded at Fe L_3 edge at a time delay of -1.33 ns and 0.66 ns between laser and X-ray pulse at 350 K in the presence of an out-of-plane magnetic field of 10 Oe in Tb3015. (c,d) XMCD images recorded at time delay of -1.33 ns and 0.66 ns between laser and X-ray pulse at 300 K in zero magnetic field. (e) Plot showing the time evolution of magnetic contrast in the bubble domain in (a,b).

At an elevated base temperature of 350 K, the magnetic susceptibility is significantly larger and the TbFe film orients in a weak external field of only 10 Oe. Local demagnetization by each laser pulse leads to the formation of a magnetic bubble domain which is unstable and collapses over time. Figure 4.26(a,b) displays the evolution of magnetic contrast in this bubble domain as the laser pulse arrives on the sample. The local magnetization dynamics can be followed as the bubble domain grows and reduces in size with time. The magnetic contrast inside the illuminated sample spot (extracted from the XMCD image) is plotted as a function of the time delay in Figure 4.26(e). The size of the bubble domain increases as soon as the laser pulse arrives and then decreases substantially within few nanoseconds. However, the magnetization has not recovered completely even after 800 ns as the bubble domain is still observed (Figure 4.26(a)). At 300 K (see Figure 4.26(c,d)), beginning from a multi-domain state, no visible variation in magnetic contrast around the thermally demagnetized region is observed. This is because the stochastic nature of the switching behavior does not allow to observe any changes in a time-resolved experiment. Once the inner demagnetized region and the local heat profile in the ring are established, the domains in the ring switch via domain wall motion. These large domains in the ring region become stable and further laser pulses only demagnetize a small part of the ring near T_c which is extremely difficult to be observed in such an experiment.

Since the changes near the thermally demagnetized region were too small to be detected in the stroboscopic experiment, another experiment was performed to overcome this limitation. Figure 4.27(a) shows the initial magnetic state in the pulse train mode (red switched magnetization in the ring region) by $\sigma-$ laser helicity. Thereafter, the laser helicity was switched back and forth every 3 seconds while recording about 400 PEEM images with fixed X-ray polarization ($c+$) to improve the statistics. The PEEM images recorded with $\sigma+$ and $\sigma-$ were extracted separately and averaged. Figure 4.27(b) shows the difference between the average of 200 PEEM images of $\sigma+$ and $\sigma-$ each. The contrast in Figure 4.27(b) represents the average changes between the magnetization of the sample illuminated by $\sigma-$ and $\sigma+$. As observed in Figure 4.27(b), the magnetic changes are limited to a narrow ring around the demagnetized region and the maximum intensity is concentrated at the domain walls as highlighted by the arrows in Figure 4.27(a,b). By comparing the dotted ring between (b) and the XMCD image of (a), it is evident that the width of the active region in Figure 4.27(b) is significantly smaller than that of the ring region where AO-HDS takes place in Figure 4.27(a).

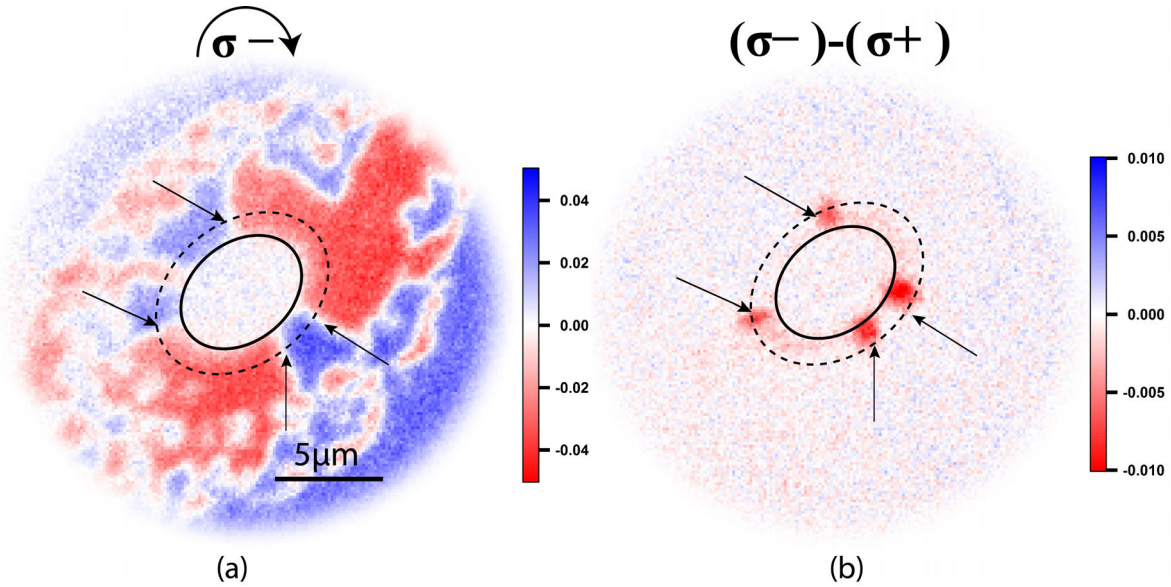

Figure 4.27: (a) XMCD image of Tb2260 recorded at Fe L_3 edge showing AO-HDS in pulse train mode with red ring region illuminated by $\sigma-$ laser helicity. (b) Average difference between PEEM images (acquired with fixed X-ray polarization) recorded with laser light of opposite helicities $\sigma-$ and $\sigma+$.

The outcome of the experiment can be explained by a combination of MCD and thermally activated domain wall motion. Consider the schematic shown in Figure 4.28(a) which shows a switching scenario similar to Figure 4.27(a). Due to MCD, the blue orientation absorbs more energy than red by $\sigma-$ helicity. Consequently, the blue orien-

tation heats up to a higher temperature near T_c and gets preferentially demagnetized and (Figure 4.28(b)) making the red orientation more stable. The blue orientation switches stochastically to red or in other words, the red domain grows at the expense of blue domains (Figure 4.28(a)). When the sample is illuminated by $\sigma+$ helicity, the red orientation absorbs more energy than blue and is more demagnetized as shown in Figure 4.28(d) and now the blue domain grows at the expense of red (Figure 4.28(c)). The repeated inversion of helicity back and forth from $\sigma-$ to $\sigma+$ results in the domain wall motion only near the red-blue domain boundary. The difference image in Figure 4.28(e) represents the changes occurred in the domains with repeated helicity flipping. The highest contrast at the red-blue domain boundary represents the domain wall motion and is limited to a narrow width indicating that MCD induced switching only occurs in the vicinity of a thermally demagnetized region (near T_c). The faint contrast in the narrow ring in Figure 4.28(e) is proportional to the MCD effect in the sample. Figure 4.27 proves that the helicity information is only transmitted near T_c.

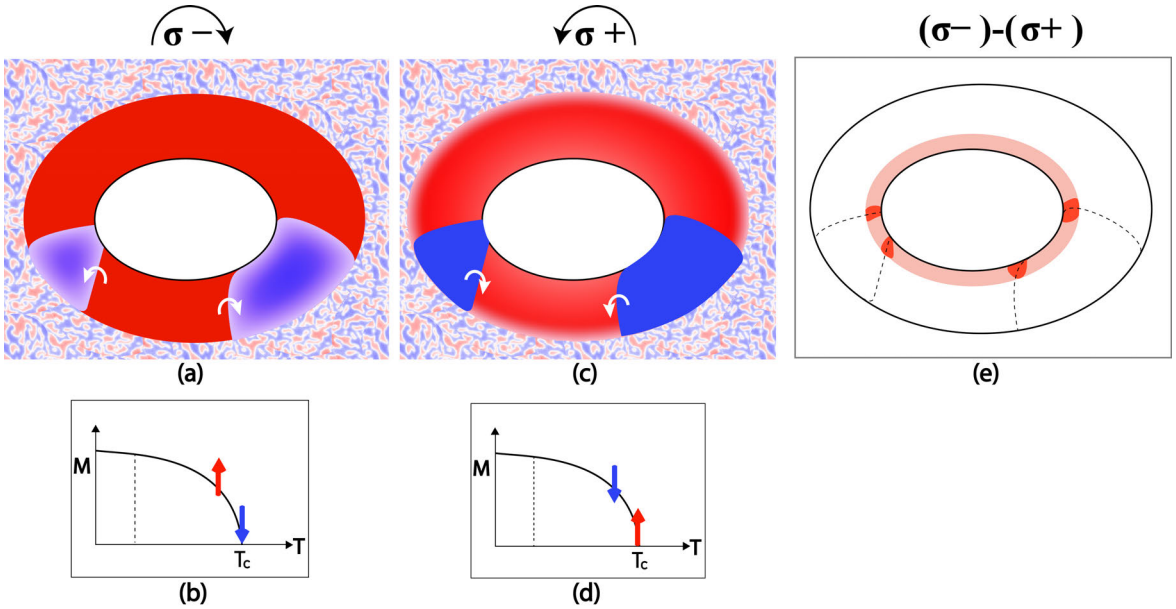

Figure 4.28: Schematic showing (a,c) XMCD image when the sample is illuminated by $\sigma-$ and $\sigma+$ laser helicity, respectively. (b,d) Magnetization vs. Temperature curve showing the selective demagnetization of blue and red domain orientation by $\sigma-$ and $\sigma+$ laser helicity, respectively due to MCD effect. (e) Average difference between PEEM images (acquired with fixed X-ray polarization) recorded with laser light of opposite helicities $\sigma-$ and $\sigma+$.

4.9 Discussion

As shown in section 4.4, the phenomenon of AO-HDS is a local effect within a stationary laser spot occurring in a ring-shaped region in the vicinity of thermal demagnetization. The switching in the ring region takes place by thermally activated domain wall motion. One domain orientation expands at the expense of the other determined by the laser helicity. The width of the switched ring region addressed by the laser can be manipulated by changing the repetition rate of the laser. Such modulations of the size of the switched area by changing the repetition rate could potentially offer a great advantage in switching smaller bit sizes for technological applications.

The switching is essentially a stochastic process that can only take place near T_c where the magnetic susceptibility of the sample is drastically reduced. The local heat profile established in the ring region facilitates the switching by thermally activated domain wall motion. The thermal gradient across the ring also influences the width of the switched ring structures. In this context, heat conductivity across the sample is also influential. The importance of thermal energy has also been highlighted in a recent study [109] where magnetic domain changes of Co in response to femtosecond laser pulses have been considered as a process of laser-induced de-pinning and thermally activated domain wall motion. In another study, the switching in ferrimagnets like TbCo has been depicted as a 'two-step' process using Hall probe measurements where the first step leads to helicity independent multi-domain formation in 1 ms followed by helicity dependent gradual re-magnetization within 100 ms [108]. While the importance of T_c and laser heating was always a matter of debate, the experimental evidence from the high-resolution data in this thesis provides an unambiguous picture for the necessity to reach T_c.

It has been argued that the helicity dependent switching is dependent on the remanent magnetization and the domain-size given by the film thickness [35, 97, 105]. Figure 4.24 shows that AO-HDS is observed for a wide range of thickness ranging from $10 - 80$ nm. The claims about the criterion of low remanent magnetization and domain size are misleading because the measurements are convoluted with the relaxation effects after the laser is removed from the sample [97, 105]. Parameters like remanent magnetization and domain-size are dependent on the film thickness and demagnetization energy which only matters when the laser exposure to the sample is stopped. However for a stationary laser spot, the helicity dependent switched domains in the ring region are stable as observed in Figure 4.20, irrespective of the film thickness. In this context, the measurements performed in this thesis provide a clear picture about the relevant parameters responsible for an efficient switching process.

Section 4.7 showed that the switching orientation with a particular laser helicity inverts at a threshold film thickness. There have been studies claiming that the switching direction in ferrimagnets depends on the magnetic orientation of an individual sublattice rather than the total magnetization of the film [110]. In essence, they argue that the laser helicity interacts with the individual Fe sublattice and orients its magnetic orientation. This is indeed true if the samples with different dominant sublattices and constant film thickness like in previous studies (Tb3010 and Tb2210) are compared. In both films, a particular laser helicity switches the Fe sublattice in the same direction. In such experiments, an additional thickness dependence should also be considered as the switching orientation depends on the film thickness. The inversion of the switching direction at a threshold film thickness has not been observed so far and is rather surprising. It most likely indicates the presence of two competing mechanisms with different dependence on thickness that contributes to AO-HDS. The two most discussed and debated fundamental explanations given for AO-HDS are Inverse Faraday Effect (IFE) effect and Magnetic Circular Dichroism (MCD).

The theory of IFE was formulated for transparent crystals with small notable dissipation. However, the primary interest for applications lies in ferromagnetic metallic thin films where the thermal effects are significant and cannot be neglected. Although IFE has been proposed as the microscopic mechanism for AO-HDS in ferromagnetic metals, a complete theory for IFE in metallic films is still missing [111–115]. The theoretical models of IFE either do not include or do not explain the implications of dissipative systems such as metallic thin films. In addition, the strength and the duration of the magnetic field pulse generated by laser light to be able to switch the magnetization are still under debate [81, 91, 115, 116]. The values vary from $0.1 - 20$ T for the amplitude and 0.1 ps to several ps for the duration of the magnetic field pulse [117]. Figure 4.21 showed that the magnitude of the magnetic field to negate the effect of laser helicity in the switching process is about 16 Oe. The direct transfer of angular momentum from the light to the magnetic system by IFE is expected to be most effective near T_c. Even if it is possible to generate enough momentum for switching near T_c, IFE alone is incapable of explaining the thickness dependent inversion of the switching orientation as observed in Figure 4.24. The angular momentum generated by a particular laser helicity should switch the magnetization in a similar way independent of the film thickness.

The MCD effect refers to the preferential demagnetization of one magnetization orientation at temperatures close to T_c due to a small magnetization dependent difference in the absorption cross section [99, 118, 119]. Figure 4.29 shows a schematic of the MCD effect. The laser increases the local temperature of the sample close to T_c leading to a

significant decrease in the magnetic anisotropy. The black domain ($\boldsymbol{M}$ down) absorbs more laser energy than the white domain ($\boldsymbol{M}$ up) by a particular helicity via MCD. In this case, the preferentially demagnetized black domain is less stable than the white domain because of its higher temperature. Thus, the black domain has a higher probability to switch to a white domain. Similarly, opposite laser helicity preferentially demagnetizes the white domain.

The MCD effect is anticipated to drive AO-HDS only near T_c. The necessity of being near T_c and the resulting thermally demagnetized region are evident by our experimental observation of AO-HDS which takes place only in the ring surrounding the thermally demagnetized region. Moreover, the switching is observed to be stochastic and cumulative in nature. Our observation of stochastic switching mediated by thermally activated domain wall motion in the ring region further favors the MCD as underlying microscopic mechanism. Consequently, single pulse helicity dependent switching has not been observed yet in any of the ferrimagnetic or ferromagnetic material except GdFeCo where switching is driven by formation of a transient ferromagnetic state due different demagnetization timescales of the Gd and Fe sublattices [93].

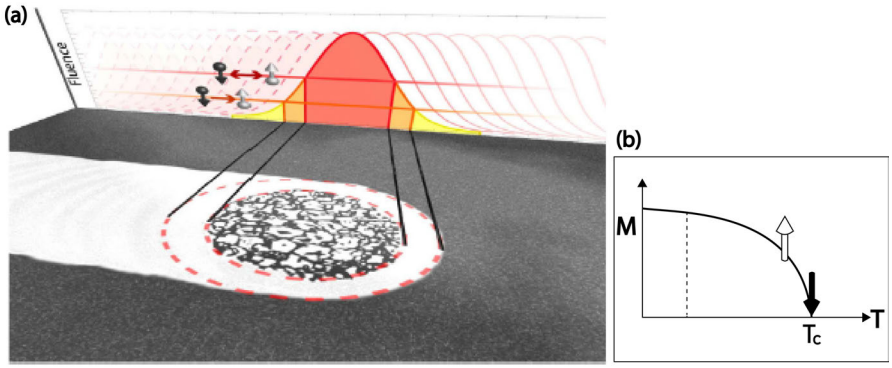

Figure 4.29: Schematic showing helicity dependent switching with multiple laser pulses. The figure is adapted from [99]. (b) Magnetization vs temperature curve showing selective demagnetization of black (down) magnetization orientations due to the MCD effect.

In the light of the results showing the thickness dependent inversion of switching orientation, understanding AO-HDS via MCD is crucial. MCD is understood by preferential demagnetization of one magnetic orientation close to T_c. This effect is based on a local variation of the absorption cross section by MCD which reduces as the film thickness increases. MCD in absorption is expected to be maximum in thinner films with thickness less than the absorption length of the laser. In thicker films, most of the laser power is absorbed by the TbFe film and the deposited laser energy begins to match the intensity

profile of the laser and no longer vary with the orientation of magnetic domains. With differential absorption via MCD, no AO-HDS is expected for the thickness above the absorption length of the laser.

Our observation of AO-HDS up to 80 nm thick TbFe films (Figure 4.23(d)) (which is well above the absorption length of the laser ($\sim$ 20 nm)) is intriguing. In addition, the novel behavior of inversion of switching orientation with a particular helicity at a threshold film thickness is observed (Figure 4.22, 4.23). Conventionally only the absorption effects are considered in MCD. However, MCD affects not only the absorption but also the local reflectivity of the sample. Reflectivity also changes with the magnetization direction in the presence of MCD. It increases with the film thickness and is opposite to the above mentioned MCD effect in absorption.

The total MCD effect as observed in Figure 4.25 was almost zero for thin films and increased with thickness. However, the MCD signal does not change the sign below absorption length of the laser ($\sim$ 20 nm). This is because the absorption and reflectivity have opposite sign and almost compensate each other for thin films. In thicker films, the magnetization dependent changes in reflectivity dominate, as the contributions of the absorption to the MCD effect vanishes. Unfortunately, the conditions between reflectivity and the PEEM measurements could not be matched in terms of the laser fluence and temperature gradients. But the observed trend indicates that the contributions of reflectivity to the MCD effect might be responsible for AO-HDS in the thicker TbFe films. The reversed helicity dependence in 10 nm thick films suggests a second mechanism that dominates below the attenuation length of laser light. This could be the enhanced contributions of absorption to the resulting MCD effect even though no sign reversal in the resulting total MCD effect is observed.

The results shown in Figure 4.27 further strengthen the claim for MCD as a microscopic mechanism. It has been shown that the MCD effect of 0.5-2% is enough to initiate a helicity dependent switching [99, 119]. Therefore a small preference set by an external magnetic field should suffice to negate the helicity dependent switching mediated by MCD effect near T_c.

Chapter 5

Control of magnetism via electric field in $Fe/BaTiO_3$

This chapter describes the voltage induced changes in the local magnetic anisotropy and magnetic domain pattern of a wedge shaped Fe film with variable thickness deposited on a ferroelectric (FE) $BaTiO_3[001]_{pc}$ (BTO) single crystal substrate. The first section 5.1 provides a brief overview of the state-of-the-art of electric field manipulation of magnetism in artificial multiferroic heterostructures. Section 5.2 characterizes the chemical, magnetic, and structural properties of the as-grown Fe wedge sample on a BTO single crystal. With the help of XPEEM and XMCD, section 5.3 discusses the evolution of magnetic domain patterns in response to an external out-of-plane voltage close to room temperature. Section 5.4 shows that electric field switches on the long-range ferromagnetic ordering at localized sample locations for which any magnetic ordering was previously absent. This key observation is associated to an electric field induced superparamagnetic to superferromagnetic transition which is discussed in Section 5.5.

5.1 Overview

Electric field control of magnetism in multiferroic materials has attracted significant interest in the past few years driven by its enormous potential for application in low-power spintronics, voltage-driven non-volatile memory, and microwave devices [18, 120–124]. While a large magnetoelectric (ME) coupling at room-temperature in single phase multiferroic materials is difficult to realize, artificial multiferroic heterostructures remain the target materials for applications as the T_c of the magnetic and ferroelectric components can be selected by chosing the appropriate compounds. In thin film heterostruc-

tures, the ME effect can take place via different mechanisms at the interface [18,122] involving a modulation of carrier density in the ferromagnetic (FM) component [125,126], strain mediated ME coupling [7,127], exchange-bias coupling [128], and orbital reconstruction [21,129]. With these mechanisms, the manipulation of magnetic properties such as the magnetic domain structure, magnetic anisotropy, critical temperatures for phase transitions, and spin-polarization have been reported [8,11,13,130].

The magnetic properties of itinerant FM materials are largely influenced by the density of the itinerant electrons. On application of an external electric voltage, charge carriers accumulate or deplete at the interface between the ferroelectric and the ferromagnetic thin film. This leads to a modification of the magnetic exchange interaction in the FM film. Such effects have been observed in metallic ferromagnetic films, dilute magnetic semiconductors and magnetic oxides [13,21,22,131–134]. The control of magnetism by changing the charge carrier density in a ferromagnetic and ferroelectric oxide heterostructure was first observed in $La_{0.8}Sr_{0.2}MnO_3/Pb[Zr_{0.2}Ti_{0.8}]O_3$ (LSMO/PZT) heterostructures [125]. Figure 5.1 shows a magnetic hysteresis loop showing the modulation of the LSMO magnetization as the PZT polarization switches with an external electric field [125]. Another example of an electric field induced change in magnetic properties was observed in FePt thin films [132] where a liquid electrolyte was used to apply a high electric field at the surface of the magnetic film. On application of electric voltage, a 4.5% coercivity change was observed and attributed to a change in the number of unpaired d electrons.

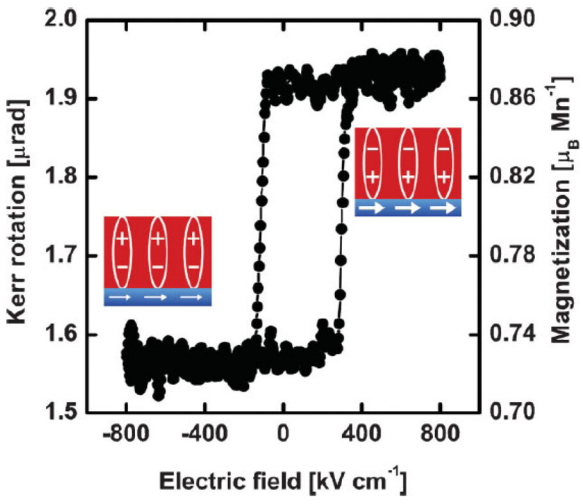

Figure 5.1: Magnetoelectric hysteresis curve at 100 K showing the magnetic response of the PZT/LSMO heterostructure as a function of the external electric field. The figure is adapted from [125].

A recent theoretical prediction argued that ME coupling in Fe/BTO heterostructures could originate via electronic hybridization between Ti and Fe atoms [21]. Atomic displacement at the interface caused by ferroelectric polarization changes the overlap between the atomic orbitals which consequently affects its magnetic properties at the interface. Such interfacial ME coupling lead to the electric field control of spin polarization of Fe (the difference between the density of states of the majority and minority spin carriers at Fermi level) at its interface with BTO [13] in a Fe/BTO/$La_{0.67}Sr_{0.33}MnO_3$ heterostructure where Fe and LSMO acted as the two electrodes and BTO as the ferroelectric tunnel barrier [13]. The authors observed that the spin polarization lead to a change in the tunnel magnetoresistance between the two magnetic layers. Similar results were obtained in Co/BTO/LSMO heterostructures [22]. In another study, the magnetism at the oxidized interface of Fe/BTO was controlled by changing the cation displacements in BTO on applying electric voltage [129]. Similar interface effects were predicted for Fe_3O_4/BTO and Co_2MnSi/BTO interfaces [135, 136].

Strain mediated ME coupling has been one of the most efficient mechanisms to observe large ME coupling effects at room temperature. Ferroelastic behavior of ferroelectric substrates can impose strain on the magnetic thin film deposited on top. Application of an electric field alters the strain state of the ferroelectric substrate which is transferred to the ferromagnetic thin film via inverse magnetostriction. The electrical and magnetic components are hence coupled via magnetoelastic interaction. Strain in the ferromagnetic film can change the magnetic properties such as magnetoelastic anisotropy, coercive field, and magnetic domains [137]. Piezoelectric materials exhibit a linear strain in response to external electric fields. Volatile piezo strain-induced magnetic changes have been observed in $La_{0.7}Sr_{0.3}MnO_3$ (LSMO)/$Pb(Mn_{1/3}Nb_{2/3})_{0.72}$-$Ti_{0.28}O_3$ (PMN-PT) heterostructures [127]. The magnetization of LSMO varies according to the characteristic 'butterfly-loop' in response to the electric field which merely traces the piezo-strain dependence on the electric field (see Figure 5.2).

The electric field applied across BTO in FeRh/BTO heterostructures was used to drive the FeRh film through AFM-FM phase transition close to room temperature [138, 139]. The effect was associated with strain transfer from the ferroelectric substrate to the ferromagnetic film changing the unit cell parameter of FeRh which controls the AFM/FM transition temperature of the system.

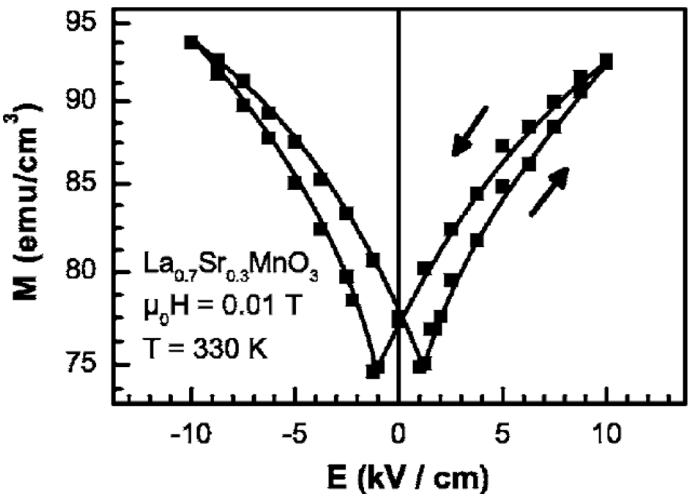

Figure 5.2: The in-plane magnetization (M) of a LSMO thin film grown on single crystal PMN-PT [001] with external electric field (E) applied across the PMN-PT substrate. The arrows show the direction of the electric field sequence. The figure is adapted from [127].

A non-volatile 90° switching of the magnetization direction associated to a ferroelastic change of magnetic anisotropy was observed in Ni/BTO heterostructures where the magnetic easy axis rotated from in-plane to out-of-plane of the sample [140]. The magnetic easy axis of the Co layer in a Co/PMN-PT heterostructure was reversibly rotated by 90° when the polarization of the PMN-PT was changed by applying electric fields of ±8 kV/cm [141]. In the same study, a reversible 180° rotation of the easy axis was observed under an electric field of ±5 kV/cm and a small field of 0.5 mT.
In a recent study, the local magnetic anisotropy was manipulated via ME coupling in a CoFe/BTO heterostructure where an electric field was used to change the strain state of the ferroelectric BTO substrate [8]. Figure 5.3(a) shows the commonly known a_1-a_2 ferroelastic domain pattern of the BTO which was magnetoelastically imprinted via partial strain transfer on the CoFe film during growth. The application of electric voltage induced changes in the local strain state of BTO domains (a_1-a_2 to a_1-c domain pattern) which via inverse magnetostriction changed the magnetic domain pattern of the CoFe film (see Figure 5.3(b). Strain mediated ME coupling was also used in another study to reversibly move the magnetic domain walls in an epitaxial Fe film grown on top of a BTO substrate [9].

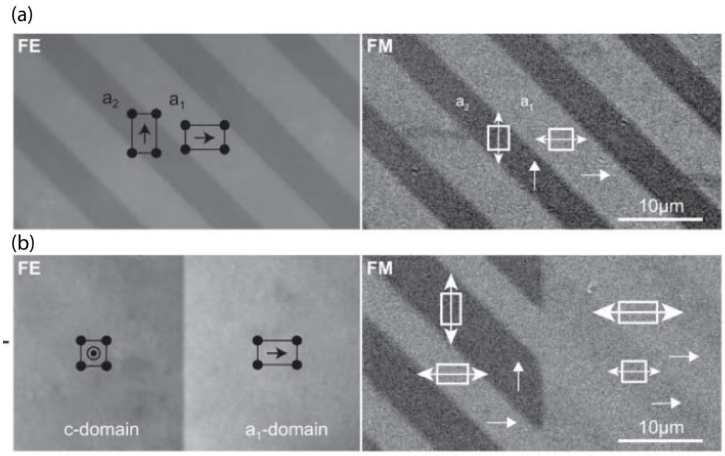

Figure 5.3: FE and FM domain structure of BTO and CoFe film (a) after growth and (b) after applying electric field. The images are recorded via Kerr microscopy. The figure is adapted from [8].

Changes of magnetic properties in response to electric field have been widely observed in bulk and thin film heterostructures. Electric field control of magnetic anisotropy has been recently extended to Ni nanoparticles on PMN-PT substrate [10]. It has been shown that the superparamagnetism in non-interacting Ni nanoparticles coupled to PMN-PT substrate can be manipulated by applying an external electric field [10]. The application of electric field modifies the strain state of the nanoparticles and consequently changes the magnetoelastic anisotropy. Since the blocking temperature T_b of a superparamagnetic system depend on the total magnetic anisotropy (see section 1.5), ferroelastic control of the T_b is feasible. Within this study, the authors show that the T_b of the Ni nanoparticles shifts by approximately 40 K under the application of an out-of-plane voltage to the ferroelectric substrate (see Figure 5.4) [10].

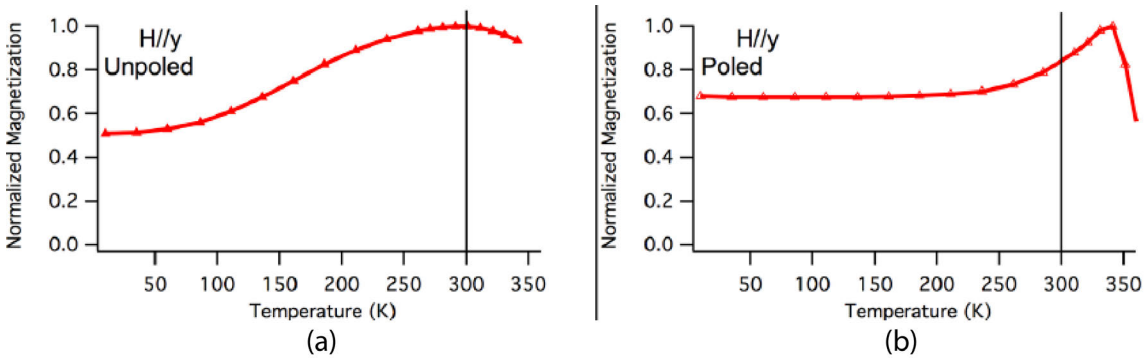

Figure 5.4: Zero field magnetization curves as a function of temperature measured in y direction in (a) unpoled and (b) poled PMN-PT crystal state, respectively. The figure is adapted from [10].

These results suggest that an electric field control of the critical temperature T_P separating superparamagnetic behavior from superspin-glass or superferromagnetic behavior, in the case of weakly or strongly interacting nanoparticles, is also possible. This is because similar to T_b, T_P also depends on the magnetic anisotropy which can be controlled by ferroelastical means [28, 29]. In order to explore such a possibility, a polycrystalline Fe wedge with variable thickness is grown on BTO to identify a thickness for which superparamagnetic behavior is present close to room temperature. With the help of XPEEM and XMCD, the electric field induced changes in the superparamagnetic properties are spatially resolved at low Fe thickness.

5.2 Sample growth and characterization

The Fe/BTO heterostructure was in-situ fabricated via electron-beam deposition. An Fe wedge was deposited on a single crystal $BaTiO_3$ (BTO) substrate [001]-oriented (0.5 mm single side polished from SurfaceNet GmbH) in a pressure of about 10^{-8} mbar. The deposition rate (1 Å/min) was calibrated via a quartz balance prior to the film deposition. The deposition was carried out at 300 K where the BTO crystal is within the tetragonal phase. A blade was used to cover approximately half of the sample during deposition of 2.5 nm of Fe. After that the blade was removed and further 0.5 nm of Fe were deposited uniformly over the substrate. Hence the film thickness varied from 0.5 nm at the thinner side of the wedge to 3 nm at the thicker side. Due to the distance between the blade and the sample, the thickness change beneath the blade is not abrupt and a wedge is grown where the thickness of the film varies smoothly within a small lateral distance of about 20 μm. A cross-section of the obtained film is schematically shown in Figure 5.5. After deposition, the sample was transferred to the XPEEM chamber for chemical and magnetic characterization without breaking the vacuum. The initial characterization after growth was followed by deposition of a 3 nm Al layer on top and remounting the sample holder to ensure electrical conductivity for the application of electric voltage. The XPEEM measurements after applying voltage were performed at 320 K.

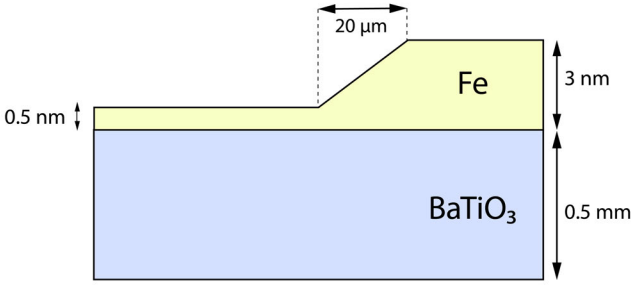

Figure 5.5: Schematic showing the cross-section of the Fe/BTO sample. The dimensions in the figure are not scaled.

Spatially resolved spectroscopic analysis of the as-grown Fe wedge/BTO was performed via XAS using XPEEM. The $L_{3,2}$ absorption edges of Fe and Ti were used to visualize the local element distribution on the sample. It was carried out by recording images with photon energies tuned to the resonant peak values (edge) and off the edge (pre-edge) for Fe and Ti. A normalized edge/pre-edge image displaying the local distribution of Fe on the sample is shown in Figure 5.6(a). A similar edge/pre-edge image in Figure 5.6 (b) shows the local distribution of Ti across the wedge. The measurement was carried out with linearly polarized X-rays so the magnetic contrast does not interfere with the recorded intensity. Line profiles showing the normalized intensity along the green and yellow dotted arrows marked in Figure 5.6(a) and (b) are shown in Figures 5.6(c) and (d), respectively. The wedge-shaped profile of the Fe is evident from Figure 5.6(c) where the thickness of the wedge (t_{Fe}) varies along the $[100]_{pc}$ direction of BTO from 0.5 nm to 3 nm. Elsewhere, the Fe thickness is constant, either 'thin' (0.5 nm) or 'thick' (3 nm). The opposite gradient of intensity of Ti across the wedge as compared to that of Fe is due to the Ti signal attenuation as the Fe thickness on top increases. Local spectroscopic information on the wedge can be obtained by selecting a region of interest. XAS spectra for Fe and Ti extracted at the thickest and the thinnest Fe regions (marked by 1 and 2 in Figure 5.6(a,b)) are shown in Figure 5.6(e) and (f), respectively. XAS spectra for Fe on the wedge (1) display the absorption resonances at 707.3 eV and 721 eV corresponding to L_3 and L_2 edges, respectively. XAS spectra for Ti on the wedge (1) recorded between 450-485 eV displays the characteristic four spectral feautes of Ti^{4+} [142].

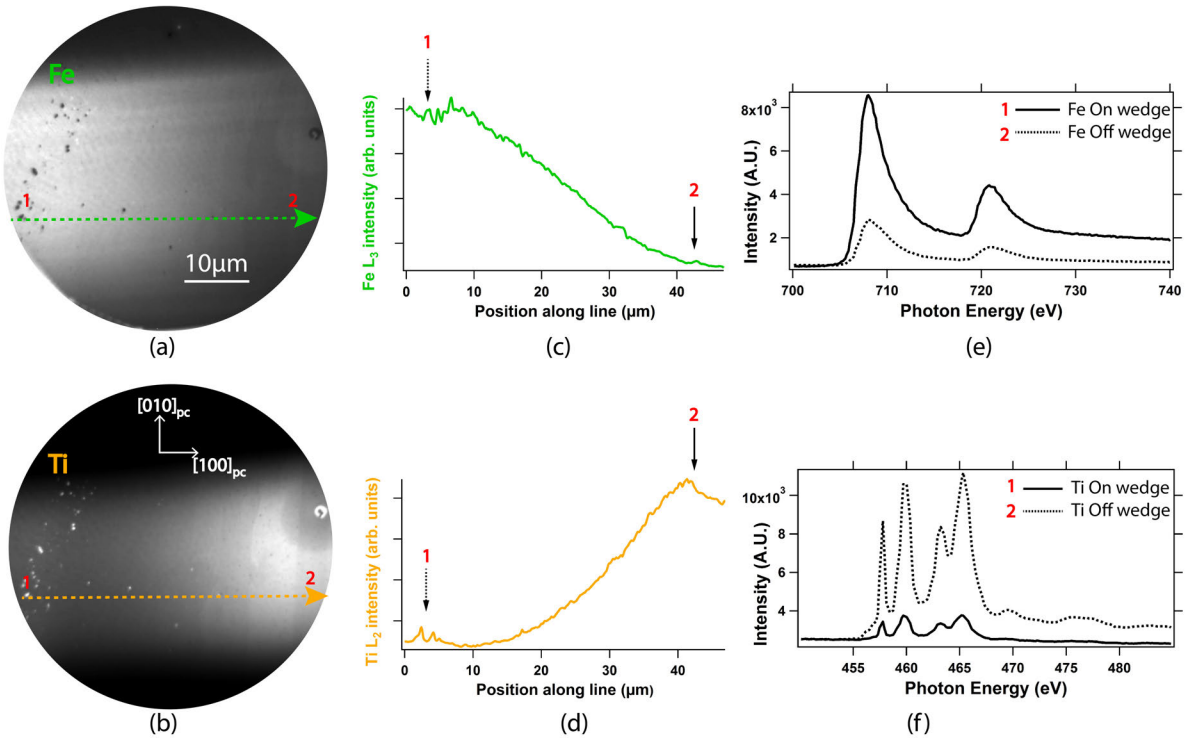

Figure 5.6: Normalized edge/pre-edge images showing local distribution of (a) Fe and (b) Ti on the wedge. Line profiles at the (c) Fe and (c) Ti edges along the green and yellow dotted lines marked in (a) and (b), respectively. XAS spectra of (e) Fe and (f) Ti at two different positions: 1 (On wedge) and 2 (Off wedge) marked in (a) and (b), respectively.

The shape and the intensity of the XAS spectra can provide important information about the local environment of the measured elements. No change of the Ti $L_{3,2}$ XAS spectral shape was observed across the Fe wedge region within the experimental resolution. In contrast, the Fe $L_{3,2}$ XAS curves do change as the Fe thickness varies (Figure 5.7(a)). The evolution is best resolved in the L_2-edge spectral region (Figure 5.7(b)) where changes in the oxidation state of Fe have larger impact in the spectral shape [60]. The thickest Fe regions ($t_{Fe} \sim 3$ nm) show a spectrum akin to that of bulk metallic Fe [60]. As the thickness of Fe is reduced, characteristic spectral features of FeO_x emerge and develop, being most prominent at the minimum Fe thickness of 0.5 nm. The increasing sensitivity to the Fe/BTO interfaces while reducing t_{Fe} highlights the presence of a FeO_x layer at the interface between the film and the BTO substrate in agreement with previous reports [129, 143].

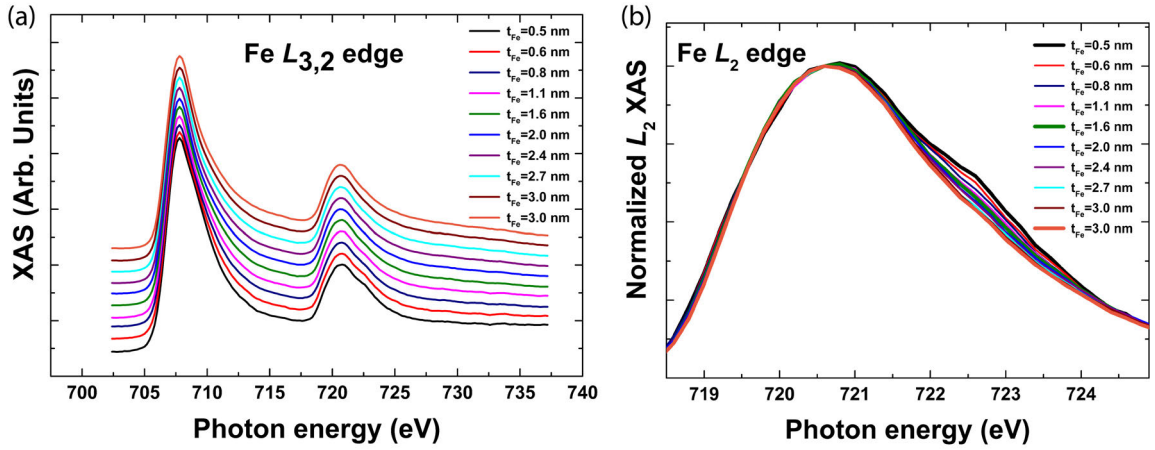

Figure 5.7: (a) XAS spectra of Fe for different thicknesses of Fe across the wedge. (b) Normalized Fe L_2-edge XAS intensity showing the oxidized nature of the interface at low Fe thickness.

The magnetic characterization of the as-grown sample was carried out via PEEM with XMCD as magnetic contrast mechanism. Figure 5.8(a) shows an XMCD image (of the same area as in Figure 5.6(a,b)) recorded at Fe L_3-edge (707.3 eV) showing a relatively sharp transition between regions showing zero XMCD contrast (white) and those with non-zero XMCD (blue/red). Figure 5.8(b) shows a plot where the line profile of XMCD intensity across the wedge is compared with the thickness profile of Fe along the line shown in Figure 5.8(a) (same line as that in Figure 5.6(a,b)). The critical thickness of the Fe film (t_{Fe}^{FM}) where the transition from magnetic to non-magnetic regime takes place is 1.3 nm.

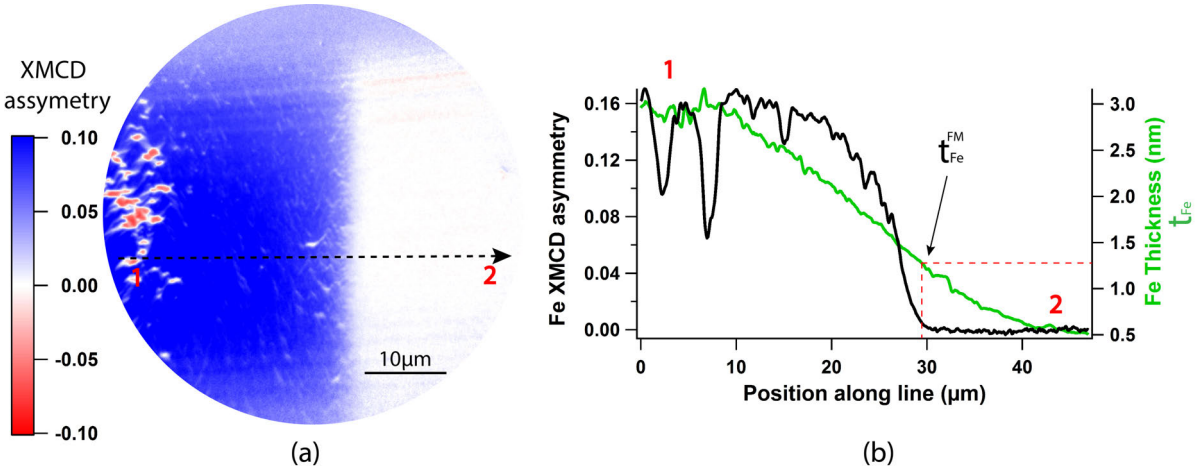

Figure 5.8: (a) XMCD image of the same area as in Figure 5.6(a,b) obtained at the Fe L_3-edge. (b) Fe thickness and XMCD line profiles along the line marked in (a).

To investigate the structure of the film, scanning transmission electron microscopy

(STEM) measurements were performed (in Laboratoire SPMS, CentraleSupélec, Université Paris Saclay, France) after electric field measurements in PEEM. A STEM high-angle annular dark field (HAADF) image (Figure 5.9(a)), obtained on a section within the region of maximum Fe thickness ($t \sim 3$ nm) shows a continuous and relatively smooth Fe layer separated from the BTO substrate by an approximately 2 nm thick interlayer. Superimposing element maps generated by energy dispersive X-ray (EDX) spectroscopy onto the HAADF image reveals that while the Fe layer is relatively pure, the interlayer contains substantial amounts of Al, Fe and O, and traces of Ba and Ti [Figure 5.9(b)]. A fourier transform image (inset of Figure 5.9(a)) of the Fe region shows that Fe is polycrystalline and exhibits crystal planes whose spacing of 2.03 Å corresponds well to the [011]-planes of the bcc structure of pure Fe.

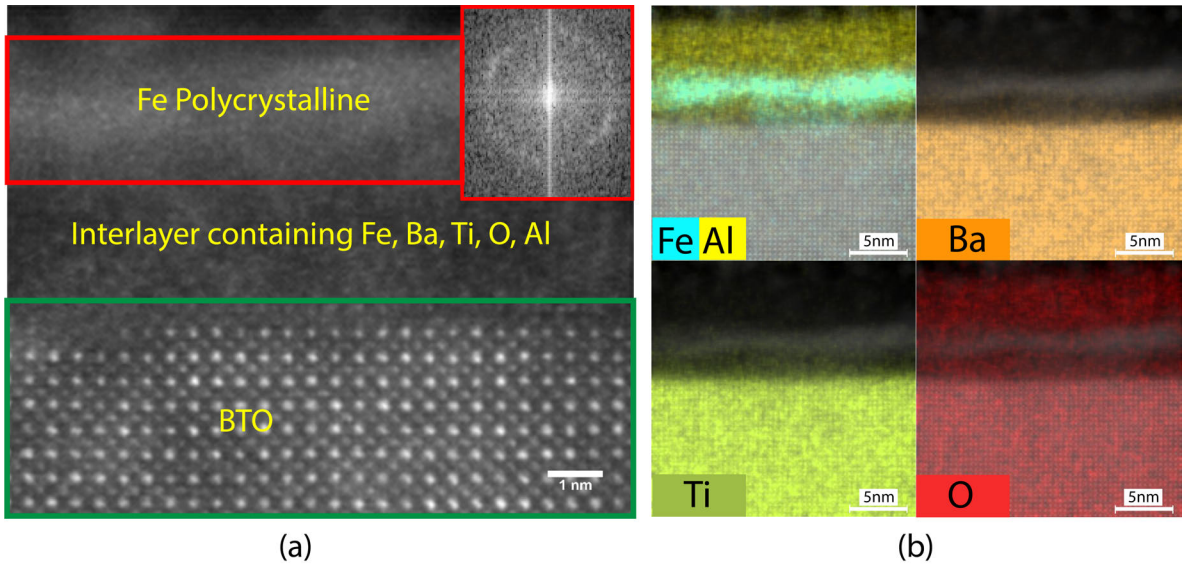

Figure 5.9: (a) HAADF-STEM image of the hetero-structure. From top to bottom: Al capping layer, metallic Fe layer, Fe/BTO interfacial layer, BTO substrate. Inset: fast fourier transform of the region of the Fe layer marked by a red rectangle. (b) EDX maps of selected elements (Fe, Al, Ba, Ti, O), superimposed on the HAADF image of panel (a).

The interlayer is likely to be due to sample damaging during the preparation of the cross-section for STEM measurements [144]. This has been confirmed by STEM measurements of similar samples. The polycrystalline nature of the film is intrinsic to the sample. The focused ion beam (FIB) preparation of the cross-section cannot induce the polycrystalline nature in the Fe film. On the contrary, it might induce alignment of the crystal along the FIB direction [144].
Figure 5.10(a) and (b) shows a magnified region of the Fe/BTO cross-section displaying the EDX map of Fe superimposed on HAADF image and the corresponding

HAADF-STEM image, respectively. The grain size is of the order of $3-4$ nm at thicker cross-section as shown by the grains marked in Figure 5.10(b). With the decreasing film thickness, the grain size is expected to decrease. If the grains are non-interacting, a superparamagnetic behavior would be expected as the critical thickness for Fe nanoparticles to become superparamagnetic is about 9 nm [145, 146].

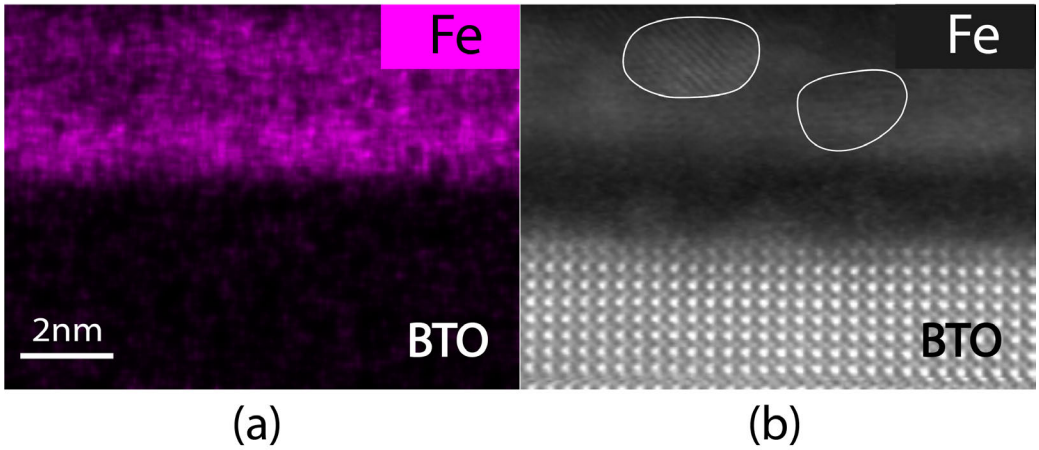

Figure 5.10: (a) High resolution EDX image of Fe. (b) HAADF-STEM image of the same region as in (a) highlighting two grains with white boundary.

5.3 Electric field control of magnetic domain pattern of Fe

The magnetic domain configuration of the as-deposited Fe wedge in Figure 5.8(a) displays no visible imprint from the underlying ferroelectric BTO domain structure. This suggests a low strain transfer (below 10%) from BTO to Fe during growth because of the low deposition rate (0.1 Å/min), in agreement with Streubel *et al.* [147]. The strain transfer from BTO to a magnetic film is known to be more efficient during thermal cycling as compared to that during growth [148]. Hence, the sample was cooled down to 60 K and heated back to 320 K to induce strain transfer. Figure 5.11(a) shows the initial magnetic state of the sample after thermal cycle prior to electric poling at a different sample position than that in Figure 5.8(a). It is evident from Figure 5.11(a) that the phase transitions of BTO altered the FE domain state of BTO which imprints on the Fe film via inverse magnetostriction. A striped white-blue domain pattern with domain walls oriented along $[\bar{1}10]_{pc}$ is now visible within the magnetic (thick) side of the wedge.

On application of electric voltage V=+74 V, the imprinted striped pattern on Fe became clearly defined as shown in Figure 5.11(b). However, after holding the voltage for some time, new domains with all-blue and all-white XMCD contrast and domain walls along $[100]_{pc}$ were observed in Figure 5.11(c). Increasing the voltage to +170 V leads to three kinds of magnetic domain patterns with domain walls oriented along $[100]_{pc}$ (Figure 5.11(d)). The FM domains observed in Figure 5.11(d) are labeled as α, β and γ according to their magnetic contrast and domain walls. The magnetic regions with domain walls along $[100]_{pc}$ and homogeneous XMCD contrast in Figure 5.11(d) have been labeled α and β depending on whether the magnetic contrast is white (XMCD ~ 0) or blue (XMCD > 0), respectively. Regions for which the former magnetic imprint has not changed (alternating white-blue striped domains with domain wall along $[\bar{1}10]_{pc}$) at V = +170 V, have been labeled as γ. On increasing the voltage from +74 V to +170 V, these α, β, γ regions of Fe move and occasionally interchange. This suggests that the magnetization of the Fe film is dominated by the magnetoelastic anisotropy which changes its magnetic easy axis according to the applied voltage. The fact that the γ pattern needs some time to be modified at +74 V to α, β is likely to be related to the presence of defects leading to a pinning of the domain walls [42].

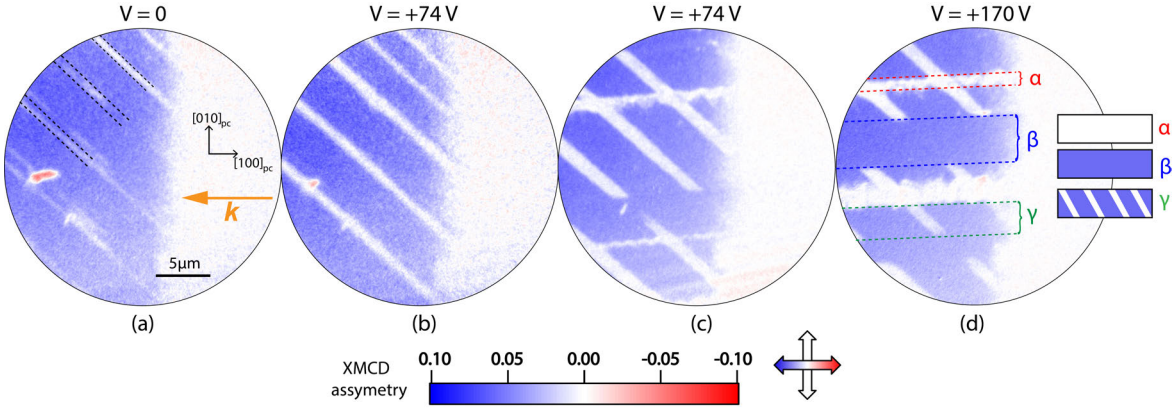

Figure 5.11: XMCD images of the Fe wedge at (a) 0 V (b,c) +74 V (d) +170 V out-of-plane electric voltage.

The white contrast (XMCD ~ 0) in α and some of the γ regions lack the magnetic sensitivity because of the orthogonal magnetization to the incoming beam direction ($\boldsymbol{M} \perp \boldsymbol{k}$). Hence, the magnetization direction is resolved by azimuthally rotating the sample. Figure 5.12 shows the XMCD images obtained as a function of azimuthal angle φ at +170 V. The region with lower t_{Fe} displays white (XMCD ~ 0) contrast independent of φ confirming the absence of long-range ferromagnetism. Within the α region, as φ is increased from 0° to 90°, the zero (white) XMCD contrast (Figure 5.12(a)) changes to alternating positive (blue) XMCD and negative (red) XMCD

(Figure 5.12(b)), highlighting that the magnetization $\boldsymbol{M}$ of the α regions alternates along $[010]_{pc}$ and $[0\bar{1}0]_{pc}$ as shown by the black arrows in Figure 5.12(b). Within the γ regions, the zero (white) XMCD changed to positive (blue) as φ is increased from 0° to 90°, while the positive (blue) XMCD changed to almost zero (reddish white) implying that the magnetization in the striped pattern of the γ region is along $[100]_{pc}$ and $[010]_{pc}$ within the blue and white stripes, respectively. Within the β regions, the positive (blue) XMCD changed to almost zero (white) as φ is increased from 0° to 90° indicating that the magnetization within these regions is oriented along $[100]_{pc}$. As all the magnetic components are along $[100]_{pc}$ or $[010]_{pc}$, an azimuthal rotation of 45° ($\boldsymbol{k} \parallel [110]_{pc}$) allows to observe the magnetic contrast for all the magnetic regions as magnetization along $[100]_{pc}$ or $[010]_{pc}$ have a non-zero projection along $[110]_{pc}$.

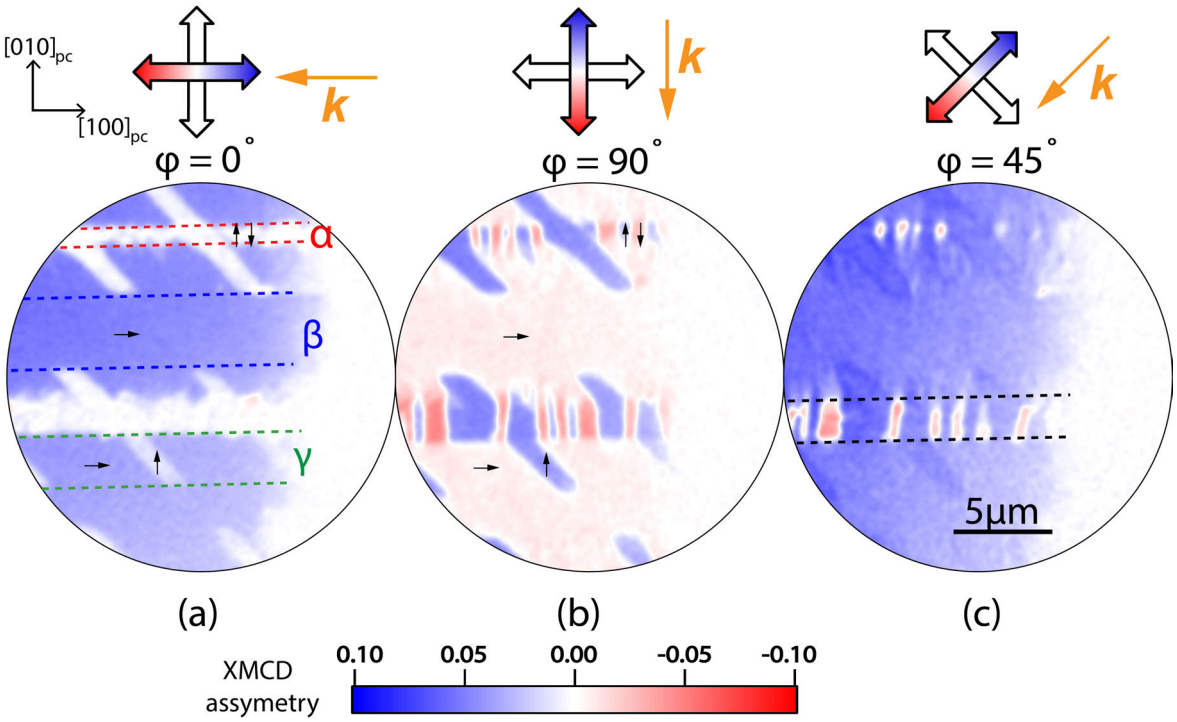

Figure 5.12: XMCD images of the Fe wedge at +170 V at different azimuthal rotation angles (a) 0° (b) 90° (c) 45°.

The azimuthal dependent XMCD analysis allows to conclude that the magnetization direction within the domains at zero voltage in Figure 5.11(a) points alternately along $[010]_{pc}$ (white stripes) and $[100]_{pc}$ directions (blue regions). This domain orientation after the thermal cycle (th) is an indirect manifestation of an underlying ferroelastic a_1^{th}-a_2^{th} [8, 45, 149] or purely c^{th} [8, 149] texture resulting from the inverse magnetostriction effect, governed by the magnetoelastic coupling [150]. The application of V = +74 V leads to a clearly defined domain pattern (Figure 5.11(b)) and finally to a new domain

pattern with domain walls along $[100]_{pc}$ (Figure 5.11(c)). As the new FM domain walls along $[100]_{pc}$ resemble FE a_1-c walls (see section 1.7.1.1), the presence of pure c^{th} FE domain after thermal excursion can be excluded. Hence, it is concluded that the BTO FE domain pattern after thermal excursion was a_1^{th}-a_2^{th} which transformed to a_1^V-c^V pattern after applying voltage. Despite the thickness gradient of Fe, no noticeable dependence of the new magnetic domain pattern on the Fe thickness is seen along $[100]_{pc}$.

5.4 Extension of the long-range ferromagnetic order towards lower Fe thickness

A local extension of the long-range FM behavior towards lower t_{Fe} is observed for β regions only. This is clearly seen in Figure 5.13(a) at V=+150 V where the red line marks the original position of the onset of long-range FM for the wedge at V = 0 V. The increase in the XMCD signal only over the β region is visualized in Figure 5.13(b).

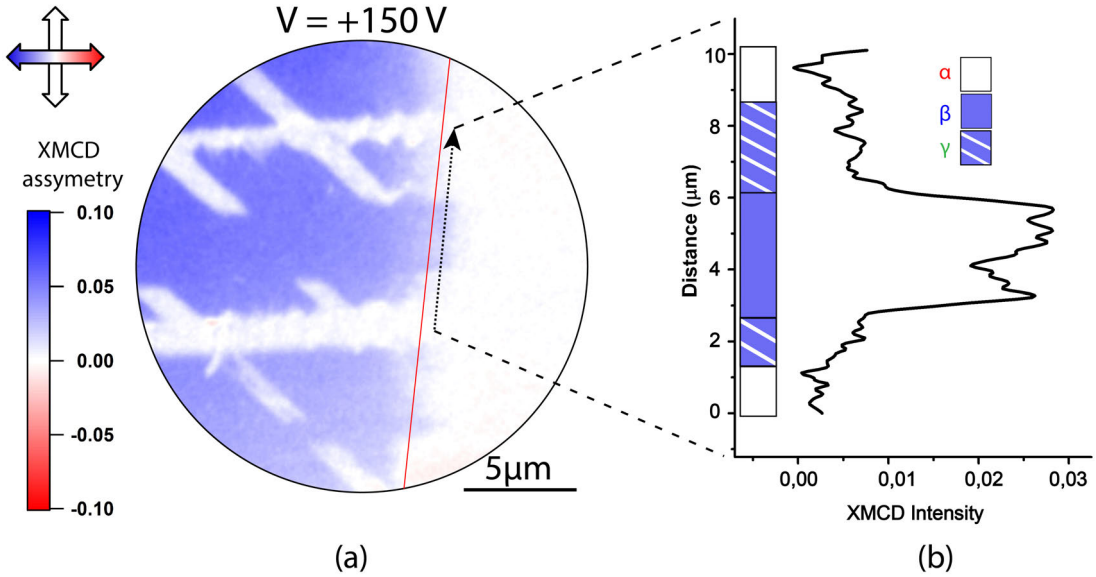

Figure 5.13: (a) XMCD image at V= +150 V highlighting the extension of the long-range FM behavior to low t_{Fe} across the marked black arrow. (b) A line plot across the dashed line shown in (a). The line plot is correlated with the α, β and γ regions schematically.

No information can be obtained about the extension of long-range FM at α regions since at azimuthal angle $\varphi = 0°$, there is no sensitivity to the magnetization direction ($\boldsymbol{M} \perp \boldsymbol{k}$) for α. Therefore, the azimuthal angle of the sample was rotated from to 0° in Figure 5.14(a) to 45° in Figure 5.14(b,c) to have access to magnetization of α regions.

No extension was observed at α regions (Figure 5.14(b,c). The extension of the FM for β regions only towards lower t_{Fe} was reproduced when the voltage was further cycled from +170 V (Figure 5.14(b)) to −170 V (Figure 5.14(c) and Figure A.1(c)). The position of the extended regions is highlighted by the black arrows in Figure 5.14(c). The appearance of extended FM regions on application of electric voltage at the β regions is visualized in Figure 5.15(a). It shows a 2-D plot of XMCD profile (along horizontal axis) across a red dashed line marked in Figure 5.14(c) as a function of electric voltage (along vertical axis). At a fixed electric voltage (given by the vertical axis), the horizontal axis corresponds to the XMCD intensity variations across the line. It is clearly observed that the blue magnetic region extends towards the right direction on increasing the voltage from 0 V to −170 V. Figure 5.15(b) compares the XMCD profile across the dashed red line in Figure 5.14(c) at 0 V and −170 V. The long-range FM behavior extends to about 1.3 μm towards $[100]_{pc}$. Considering that the Fe thickness changes by 2.5 nm in about 25 μm (Figure 5.8(b)), the increase of FM by 1.3 μm corresponds to a decrease in the critical thickness for FM (t_{Fe}^{FM}) of about Å.

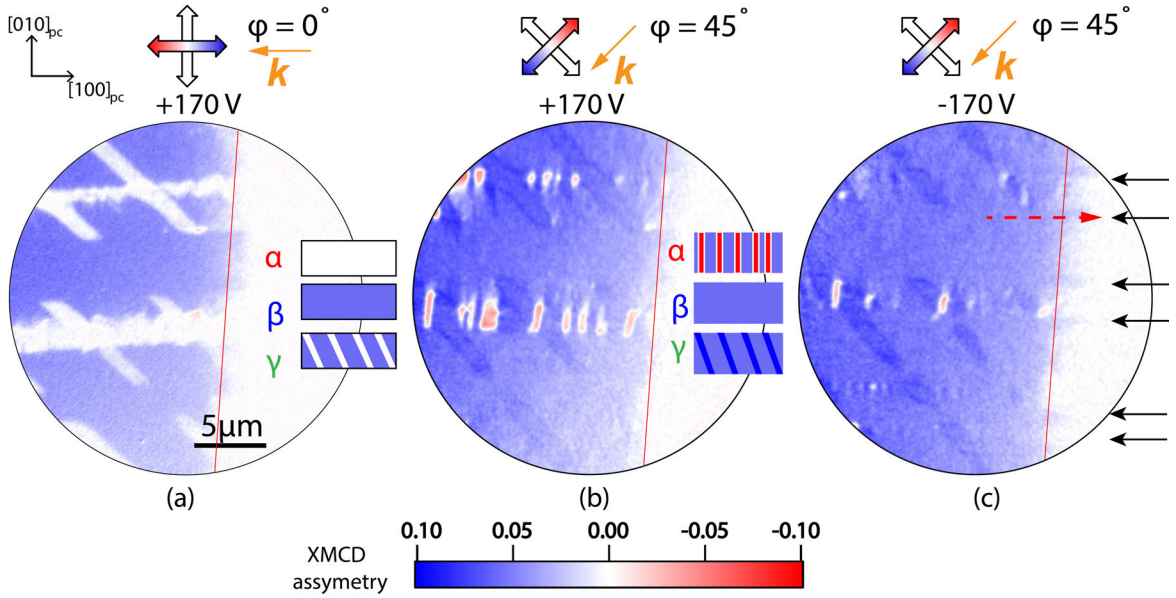

Figure 5.14: XMCD images of the Fe wedge at +170 V at azimuthal angles of (a) 0° and (b) 45°. (c) XMCD image at −170 V of the same region as in (b). The black arrows in (c) highlight the position of the extended FM regions.

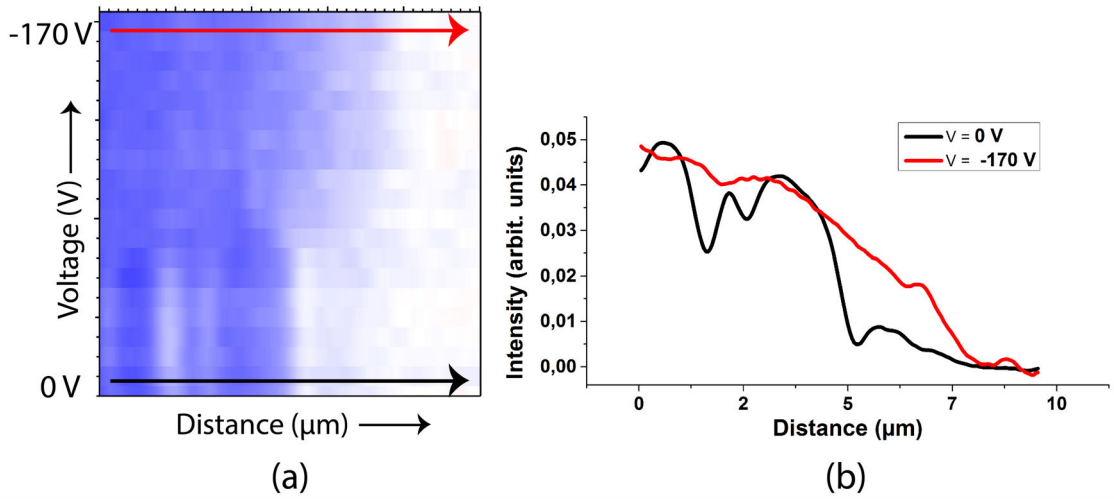

Figure 5.15: (a) 2-D plot showing the XMCD intensity profile across the red dashed line marked in Figure 5.14(c) as a function of different V (vertical axis). (b) Line profiles at V=0 V and V=−170 V showing the extension of the XMCD as the voltage is increased from 0 V to −170 V.

To understand the physical phenomenon behind the electric field induced extension of long-range FM towards lower t_{Fe} observed only at β regions, it is necessary to investigate the history and the evolution of the strain state of β regions and possible correlation with the FE strain state of the BTO substrate. Given the initial BTO FE domain state after growth of the Fe film and the magnetostrictive nature of the Fe film (see Appendix section A.1), a differential strain (DS) model (see Appendix section A.2) can explain the rotation of the local magnetization as a function of electric voltage in terms of changes in the magnetoelastic anisotropy. Thus, the strain history of β regions and its evolution with electric voltage can be mapped. From the FM domain evolution in response to a voltage cycle from +170 V to −170 V, the sign of magnetostriction is inferred to be positive (see Appendix section A.1).

During growth, BTO can exist either in the a_1-a_2, a_1-c or a_2-c state (see section 1.7.1.1). The experimentally observed coexistence of α, β, and γ regions on Fe can only be explained by the presence of the a_1^{gr}-c^{gr} FE BTO domain pattern under the Fe film at growth (gr) time. The deduction is discussed in Appendix section A.2 for the sake of simplicity. Therefore, the initial a_1^{gr}-c^{gr} BTO pattern after growth transforms to a_1^{th}-a_2^{th} post thermal cycle (th) (Figure 5.11(a)) and a_1^{V}-c^{V} post electric poling (V) (Figure 5.11(d)). From the DS model, the strain history of β regions (beginning from growth to post thermal cycle to post electric poling) and the corresponding underlying FE domain state can be deduced. The β region can originate from the following different paths:

(1) **FE:** $a_1^{gr} \rightarrow a_1^{th}$-$a_2^{th} \rightarrow c^V$
FM: no-imprint $\rightarrow \quad \gamma \quad \rightarrow \beta$

(2) **FE:** $a_1^{gr} \rightarrow a_1^{th}$-$a_2^{th} \rightarrow a_1^V \rightarrow c^V$
FM: no-imprint $\rightarrow \quad \gamma \quad \rightarrow \alpha \rightarrow \beta$

This implies that the β regions develop in regions with an underlying c^V FE domain which were a_1^{gr} FE domains at growth time. Such $a_1^{gr} \rightarrow c^V$ transitions induce a uniaxial compressive strain of about 1% along $[010]_{pc}$ (also discussed in section 1.7.1) which is completely transferred to the Fe film. In contrast, Fe corresponding to α and γ regions originate from c^{gr} domains at growth time and do not experience any strain at high voltage as compared to that at growth time (see Appendix Figure A.2).

5.5 Discussion

Our results show that the onset of a long-range FM order extends towards the lower Fe thickness at localized sample position after applying an external electric voltage. The analysis of XMCD contrast with the voltage has allowed to empirically determine the sign of the magnetostriction constant (Appendix section A.1) and deduce the associated FE domain history of BTO. With the help of the differential-strain analysis (Appendix section A.2) which takes into account the local strain transfer from BTO to Fe film, the voltage induced magnetoelastic modulation of FM in Fe can be explained. Our analysis highlights a direct correlation between the long-range FM regions and their local strain history. Electric field induced extension of long-range FM order takes place only for the regions which experience a local uniaxial compression of 1.1% along $[010]_{pc}$ as compared to the unstrained state at the growth time.
Such a strain-induced decrease in the critical thickness resulting from an application of voltage could be interpreted as a ferroelastic modulation of T_c. In this case, the non-magnetic region (at 320 K) in the vicinity of $t_{Fe}^{FM} = 1.3$ nm would become ferromagnetic on application of a compressive strain. In order to explore this possibility, additional temperature-dependent XMCD measurements were performed on a similar Fe wedge deposited on BTO. The results described in Appendix section A.3 provide evidence that a change of T_c of about 50 K would be necessary to produce the observed change in the critical thickness (Δt_{Fe}^{FM}) by 1$\mathring{A}$. Although voltage induced changes of T_c of similar order have been observed in other materials [138], bcc Fe does not show such

behavior. Both theoretical and experimental results highlight that T_c for bcc Fe barely changes under pressure [151–154]. Therefore, in our case, an electric field induced change of T_c due to 1.1% uniaxial compression cannot explain the observed extension of FM regions to lower t_{Fe}.

At this point, we recall the nano-polycrystalline nature of the Fe film, as well as the fact that, surprisingly, the long-range FM ordering for the as-grown film is absent close to room temperature for Fe thicknesses below 1.3 nm. This suggests that at low Fe thickness, the film is composed of nanocrystals behaving as superparamagnetic nanoparticles with blocking temperature T_b below that of the experiment (320 K). While the onset of FM close to room temperature for ultra-thin and highly-ordered coherent epitaxial films is approximately one atomic monolayer [155,156], superparamagnetic behavior of nanoparticles has been previously reported for Fe films above this thickness resulting from Volmer-Weber type island growth [157,158]. At low coverages, such type of growth leads to a random nucleation and expansion of unconnected Fe nano-islands which become superparamagnetic due to their size. In this context, Kim *et al.* recently reported that the blocking temperature T_b of non-interacting superparamagnetic Ni nanoparticles deposited on BTO can be increased by 40 K due to an electric field induced compression [10]. This result was associated with the electric field induced change of magnetoelastic anisotropy leading to an increase of the energy barrier between energetically equivalent magnetization directions. This prevented the time-dependent flip of the 'super-spin' of the nanoparticles and fixed its magnetization along a certain direction.

An electric modification of T_b as reported by Kim *et al.* cannot explain our results. Within this scenario, an increase of T_b implies 'blocking' of spins of nanoparticles along a given direction defined by the magnetic anisotropy. These are the two energetically equivalent possibilities with anti-parallel magnetizations. If such a 'blocked' state was imaged by XPEEM, the XMCD signal of an assembly of 'blocked' nanoparticles would average to zero as the spatial resolution of PEEM (30 nm) is much larger than the grain size (< 3 nm). In contrast, we observe that the long-range FM order appears on applying voltage, suggesting an interaction between the nanoparticles. Such observation is typical for nanoparticle systems with non-zero inter-particle interactions which undergo a superparamagnetic-superferromagnetic transition at a transition temperature T_P. For $T > T_P$ the system is superparamagnetic. For $T < T_P$, the inter-grain interactions are strong enough to dominate the thermal energy aligning the super-spins of nanoparticles along a given direction defined by the anisotropy and form a so-called superferromagnetic state [31,32,159–165]. Similar to T_b, T_P is also dependent on the local

anisotropy of the nanoparticles. An electric field induced modification of magnetoelastic anisotropy can drive the transition from superparamagnetic to superferromagnetic state [32].

Therefore, we conclude that the observed increase of critical thickness for long-range FM only at β regions is due to electric field induced modification of magnetoelastic anisotropy that leads to a local superparamagnetic-superferromagnetic transition. The ferroelastic modulation of magnetic anisotropy leads to an increase of T_P of about 50 K above 320 K. This novel observation of electric field induced local superparamagnetic to superferromagnetic transition near room temperature in a nanoscale magnetic material opens exciting possibilities for an electric field control of magnetism and exploitation of the ME coupling for new storage devices.

Chapter 6

Summary

Controlling magnetism without applying magnetic fields is an important topic of research owing to its foreseen applications in spintronics and magnetic data storage with low-power consumption. Several approaches are currently being investigated. Within this thesis, two major routes are explored namely, optical control of magnetism via femtosecond laser pulses and electric field control of magnetism.

The first part of the thesis deals with investigating all-optical helicity dependent switching (AO-HDS) in a ferrimagnetic TbFe alloy. Here, the magnetization can be switched deterministically using the helicity of a circularly polarized femtosecond laser beam impinging the sample. The recent experimental work showed that AO-HDS is a general phenomenon which is not limited to rare-earth-transition metal ferrimagnetic alloys and is also observed in ferromagnetic materials. However, the fundamental mechanism of the switching mechanism is not clear and is currently under debate. In this thesis, the scalability of AO-HDS is investigated by a small laser spot size of few microns. The questions such as the role of heating and the microscopic mechanism behind AO-HDS are investigated in TbFe alloy by photoemission electron microscopy (PEEM) employing X-ray magnetic circular dichroism (XMCD) as the magnetic contrast mechanism. The experiments reported within this thesis have been carried out in a continuous pulse train mode of the laser to minimize the relaxation effects which appear in experiments when the magnetic domain state is imaged after the laser is switched off.

The space-resolved experiments show that the central region within the laser spot size gets thermally demagnetized. The AO-HDS is observed to be a local effect within the laser spot size that occurs in a ring region surrounding the inner thermally demagnetized region. The magnetic domains within this ring region switch stochastically via thermally activated domain wall motion. A thermal gradient established in the ring region assists the switching process which can be influenced by the repetition rate of

the laser and the base temperature of the sample. Therefore, the local heat accumulation, thermal gradient, and heat conductivity across the sample influence the switching process.

A novel thickness dependent behavior of the switching orientation by a particular laser helicity has been reported. The results show that the magnetization orientation resulting from the interaction between the TbFe alloy and the laser, not only depend on the laser helicity but also on the film thickness. Therefore, above a threshold thickness between 10 nm and 20 nm, the switching orientation inverts for the same laser helicity. This effect does not depend on the alloy composition or any other magnetic parameter. Although this thickness dependence indicates a presence of two competing microscopic mechanisms contributing to AO-HDS, the laser helicity flipping experiments indicated that the magnetic circular dichroism (MCD) by the laser is able to explain the observed switching in thicker films. The results show that helicity dependent information is transmitted through a narrow ring at the periphery of the inner demagnetized region where one of the magnetic orientation preferentially absorbs more energy.

All-optical helicity dependent switching via a femtosecond laser without applying magnetic field offers a clear path for controlled 180° magnetization reversal with low power consumption in magnetic devices. The thesis contributes towards increasing the basic understanding of magnetization switching in AO-HDS by imaging the magnetic contrast with high resolution while the laser interacts with the sample. The results on the importance of attained T_c and the magnetic circular dichroism as a microscopic mechanism provide a clearer picture about the fundamentals of AO-HDS, which would help towards the realization of this phenomenon in practical applications.

The second part of the thesis addresses the electric field control of superparamagnetism in an artificial multiferroic heterostructure. Control of magnetic properties by means of electric fields has been an emergent field of research within the last years. Electric field control of magnetic anisotropy, magnetic ordering, and magnetic transition temperatures have recently been reported in thin film heterostructure. At the nanoscale, the blocking temperature of a superparamagnetic system of nanoparticles has been manipulated by ferroelastic means via a magnetoelastic modification of the magnetic anisotropy. To this respect, it is possible to control the transition temperature separating the superparamagnetic-superferromagnetic regimes as it also depends on the magnetic anisotropy. To explore this possibility, a polycrystalline Fe film is grown by means of electron beam evaporation onto a ferroelectric and ferroelastic (FE) BaTiO3 (BTO) substrate. The Fe film is deposited in a wedge-shape with its thickness varying between $0.5 - 3$ nm within a lateral distance of approximately 20 μm. The magnetic

domain state and its evolution with temperature and voltage applied to the FE substrate are spatially resolved by means of PEEM and XMCD as the magnetic contrast mechanism. A wedge sample allows identification of the threshold thickness below which the film is superparamagnetic close to room temperature. The critical thickness for long-range ferromagnetic ordering is observed to be around 1.3 nm.

It is known that the magnetic domain configuration of the FM film relies on the strain imposed by the underlying FE BTO substrate via inverse magnetostriction. Any local modification of the strain state of BTO, induced either by a temperature cycling or a voltage application, has a direct impact on the magnetic ordering of the FM film as the magnetoelastic contribution to the total magnetic anisotropy is affected. The XMCD vs voltage data shows local rotations of the magnetization by $\pm$ 90° associated to ferroelastic induced changes of the magnetic anisotropy for Fe thickness above 1.3 nm. These results highlight that the magnetization orientation in the polycrystalline film is dominated by the magnetoelastic anisotropy.

For Fe thickness below 1.3 nm, the application of large out-of-plane voltages to the FE BTO substrate leads to a spontaneous formation of long-range FM ordering at some particular sample positions (in the vicinity of the threshold thickness below 1.3 nm where FM ordering was previously absent. A differential strain analysis of the XMCD vs voltage data allows tracking of the strain history of these regions. The analysis shows that the Fe in these regions experiences a local uniaxial compression of about 1.1% as compared to an almost unstrained state at the growth time. The absence of FM ordering in these regions, prior to the voltage application, suggests that at low Fe coverages the film consists of islands which behave superparamagnetically close to room temperature, similar to as observed for example for Fe deposited on MgO. In addition, the spontaneous formation of long-range FM ordering within these regions points to strong inter-particle interactions. The local ferroelastic compression on these areas locally enhances the magnetoelastic anisotropy. This increases the energy barrier for magnetization flip of the superparamagnetic particles allowing the nanoparticles to fix their magnetization along the electric field-induced magnetoelastic anisotropy. The strong inter-particle interactions allow a collinear alignment of the magnetization for all the nanoparticle, resulting in a superferromagnetic state. Effectively, the electric field induces a superparamagnetic to superferromagnetic transition by increasing the transition temperature by about 50 K.

The electric field induced strain has been widely used to alter the magnetic properties of multiferroic composite materials. However, controlling the magnetism of nanoscale particles can also play a role in the technological functionality. Today, the superparamagnetic limit is an issue for the data storage industry because the magnetization in the

nanometer-sized grains oscillates due to the thermal energy. However, superparamagnetic limit of the nanoparticles can be turned into an advantage if the magnetization direction can be switched by electric field induced changes of the magnetic anisotropy. Such a prospect represents a rather unexplored dimension in magnetoelectric coupling and has a potential for novel magnetization switching behavior on a nanoscale close to room temperature.

In summary, the thesis investigated two major paths for magnetization control without applying any external magnetic fields. The results increase the understanding towards the physical mechanism behind AO-HDS and show novel magnetoelectric phenomena at nanoscale which might pave the way for the implementation of these effects in novel spintronic and/or magnetic devices.

Appendix A

A.1 Sign of magnetostriction

The easy axis of a positive magnetostrictive material aligns perpendicular/parallel to the direction of compressive/tensile stress as shown schematically in Figure A.1(a). Similarly, the easy axis of a negative magnetostrictive material aligns parallel/perpendicular to the direction of compressive/tensile stress as shown in Figure A.1(b).

In order to identify the sign of magnetostriction, the behavior of α, β, and γ was recorded during a voltage cycle from +170 V to −170 V. Figure A.1(a-c) shows XMCD images recorded at electric voltage +170 V, 0 V, and −170 V at an azimuthal angle of 45° where all in-plane components of magnetization are accessible. The XMCD image at +170 V in Figure A.1(a) shows three types of regions: α with alternating red and blue stripes and magnetization along $[010]_{pc}$ and $[0\bar{1}0]_{pc}$, β with homogeneous blue contrast and magnetization along $[100]_{pc}$ and γ with striped pattern resembling the original a_1°-a_2° and magnetization alternating along $[100]_{pc}$ and $[010]_{pc}$. By decreasing the voltage to 0 V, the relative fraction of α regions within the field of view increases. It decreases again as the voltage is cycled to −170 V (Figure A.1(b,c)). Such voltage dependence is typical for a_1 domains suggesting that the FE domains underlying α regions are a_1 domains. Therefore, the white and the blue stripes observed in Figure 5.11(b) are correlated with underlying a_1 and a_2 FE domains, respectively.

The direction of the magnetization in α regions (a_1 FE domains underneath) is along $[010]_{pc}$ with FM domain wall along $[100]_{pc}$ coinciding with the FE domain wall. It is well known that the long axis of the FE a_1 domain is oriented perpendicular to the a_1-c domain wall boundary [45]. Therefore, the long axis of the a_1 domain is along $[010]_{pc}$ which is parallel to the magnetization direction of α regions. Since the magnetization in the α region is parallel to the uniaxial stress axis of underlying a_1 domains, Fe exhibits a positive magnetostriction.

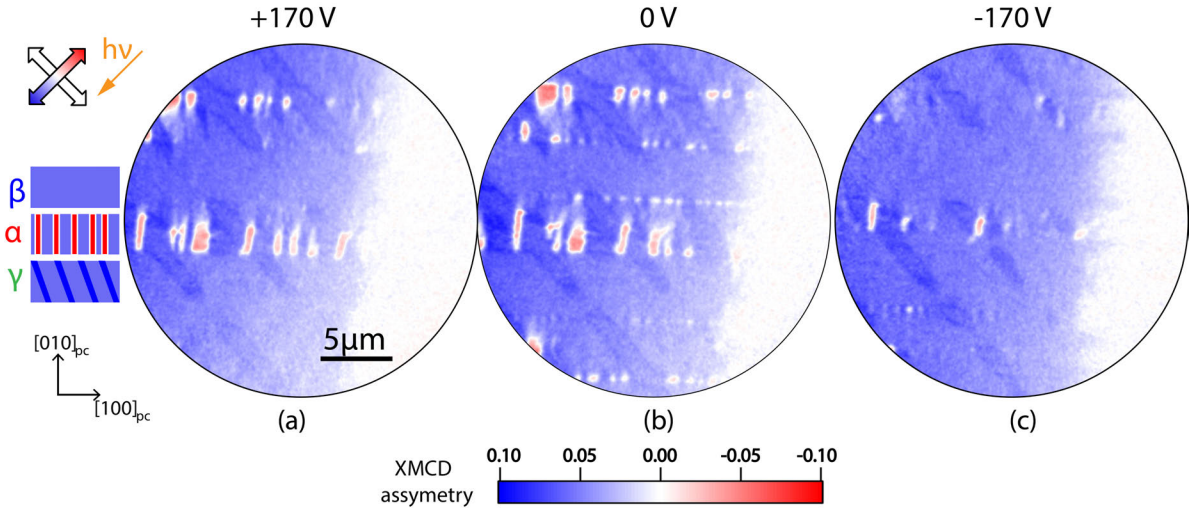

Figure A.1: XMCD images of the Fe wedge at (a) +170 V (b) 0 V (c) −170 V at 45° azimuthal angle.

A.2 Differential-strain transfer analysis

The differential strain (DS) model predicts the induced magnetic anisotropy and the direction of the magnetic easy axis by analyzing the accumulated strain in the Fe film due to changes in the strain state of the BTO. This model has been previously used to predict the domain state of a CoFe thin film deposited on BTO [149].

The differential strain (DS) in BTO FE domains can be expressed as $\bar{\epsilon}^{BTO}$ which is difference between the strain along two orthogonal $[010]_{pc}$ and $[100]_{pc}$ axes. For instance, the $\bar{\epsilon}^{BTO}$ in BTO for FE a_1, a_2 and c domains is +1.1%, -1.1% and 0%, respectively. During the growth (gr) of FM film, a part of this DS is transferred to the FM film. When FE BTO domain changes in response to external stimuli (temperature change or voltage), the Fe film on top experiences this differential strain change $\Delta\bar{\epsilon}^{BTO}$ with respect to BTO growth strain. The differential strain $\bar{\epsilon}^{FM}$ in FM layer at any instant depends on the DS transmitted at growth and the change in the DS of BTO with respect to growth time, i.e. $\bar{\epsilon}^{FM} = \delta_{gr}\ \bar{\epsilon}^{BTO}_{gr} + \delta\ \Delta\bar{\epsilon}^{BTO}$, where δ_{gr} is the strain transfer at the growth time and δ is strain transfer due to other stimulus like temperature change or voltage. The total DS in the FM film $\bar{\epsilon}^{FM}$ determines the modulation in the imprinted magnetic domain pattern of the FM film, as the magnetoelastic anisotropy K_σ is given by

$$K_\sigma \propto \lambda_s(\epsilon^{FM}_{010} - \epsilon^{FM}_{100}) \propto \lambda_s\bar{\epsilon}^{FM} \tag{A.1}$$

where λ_s is the magnetostriction. Therefore a strain change in BTO can induce a strain

transfer in the Fe film altering the magnetoelastic anisotropy. If the magnetoelastic anisotropy dominates over other sources of anisotropy, a rotation of magnetization is observed in the Fe film [149]. The magnetic easy axis or the magnetic anisotropy in the Fe film is thus determined by the sign of the accumulated differential strain. For positive magnetostriction of Fe, $\overline{\epsilon}^{FM} > 0$ and $\overline{\epsilon}^{FM} < 0$ orient the magnetic easy axis along $[010]_{pc}$ and $[100]_{pc}$, respectively.

The strain changes in BTO are fully or partially transferred to the FM film depending on the source of the strain: sample growth (gr), temperature change (th), or voltage (V). The strain transfer during growth is between 0 to 10%, above which an imprint of BTO domains on Fe is expected. For our case, a strain transfer of $\delta_{gr} = 10\%$ is considered at growth time [8, 148]. The strain transfer during thermal cycle and application of voltage is much more efficient and is considered to be $\delta = 100\%$ [8, 148]. With a_1-a_2 as the initial state for BTO during Fe film growth, only two kind of FM regions (β and γ) are expected after application of the voltage [147, 149]. Hence, a_1^{gr}-a_2^{gr} state cannot explain the coexistence of three kinds of FM regions (α, β, and γ). Therefore, at growth time, BTO is either in a a_1-c or a_2-c FE domain state. As the domain walls are oriented along $[100]_{pc}$ after application of electric voltage in Figure 5.11(d), it is deduced that the BTO possessed an initial a_1-c state.

Using the proper notation for different sources of strain transfer, the BTO converted from a_1^{gr}-c^{gr} during growth to a_1^{th}-a_2^{th} after the thermal cycle and to a_1^{V}-c^{V} after application of the voltage. The FE domain pattern and the corresponding FM domain pattern during growth, after thermal cycle and after applying voltage are shown schematically in Figure A.2. The grey and blue color in the FM domain pattern represent the direction of the induced magnetization along the $[100]_{pc}$ and $[010]_{pc}$ axes in the Fe film. The numbers in the brackets in the FE and FM domain state depict the DS $\overline{\epsilon}^{BTO}$ and $\overline{\epsilon}^{FM}$, respectively. The direction (either $[100]_{pc}$ or $[010]_{pc}$) and the magnitude of the strain in the Fe and BTO are depicted schematically on the right side of the corresponding FM and FE domain state.

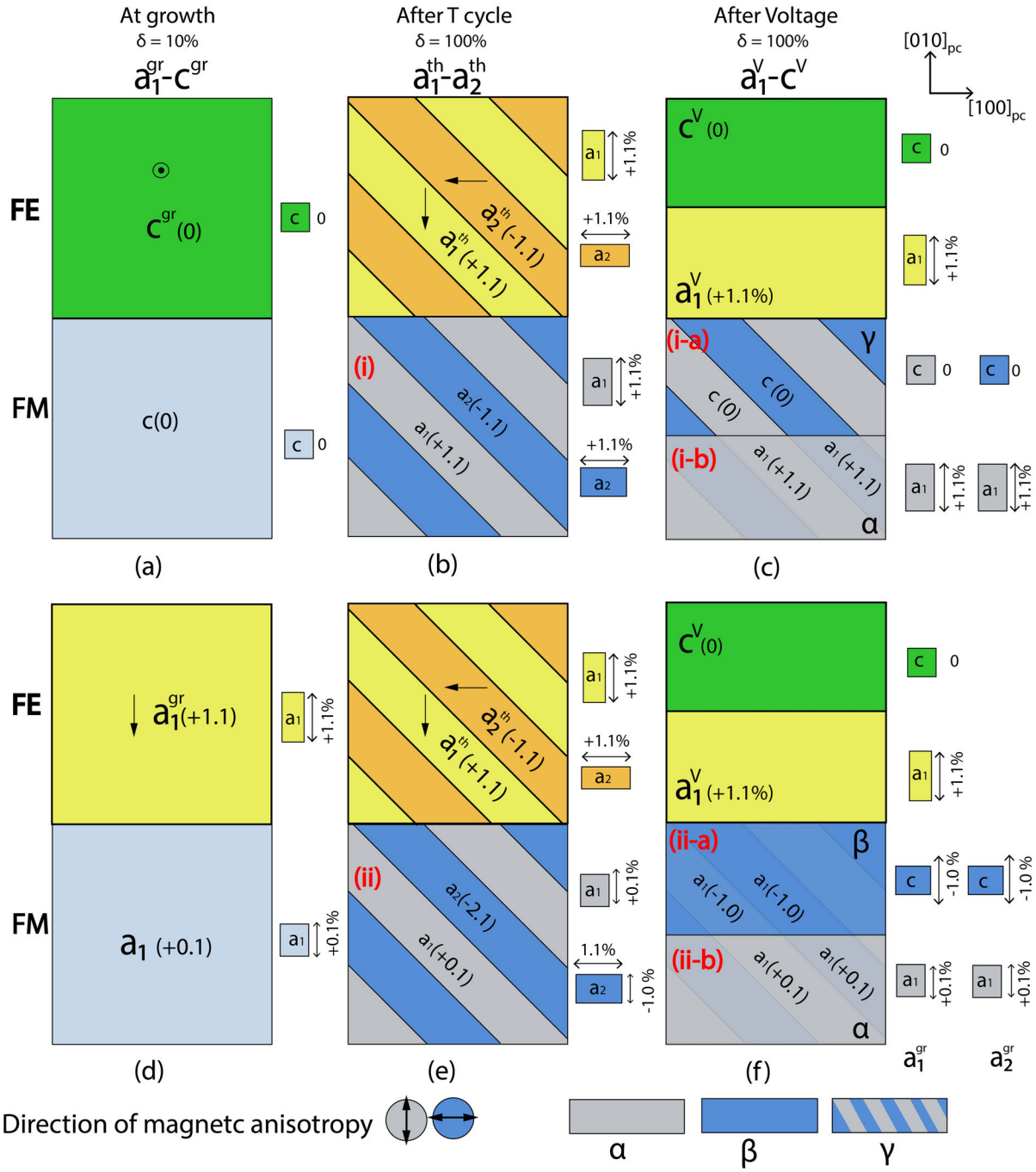

Figure A.2: Schematic showing FE and the corresponding imprinted FM domain patterns (a,d) at growth (b,e) after temperature cycle and (c,f) after applying voltage. The FE domain pattern evolves from a_1^{gr}-c^{gr} to a_1^{th}-a_2^{th} after temperature cycle to a_1^{V}-c^{V} after applying voltage.

The initial c^{gr} domain of BTO and the corresponding FM domain state is shown in Figure A.2(a). No imprint is expected in the Fe film on top of a c^{gr} domain as it is isotropic. After the thermal cycle, the c^{gr} domain converts to a_1^{th}-a_2^{th} domains as shown in the top FE pattern in Figure A.2(b). The FM region over a_1^{th} and a_2^{th}

experiences a tensile strain of 1.1% along $[010]_{pc}$ and $[100]_{pc}$, respectively. Therefore, the magnetization in regions above a_1^{th} and a_2^{th} orients along $[010]_{pc}$ and $[100]_{pc}$ for a positive Fe magnetostriction. On application of voltage, the a_1^{th}-a_2^{th} FE state in Figure A.2(b) convert to a_1^V-c^V in Figure A.2(c). Beginning from a c^{gr} at growth time, the following transitions (marked in Figure A.2) take place:

- **(i) → (i-a)**
  FE: $c^{gr} \rightarrow a_1^{th}$-$a_2^{th} \rightarrow c^V$
  In this case, the strain introduced after the thermal cycle is removed after applying the voltage and Fe becomes isotropic. It is expected that the magnetization direction will not change with respect to (i) as the magnetization is already aligned along easy axis, thus preserving the white-blue contrast or so-called γ pattern.

- **(i) → (i-b)**
  FE: $c^{gr} \rightarrow a_1^{th}$-$a_2^{th} \rightarrow a_1^V$
  The FM regions over new a_1^V domains experience tensile strain of 1.1% along $[010]_{pc}$ irrespective of whether they originate from a_1^{th} or a_2^{th}. With $\bar{\epsilon}^{FM} = +1.1\%$, the magnetic anisotropy of Fe is expected to orient along $[010]_{pc}$ resulting in a homogeneous white XMCD contrast, i.e. α region.

The initial a_1^{gr} domain of BTO after growth and the corresponding FM domain state is shown in Figure A.2(d). The a_1^{gr} BTO domain experiences a tensile strain of 1.1% along $[010]_{pc}$. After the thermal cycle, the a_1^{gr} domain converts to a_1^{th}-a_2^{th} domains as shown in FE pattern in Figure A.2(e). The FM region over a_1^{th} experiences a tensile strain of 0.1% along $[010]_{pc}$. The FM regions over a_2^{th} experience a compressive strain of 1% along [010] and a tensile strain of 1.1% along $[100]_{pc}$, i.e $\bar{\epsilon}^{FM}$ = -2.1% . Therefore, the magnetization in FM regions above a_1^{th} and a_2^{th} orients along $[010]_{pc}$ and $[100]_{pc}$, respectively for a positive Fe magnetostriction (see Appendix section A.1 for the sign of magnetostriction). On application of voltage, the a_1^{th}-a_2^{th} FE state in Figure A.2(e) converts to a_1^V-c^V as shown in Figure A.2(f). The following transitions (marked in the Figure A.2) take place:

- **(ii) → (ii-a)**
  FE: $a_1^{gr} \rightarrow a_1^{th}$-$a_2^{th} \rightarrow c^V$
  The Fe on top of the new c^V domains is compressed by 1% along $[010]_{pc}$ irrespective of whether they originate from a_1^{th} or a_2^{th}. The magnetic anisotropy is expected to orient along $[100]_{pc}$ because of the $\bar{\epsilon}^{FM}$ = -1.0%. In this case a blue XMCD contrast, i.e. β region is expected.

- **(ii) → (ii-b)**
  FE: $a_1^{gr} \rightarrow a_1^{th}$-$a_2^{th} \rightarrow a_1^V$
  The FM regions over new a_1^V domains experience a small tensile strain of 0.1% irrespective of whether they originate from a_1^{th} or a_2^{th}. The $\overline{\epsilon}^{FM} = +0.1\%$ is expected to orient the magnetic anisotropy along $[010]_{pc}$ which would show a white XMCD contrast, i.e. α region.

Further increasing the voltage should convert the remaining a_1^V domains to c^V domains (also discussed in section 1.7.1.1). Such domain transformation is depicted in Figure A.3. The following transitions take place:

- **(i-b)→ (i-b-1)**
  FE: $c^{gr} \rightarrow a_1^{th}$-$a_2^{th} \rightarrow a_1^V \rightarrow c^V$
  The Fe on top of the new c^V domains is compressed by 1.1% along $[010]_{pc}$ irrespective of their origin from of a_1^{th} or a_2^{th} and become isotropic. With $\overline{\epsilon}^{FM} = 0\%$, the magnetic anisotropy remains along $[010]_{pc}$ preserving the previous homogeneous white XMCD contrast, i.e. α region.

- **(ii-b) → (ii-b-1)**
  FE: $a_1^{gr} \rightarrow a_1^{th}$-$a_2^{th} \rightarrow a_1^V \rightarrow c^V$
  The FM regions over new c^V domains experience a compressive strain of 1.1% along $[010]_{pc}$ irrespective of their origin from of a_1^{th} or a_2^{th}. The magnetic anisotropy orients along $[010]_{pc}$ due to $\overline{\epsilon}^{FM}$ = -1.0%, showing a homogeneous blue XMCD contrast, i.e. β region.

The differential strain model predicts the coexistence of all three types of FM regions, i.e. α, β and γ as experimentally observed in Figure 5.11. At large voltage, the α and γ regions are correlated to c^V domains originating from c^{gr} domains at growth time. The β regions are correlated to c^V domains originating from a_1^{gr} domains at growth time. Consequently, the β regions experience a significant compressive strain along $[010]_{pc}$ at large voltage unlike α and γ regions.

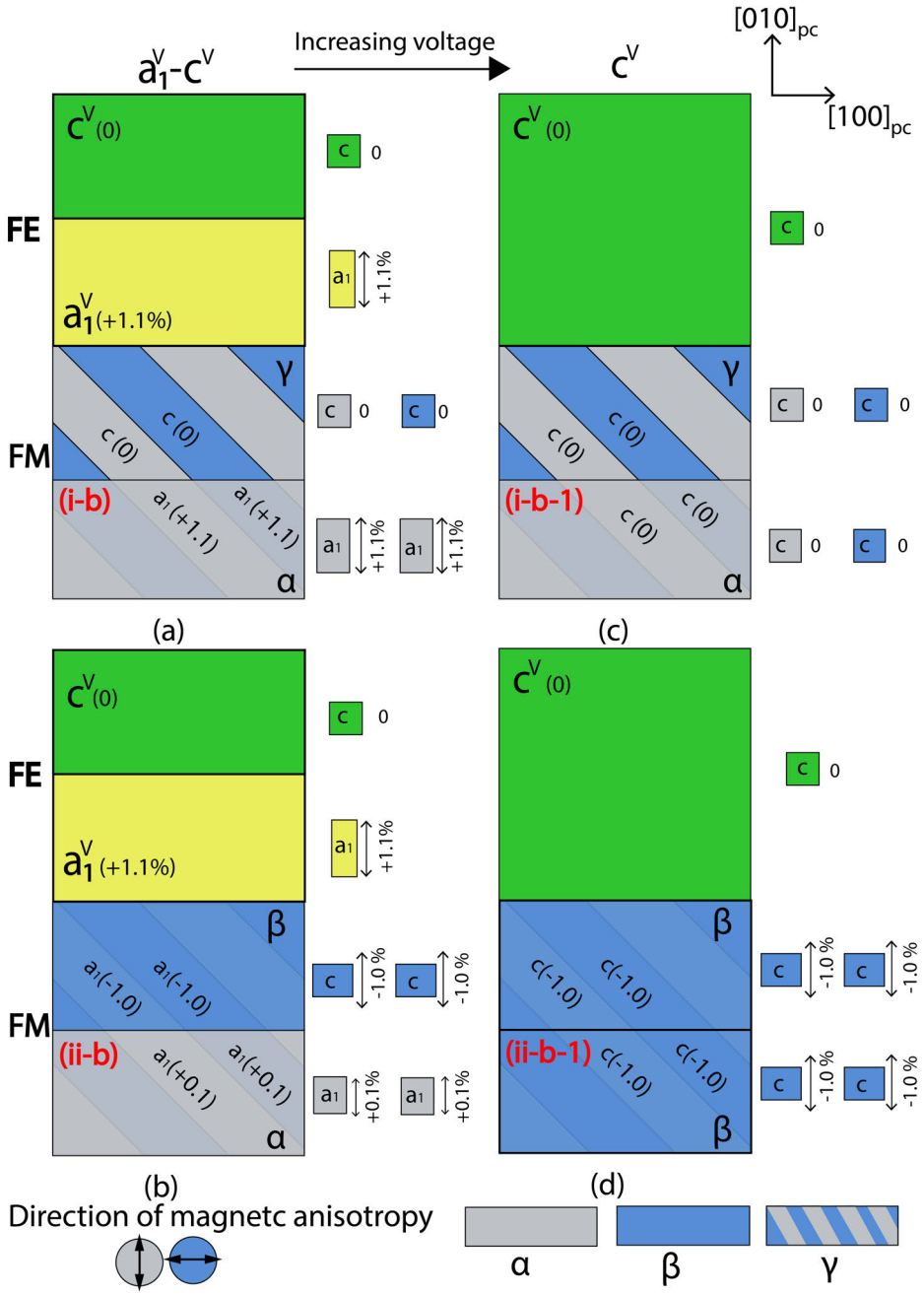

Figure A.3: Schematic showing FE and the corresponding imprinted FM domain patterns (a,b) (same as Figure A.2(c,f)) after applying voltage and (b,d) after increasing voltage. The FE domain pattern evolves from a_1^V-c^V to a complete c^V domain state after increasing the voltage.

A.3 Temperature dependent displacement of critical thickness

In order to quantify the change in the T_c necessary to decrease the critical thickness by 1 Å, temperature dependent XMCD measurements have been performed on an Fe wedge film on BTO, similar to the sample which showed an electric field induced modification of t_{Fe}^{FM}. Figure A.4(a) and (b) show the XMCD images recorded at 80 K and 340 K, respectively. Increasing the temperature from 80 K to 340 K (260 K change) leads to an extension of the FM region by approximately 1 μm which is associated to a decrease of t_{Fe}^{FM} by approximately 5 Å. Hence, if an electric-field induced change of T_c can explain the experimental observation of a decrease in t_{Fe}^{FM} of about 1 Å, such a change should correspond to an increase of T_c of about 50 K.

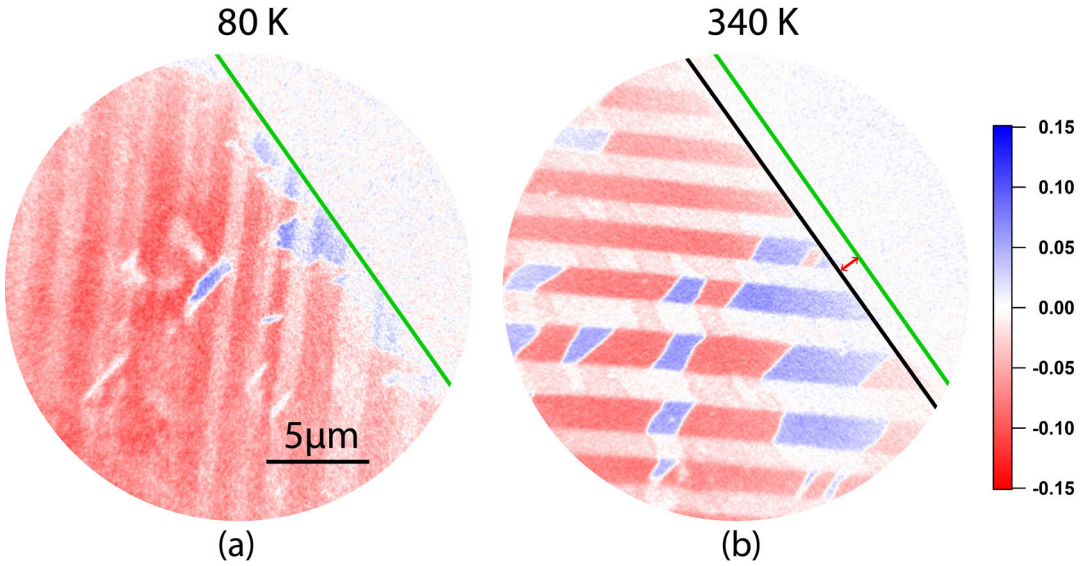

Figure A.4: XMCD image of Fe wedge deposited on top of BTO recorded at (a) 80 K and (b) 340 K. The green and the black line in (a) and (b) mark the onset of ferromagnetic order at 80 K and 340 K, respectively. As observed by comparing the green and black lines in (b), the onset of the ferromagnetism is shifted by 1μm which corresponds to a change in the critical thickness by 5 Å. Therefore, change in the critical thickness of 1 Å would correspond to a change in T_c by about 50 K.

Publications

1. Arora, A., Mawass M. A., Sandig O., Luo C., Ünal A. A., Radu F., Valencia S. and Kronast F., Spatially resolved investigation of all optical magnetization switching in TbFe alloys, *Scientific Reports*, **7**, 9456 (2017).

2. Arora A., Phillips L. C. , Hassine M. B., Nukala P., Ünal A.A., Dkhil B., *et al.* Switching on Superferromagnetism. *Manuscript in preparation*

3. Ünal A. A., Parabas A., Arora A., Ehrler J., Barton C., Valencia S., Bali R.,Thomson T., Yildiz F., Kronast F. Laser-driven formation of transient local ferromagnetism in FeRh thin films, *Ultramicroscopy*, **183**, 104-108 (2017).

4. Grisolia M., Varignon J., Santolino G. S., Arora A., Valencia S.,*et al.*, Hybridization controlled charge transfer and induced magnetism at correlated oxide interfaces, *Nature Physics*, **12**, 484 (2016).

5. Palau A., Valencia S., Del-Valle N., Navau C., Cialone M., Arora A., Kronast F. *et al.*, Encoding magnetic states in monopole-like configurations using superconducting dots. *Advanced Science*, **3**, 1600207 (2016).

References

[1] Bader, S. & Parkin, S. Spintronics. *Annu. Rev. Condens. Matter Phys.* **1**, 71–88 (2010).

[2] Katine, J., Albert, F., Buhrman, R., Myers, E. & Ralph, D. Current-driven magnetization reversal and spin-wave excitations in Co/Cu/Co pillars. *Physical Review Letters* **84**, 3149 (2000).

[3] Myers, E., Ralph, D., Katine, J., Louie, R. & Buhrman, R. Current-induced switching of domains in magnetic multilayer devices. *Science* **285**, 867–870 (1999).

[4] Eerenstein, W., Mathur, N. & Scott, J. F. Multiferroic and magnetoelectric materials. *Nature* **442**, 759 (2006).

[5] Ramesh, R. & Spaldin, N. A. Multiferroics: progress and prospects in thin films. *Nature Materials* **6**, 21 (2007).

[6] Stanciu, C. D. *et al.* All-optical magnetic recording with circularly polarized light. *Phys. Rev. Lett.* **99**, 047601 (2007).

[7] Sahoo, S. *et al.* Ferroelectric control of magnetism in $BaTiO_3$/ Fe heterostructures via interface strain coupling. *Physical Review B* **76**, 092108 (2007).

[8] Lahtinen, T. H., Franke, K. J. & Van Dijken, S. Electric-field control of magnetic domain wall motion and local magnetization reversal. *Scientific reports* **2** (2012).

[9] Franke, K. J. *et al.* Reversible electric-field-driven magnetic domain-wall motion. *Physical Review X* **5**, 011010 (2015).

[10] Kim, H. K. *et al.* Magnetoelectric control of superparamagnetism. *Nano letters* **13**, 884–888 (2013).

[11] Chiba, D. *et al.* Electrical control of the ferromagnetic phase transition in cobalt at room temperature. *Nature Materials* **10**, 853 (2011).

[12] Allibe, J. *et al.* Room temperature electrical manipulation of giant magnetoresistance in spin valves exchange-biased with $BiFeO_3$. *Nano letters* **12**, 1141–1145 (2012).

[13] Garcia, V. *et al.* Ferroelectric control of spin polarization. *Science* **327**, 1106–1110 (2010).

[14] Jiang, S., Shan, J. & Mak, K. F. Electric-field switching of two-dimensional van der waals magnets. *Nature Materials* 1 (2018).

[15] Mangin, S. *et al.* Engineered materials for all-optical helicity-dependent magnetic switching. *Nature Materials* **13**, 286 (2014).

[16] Lambert, C.-H. *et al.* All-optical control of ferromagnetic thin films and nanostructures. *Science* **345**, 1337–1340 (2014).

[17] Richter, H., Lyberatos, A., Nowak, U., Evans, R. F. L. & Chantrell, R. W. The thermodynamic limits of magnetic recording. *Journal of Applied Physics* **111**, 033909 (2012).

[18] Song, C., Cui, B., Li, F., Zhou, X. & Pan, F. Recent progress in voltage control of magnetism: Materials, mechanisms, and performance. *Progress in Materials Science* **87**, 33–82 (2017).

[19] Prellier, W., Singh, M. & Murugavel, P. The single-phase multiferroic oxides: from bulk to thin film. *Journal of Physics: Condensed Matter* **17**, R803 (2005).

[20] Cheong, S.-W. & Mostovoy, M. Multiferroics: a magnetic twist for ferroelectricity. *Nature Materials* **6**, 13 (2007).

[21] Duan, C.-G., Jaswal, S. S. & Tsymbal, E. Y. Predicted magnetoelectric effect in $Fe/BaTiO_3$ multilayers: ferroelectric control of magnetism. *Physical Review Letters* **97**, 047201 (2006).

[22] Valencia, S. *et al.* Interface-induced room-temperature multiferroicity in $BaTiO_3$. *Nature Materials* **10**, 753 (2011).

[23] Kittel, C. *Introduction to Solid State Physics* (John Wiley & Sons, Inc., New York, 1986), 6th edn.

[24] Callen, E. & Callen, H. B. Magnetostriction, forced magnetostriction, and anomalous thermal expansion in ferromagnets. *Physical Review* **139**, A455 (1965).

[25] Cullity, B. D. & Graham, C. D. *Introduction to magnetic materials* (John Wiley & Sons, 2011).

[26] Frenkel, J. & Dorfman, J. Spontaneous and induced magnetisation in ferromagnetic bodies. *Nature* **126**, 274–275 (1930).

[27] Kittel, C. Theory of the structure of ferromagnetic domains in films and small particles. *Physical Review* **70**, 965 (1946).

[28] Knobel, M. *et al.* Superparamagnetism and other magnetic features in granular materials: a review on ideal and real systems. *Journal of nanoscience and nanotechnology* **8**, 2836–2857 (2008).

[29] Bean, C. & Livingston, u. J. D. Superparamagnetism. *Journal of Applied Physics* **30**, S120–S129 (1959).

[30] Bedanta, S. *Supermagnetism in magnetic nanoparticle systems.* Ph.D. thesis, Universität Duisburg-Essen, Fakultät für Physik (2006).

[31] Mørup, S., Madsen, M. B., Franck, J., Villadsen, J. & Koch, C. J. A new interpretation of mössbauer spectra of microcrystalline goethite:"super-ferromagnetism" or "super-spin-glass" behaviour? *Journal of Magnetism and Magnetic Materials* **40**, 163–174 (1983).

[32] Mørup, S. & Christiansen, G. Influence of magnetic anisotropy on the superferromagnetic ordering in nanocomposites. *Journal of Applied Physics* **73**, 6955–6957 (1993).

[33] Campbell, I. Indirect exchange for rare earths in metals. *Journal of Physics F: Metal Physics* **2**, L47 (1972).

[34] Coey, J. Amorphous magnetic order. *Journal of Applied Physics* **49**, 1646–1652 (1978).

[35] Hebler, B., Hassdenteufel, A., Reinhardt, P., Karl, H. & Albrecht, M. Ferrimagnetic Tb-Fe alloy thin films: composition and thickness dependence of magnetic properties and all-optical switching. *Frontiers in Materials* **3**, 8 (2016).

[36] Wang, J. *et al.* Epitaxial $BiFeO_3$ multiferroic thin film heterostructures. *science* **299**, 1719–1722 (2003).

[37] Hur, N. *et al.* Electric polarization reversal and memory in a multiferroic material induced by magnetic fields. *Nature* **429**, 392–395 (2004).

[38] Van Aken, B. B., Palstra, T. T., Filippetti, A. & Spaldin, N. A. The origin of ferroelectricity in magnetoelectric $YMnO_3$. *Nature Materials* **3**, 164–170 (2004).

[39] Lahtinen, T. *Ferromagnetic-Ferroelectric Domain Coupling in Multiferroic Heterostructures*. Ph.D. thesis (2013).

[40] Kwei, G., Lawson, A., Billinge, S. & Cheong, S. Structures of the ferroelectric phases of barium titanate. *The Journal of Physical Chemistry* **97**, 2368–2377 (1993).

[41] Von Hippel, A. Ferroelectricity, domain structure, and phase transitions of barium titanate. *Reviews of Modern Physics* **22**, 221 (1950).

[42] Damjanovic, D. Ferroelectric, dielectric and piezoelectric properties of ferroelectric thin films and ceramics. *Reports on Progress in Physics* **61**, 1267 (1998).

[43] Merz, W. J. Domain formation and domain wall motions in ferroelectric $BaTiO_3$ single crystals. *Physical Review* **95**, 690 (1954).

[44] Lagos, P. *et al.* Identification of ferroelectric domain structures in $BaTiO_3$ for raman spectroscopy. *Surface science* **532**, 493–500 (2003).

[45] Chopdekar, R. *et al.* Spatially resolved strain-imprinted magnetic states in an artificial multiferroic. *Physical Review B* **86**, 014408 (2012).

[46] Schmid, H. Multi-ferroic magnetoelectrics. *Ferroelectrics* **162**, 317–338 (1994).

[47] Khomskii, D. Multiferroics: Different ways to combine magnetism and ferroelectricity. *Journal of Magnetism and Magnetic Materials* **306**, 1–8 (2006).

[48] Vazquez, M. & Hernando, A. A soft magnetic wire for sensor applications. *Journal of Physics D: Applied Physics* **29**, 939 (1996).

[49] Reiss, G. & Hütten, A. Magnetic nanoparticles: applications beyond data storage. *Nature Materials* **4**, 725–726 (2005).

[50] Zeng, H., Li, J., Liu, J. P., Wang, Z. L. & Sun, S. Exchange-coupled nanocomposite magnets by nanoparticle self-assembly. *Nature* **420**, 395–398 (2002).

[51] Hill, N. A. Why are there so few magnetic ferroelectrics? (2000).

[52] Neaton, J., Ederer, C., Waghmare, U., Spaldin, N. & Rabe, K. First-principles study of spontaneous polarization in multiferroic $BiFO_3$. *Physical Review B* **71**, 014113 (2005).

[53] Kimura, T. *et al.* Magnetic control of ferroelectric polarization. *Nature* **426**, 55–58 (2003).

[54] Kimura, T. Spiral magnets as magnetoelectrics. *Annu. Rev. Mater. Res.* **37**, 387–413 (2007).

[55] Fiebig, M., Lottermoser, T., Meier, D. & Trassin, M. The evolution of multiferroics. *Nature Reviews Materials* **1**, 16046 (2016).

[56] Fiebig, M. Revival of the magnetoelectric effect. *Journal of Physics D: Applied Physics* **38**, R123 (2005).

[57] Van Suchtelen, J. Product properties: a new application of composite materials. *Philips Res. Rep* **27**, 28–37 (1972).

[58] B.Sc., J. C. C. Some experiments on polarized röntgen radiation. *The London, Edinburgh, and Dublin Philosophical Magazine and Journal of Science* **25**, 792–802 (1913).

[59] De Groot, F. & Kotani, A. *Core level spectroscopy of solids* (CRC press, 2008).

[60] Regan, T. *et al.* Chemical effects at metal/oxide interfaces studied by x-ray-absorption spectroscopy. *Physical Review B* **64**, 214422 (2001).

[61] Beaurepaire, E., Bulou, H., Scheurer, F. & Kappler, J. P. *Magnetism: A synchrotron radiation approach*, vol. 697 (Springer, 2006).

[62] Schütz, G. *et al.* Absorption of circularly polarized x rays in iron. *Physical review letters* **58**, 737 (1987).

[63] Beaurepaire, E., Scheurer, F., Krill, G. & Kappler, J.-P. *Magnetism and synchrotron radiation*, vol. 34 (Springer, 2001).

[64] Stöhr, J. & Wu, Y. X-Ray magnetic circular dichroism: Basic concepts and theory for 3D transition metal atoms. *In "New Directions in Research with Third-Generation Soft X-Ray Synchrotron Radiation Sources", NATO ASI Series, Series E: Applied Sciences, Eds. A.S.Schlachter and F.J.Wuilleumie* **254**, 221–250 (1994).

[65] Fano, U. Spin orientation of photoelectrons ejected by circularly polarized light. *Physical Review* **178**, 131 (1969).

[66] Carra, P., Thole, B., Altarelli, M. & Wang, X. X-ray circular dichroism and local magnetic fields. *Physical Review Letters* **70**, 694 (1993).

[67] Thole, B., Carra, P., Sette, F. & van der Laan, G. X-ray circular dichroism as a probe of orbital magnetization. *Physical Review Letters* **68**, 1943 (1992).

[68] Bauer, E. Photoelectron microscopy. *Journal of Physics: Condensed Matter* **13**, 11391 (2001).

[69] Schneider, C. M. & Schönhense, G. Investigating surface magnetism by means of photoexcitation electron emission microscopy. *Reports on Progress in Physics* **65**, 1785 (2002).

[70] Kronast, F. & Valencia, S. SPEEM: The photoemission microscope at the dedicated microfocus PGM beamline UE49-PGMa at BESSY II. *Journal of large-scale research facilities JLSRF* **2**, 90 (2016).

[71] Nakajima, R., Stöhr, J. & Idzerda, Y. U. Electron-yield saturation effects in L-edge x-ray magnetic circular dichroism spectra of Fe, Co, and Ni. *Physical Review B* **59**, 6421 (1999).

[72] Stohr, J. & Anders, S. X-ray spectro-microscopy of complex materials and surfaces. *IBM Journal of Research and Development* **44**, 535–551 (2000).

[73] Gierster, L., Pape, L., Ünal, A. & Kronast, F. A sample holder with integrated laser optics for an ELMITEC photoemission electron microscope. *Review of Scientific Instruments* **86**, 023702 (2015).

[74] Cialone, M. Photoemission electron microscopy of multiferroic systems. Unpublished master's thesis. *Freie University Berlin* (2015).

[75] Beaurepaire, E., Merle, J.-C., Daunois, A. & Bigot, J.-Y. Ultrafast spin dynamics in ferromagnetic nickel. *Physical review letters* **76**, 4250 (1996).

[76] Liu, X. *et al.* Dynamics of magnetization, reversal, and ultrafast demagnetization of TbFeCo amorphous films. *Applied Physics Letters* **92**, 232501 (2008).

[77] Guarisco, D., Burgermeister, R., Stamm, C. & Meier, F. Magnetization reversal in the picosecond range measured with time-resolved magneto-optical kerr effect. *Applied Physics Letters* **68**, 1729–1731 (1996).

[78] Hohlfeld, J. *et al.* Fast magnetization reversal of GdFeCo induced by femtosecond laser pulses. *Physical Review B* **65**, 012413 (2001).

[79] Atxitia, U., Chubykalo-Fesenko, O., Walowski, J., Mann, A. & Münzenberg, M. Evidence for thermal mechanisms in laser-induced femtosecond spin dynamics. *Physical Review B* **81**, 174401 (2010).

[80] Alebrand, S., Hassdenteufel, A., Steil, D., Cinchetti, M. & Aeschlimann, M. Interplay of heating and helicity in all-optical magnetization switching. *Physical Review B* **85**, 092401 (2012).

[81] Kimel, A., Kirilyuk, A., Usachev, P., Pisarev, R. *et al.* Ultrafast non-thermal control of magnetization by instantaneous photomagnetic pulses. *Nature* **435**, 655 (2005).

[82] Hansteen, F., Kimel, A., Kirilyuk, A. & Rasing, T. Nonthermal ultrafast optical control of the magnetization in garnet films. *Physical Review B* **73**, 014421 (2006).

[83] Stanciu, C. *et al.* Ultrafast interaction of the angular momentum of photons with spins in the metallic amorphous alloy GdFeCo. *Physical Review Letters* **98**, 207401 (2007).

[84] Van der Ziel, J., Pershan, P. & Malmstrom, L. Optically-induced magnetization resulting from the inverse faraday effect. *Physical Review Letters* **15**, 190 (1965).

[85] Pershan, P., Van der Ziel, J. & Malmstrom, L. Theoretical discussion of the inverse faraday effect, raman scattering, and related phenomena. *Physical Review* **143**, 574 (1966).

[86] Pitaevskii, L. Electric forces in a transparent dispersive medium. *Sov. Phys. JETP* **12**, 1008–1013 (1961).

[87] Kirilyuk, A., Kimel, A. V. & Rasing, T. Ultrafast optical manipulation of magnetic order. *Reviews of Modern Physics* **82**, 2731 (2010).

[88] Koopmans, B., Van Kampen, M., Kohlhepp, J. & De Jonge, W. Ultrafast magneto-optics in nickel: magnetism or optics? *Physical Review Letters* **85**, 844 (2000).

[89] van der Ziel, J. P., Pershan, P. S. & Malmstrom, L. D. Optically-induced magnetization resulting from the inverse faraday effect. *Physical Review Letters* **15**, 190–193 (1965).

[90] Alebrand, S. *et al.* Light-induced magnetization reversal of high-anisotropy TbCo alloy films. *Applied Physics Letters* **101**, 162408 (2012).

[91] Vahaplar, K. *et al.* All-optical magnetization reversal by circularly polarized laser pulses: Experiment and multiscale modeling. *Physical Review B* **85**, 104402 (2012).

[92] Ostler, T. *et al.* Ultrafast heating as a sufficient stimulus for magnetization reversal in a ferrimagnet. *Nature communications* **3**, 1666 (2012).

[93] Radu, I. *et al.* Transient ferromagnetic-like state mediating ultrafast reversal of antiferromagnetically coupled spins. *Nature* **472**, 205 (2011).

[94] Hohlfeld, J., Stanciu, C. & Rebei, A. Athermal all-optical femtosecond magnetization reversal in GdFeCo. *Applied Physics Letters* **94**, 152504 (2009).

[95] Cheng, T. *et al.* Temperature dependence of all-optical ultrafast magnetization switching in TbFeCo. *IEEE Transactions on Magnetics* **48**, 3387–3389 (2012).

[96] Bunce, C. *et al.* Laser-induced magnetization switching in films with perpendicular anisotropy: A comparison between measurements and a multi-macrospin model. *Physical Review B* **81**, 174428 (2010).

[97] Hassdenteufel, A. *et al.* Low-remanence criterion for helicity-dependent all-optical magnetic switching in ferrimagnets. *Physical Review B* **91**, 104431 (2015).

[98] Hassdenteufel, A. *et al.* All-optical helicity dependent magnetic switching in Tb-Fe thin films with a MHz laser oscillator. *Optics express* **22**, 10017–10025 (2014).

[99] Khorsand, A. *et al.* Role of magnetic circular dichroism in all-optical magnetic recording. *Physical Review Letters* **108**, 127205 (2012).

[100] Gierster, L., Ünal, A., Pape, L., Radu, F. & Kronast, F. Laser induced magnetization switching in a TbFeCo ferrimagnetic thin film: discerning the impact of dipolar fields, laser heating and laser helicity by XPEEM. *Ultramicroscopy* **159**, 508–512 (2015).

[101] Malmhäll, R. & Chen, T. Thickness dependence of magnetic hysteretic properties of rf-sputtered amorphous Tb–Fe alloy thin films. *Journal of Applied Physics* **53**, 7843–7845 (1982).

[102] Hassdenteufel, A. *et al.* Thermally assisted all-optical helicity dependent magnetic switching in amorphous $Fe_{100-x}Tb_x$ alloy films. *Advanced Materials* **25**, 3122–3128 (2013).

[103] Hansen, P., Clausen, C., Much, G., Rosenkranz, M. & Witter, K. Magnetic and magneto-optical properties of rare-earth transition-metal alloys containing Gd, Tb, Fe, Co. *Journal of Applied Physics* **66**, 756–767 (1989).

[104] Gierster, L. *Lokales laserinduziertes magnetisches Schalten in TbFeCo Schichten.* Ph.D. thesis, TU Berlin (2014).

[105] El Hadri, M. S. *et al.* Domain size criterion for the observation of all-optical helicity-dependent switching in magnetic thin films. *Physical Review B* **94**, 064419 (2016).

[106] El Hadri, M. *et al.* Electrical characterization of all-optical helicity-dependent switching in ferromagnetic hall crosses. *Applied Physics Letters* **108**, 092405 (2016).

[107] Le Guyader, L. *et al.* Deterministic character of all-optical magnetization switching in GdFe-based ferrimagnetic alloys. *Physical Review B* **93**, 134402 (2016).

[108] El Hadri, M. S. *et al.* Two types of all-optical magnetization switching mechanisms using femtosecond laser pulses. *Physical Review B* **94**, 064412 (2016).

[109] Sandig, O. *et al.* Movement of magnetic domain walls induced by single femtosecond laser pulses. *Physical Review B* **94**, 054414 (2016).

[110] Hassdenteufel, A. *et al.* Dependence of all-optical magnetic switching on the sublattice magnetization orientation in Tb-Fe thin films. *Applied Physics Letters* **105**, 112403 (2014).

[111] Freimuth, F., Blügel, S. & Mokrousov, Y. Laser-induced torques in metallic ferromagnets. *Physical Review B* **94**, 144432 (2016).

[112] Berritta, M., Mondal, R., Carva, K. & Oppeneer, P. M. Ab initio theory of coherent laser-induced magnetization in metals. *Physical Review Letters* **117**, 137203 (2016).

[113] Battiato, M., Barbalinardo, G. & Oppeneer, P. M. Quantum theory of the inverse faraday effect. *Physical Review B* **89**, 014413 (2014).

[114] Popova, D., Bringer, A. & Blügel, S. Theoretical investigation of the inverse faraday effect via a stimulated raman scattering process. *Physical Review B* **85**, 094419 (2012).

[115] Cornelissen, T., Córdoba, R. & Koopmans, B. Microscopic model for all optical switching in ferromagnets. *Applied Physics Letters* **108**, 142405 (2016).

[116] Nieves, P. & Chubykalo-Fesenko, O. Modeling of ultrafast heat-and field-assisted magnetization dynamics in FePt. *Physical Review Applied* **5**, 014006 (2016).

[117] Vahaplar, K. *et al.* Ultrafast path for optical magnetization reversal via a strongly nonequilibrium state. *Physical Review Letters* **103**, 117201 (2009).

[118] Ellis, M. O., Fullerton, E. E. & Chantrell, R. W. All-optical switching in granular ferromagnets caused by magnetic circular dichroism. *Scientific reports* **6**, 30522 (2016).

[119] Gorchon, J., Yang, Y. & Bokor, J. Model for multishot all-thermal all-optical switching in ferromagnets. *Physical Review B* **94**, 020409 (2016).

[120] Hu, J.-M., Duan, C.-G., Nan, C.-W. & Chen, L.-Q. Understanding and designing magnetoelectric heterostructures guided by computation: progresses, remaining questions, and perspectives. *NPJ Computational Materials* **3**, 18 (2017).

[121] Chappert, C., Fert, A. & Van Dau, F. N. The emergence of spin electronics in data storage. *Nature Materials* **6**, 813 (2007).

[122] Ma, J., Hu, J., Li, Z. & Nan, C.-W. Recent progress in multiferroic magnetoelectric composites: from bulk to thin films. *Advanced Materials* **23**, 1062–1087 (2011).

[123] Hu, J.-M., Li, Z., Chen, L.-Q. & Nan, C.-W. High-density magnetoresistive random access memory operating at ultralow voltage at room temperature. *Nature communications* **2**, 553 (2011).

[124] Wang, W.-G., Li, M., Hageman, S. & Chien, C. Electric-field-assisted switching in magnetic tunnel junctions. *Nature Materials* **11**, 64 (2012).

[125] Molegraaf, H. J. *et al.* Magnetoelectric effects in complex oxides with competing ground states. *Advanced Materials* **21**, 3470–3474 (2009).

[126] Yin, Y. *et al.* Enhanced tunnelling electroresistance effect due to a ferroelectrically induced phase transition at a magnetic complex oxide interface. *Nature Materials* **12**, 397 (2013).

[127] Thiele, C., Dörr, K., Bilani, O., Rödel, J. & Schultz, L. Influence of strain on the magnetization and magnetoelectric effect in $La_{0.7}A_{0.3}MnO_3$/ PMN- PT (001)(A= Sr, Ca). *Physical Review B* **75**, 054408 (2007).

[128] Wu, S. *et al.* Reversible electric control of exchange bias in a multiferroic field-effect device. *Nature Materials* **9**, 756 (2010).

[129] Radaelli, G. *et al.* Electric control of magnetism at the Fe/$BaTiO_3$ interface. *Nature communications* **5**, 3404 (2014).

[130] Weiler, M. *et al.* Voltage controlled inversion of magnetic anisotropy in a ferromagnetic thin film at room temperature. *New Journal of Physics* **11**, 013021 (2009).

[131] Dietl, T. & Ohno, H. Dilute ferromagnetic semiconductors: Physics and spintronic structures. *Reviews of Modern Physics* **86**, 187 (2014).

[132] Weisheit, M. *et al.* Electric field-induced modification of magnetism in thin-film ferromagnets. *Science* **315**, 349–351 (2007).

[133] Chiba, D. *et al.* Magnetization vector manipulation by electric fields. *Nature* **455**, 515–518 (2008).

[134] Rushforth, A. *et al.* Voltage control of magnetocrystalline anisotropy in ferromagnetic-semiconductor-piezoelectric hybrid structures. *Physical Review B* **78**, 085314 (2008).

[135] Yamauchi, K., Sanyal, B. & Picozzi, S. Interface effects at a half-metal/ferroelectric junction. *Applied Physics Letters* **91**, 062506 (2007).

[136] Niranjan, M. K., Velev, J. P., Duan, C.-G., Jaswal, S. S. & Tsymbal, E. Y. Magnetoelectric effect at the Fe_3O_4/$BaTiO_3$(001) interface: a first-principles study. *Physical Review B* **78**, 104405 (2008).

[137] Eerenstein, W., Wiora, M., Prieto, J., Scott, J. & Mathur, N. Giant sharp and persistent converse magnetoelectric effects in multiferroic epitaxial heterostructures. *Nature Materials* **6**, 348–351 (2007).

[138] Cherifi, R. *et al.* Electric-field control of magnetic order above room temperature. *Nature Materials* **13**, 345–351 (2014).

[139] Phillips, L. *et al.* Local electrical control of magnetic order and orientation by ferroelastic domain arrangements just above room temperature. *Scientific reports* **5** (2015).

[140] Ghidini, M. *et al.* Perpendicular local magnetization under voltage control in ni films on ferroelectric $BaTiO_3$ substrates. *Advanced Materials* **27**, 1460–1465 (2015).

[141] Yang, S.-W. *et al.* Non-volatile 180 magnetization reversal by an electric field in multiferroic heterostructures. *Advanced Materials* **26**, 7091–7095 (2014).

[142] De Groot, F. X-ray absorption and dichroism of transition metals and their compounds. *Journal of Electron Spectroscopy and Related Phenomena* **67**, 529–622 (1994).

[143] Bocher, L. *et al.* Atomic and electronic structure of the $BaTiO_3$/Fe interface in multiferroic tunnel junctions. *Nano letters* **12**, 376–382 (2011).

[144] Mayer, J., Giannuzzi, L. A., Kamino, T. & Michael, J. TEM sample preparation and FIB-induced damage. *MRS bulletin* **32**, 400–407 (2007).

[145] Gangopadhyay, S. *et al.* Magnetic properties of ultrafine iron particles. *Physical Review B* **45**, 9778 (1992).

[146] Gong, W., Li, H., Zhao, Z. & Chen, J. Ultrafine particles of Fe, Co, and Ni ferromagnetic metals. *Journal of Applied Physics* **69**, 5119–5121 (1991).

[147] Streubel, R., Köhler, D., Schäfer, R. & Eng, L. M. Strain-mediated elastic coupling in magnetoelectric nickel/barium-titanate heterostructures. *Physical Review B* **87**, 054410 (2013).

[148] Lahtinen, T. H. & van Dijken, S. Temperature control of local magnetic anisotropy in multiferroic CoFe/$BaTiO_3$. *Applied Physics Letters* **102**, 112406 (2013).

[149] Yang, T., Hu, J.-M., Nan, C. & Chen, L. On the elastically coupled magnetic and ferroelectric domains: A phase-field model. *Applied Physics Letters* **104**, 202402 (2014).

[150] Sander, D. The correlation between mechanical stress and magnetic anisotropy in ultrathin films. *Reports on Progress in Physics* **62**, 809 (1999).

[151] Sha, X. & Cohen, R. Finite-temperature magnetism in bcc Fe under compression. *Journal of Physics: Condensed Matter* **22**, 372201 (2010).

[152] Körmann, F., Dick, A., Hickel, T. & Neugebauer, J. Pressure dependence of the curie temperature in bcc iron studied by ab initio simulations. *Physical Review B* **79**, 184406 (2009).

[153] Gunkelmann, N. *et al.* Polycrystalline iron under compression: Plasticity and phase transitions. *Physical Review B* **86**, 144111 (2012).

[154] Leger, J., Loriers-Susse, C. & Vodar, B. Pressure effect on the curie temperatures of transition metals and alloys. *Physical Review B* **6**, 4250 (1972).

[155] Cui, X., Zhao, M. & Jiang, Q. Curie transition temperature of ferromagnetic low-dimensional metals. *Thin Solid Films* **472**, 328–333 (2005).

[156] Dürr, W. *et al.* Magnetic phase transition in two-dimensional ultrathin Fe films on Au (100). *Physical Review Letters* **62**, 206 (1989).

[157] Methling, R.-P. *et al.* Magnetic studies on mass-selected iron particles. *The European Physical Journal D-Atomic, Molecular, Optical and Plasma Physics* **16**, 173–176 (2001).

[158] Boubeta, C. M. *et al.* Coverage effects on the magnetism of Fe/ MgO (001) ultrathin films. *Physical Review B* **71**, 014407 (2005).

[159] Bedanta, S. *et al.* Single-particle blocking and collective magnetic states in discontinuous CoFe/Al_2O_3 multilayers. *Journal of Physics D: Applied Physics* **43**, 474002 (2010).

[160] Bedanta, S., Barman, A., Kleemann, W., Petracic, O. & Seki, T. Magnetic nanoparticles: a subject for both fundamental research and applications. *Journal of Nanomaterials* **2013**, 169 (2013).

[161] Djurberg, C. *et al.* Dynamics of an interacting particle system: evidence of critical slowing down. *Physical Review Letters* **79**, 5154 (1997).

[162] Kleemann, W. *et al.* Interacting ferromagnetic nanoparticles in discontinuous $Co_{80}Fe_{20}/Al_2O_3$ multilayers: From superspin glass to reentrant superferromagnetism. *Physical Review B* **63**, 134423 (2001).

[163] Petracic, O. *et al.* Collective states of interacting ferromagnetic nanoparticles. *Journal of Magnetism and Magnetic Materials* **300**, 192–197 (2006).

[164] Sasaki, M., Jönsson, P., Takayama, H. & Mamiya, H. Aging and memory effects in superparamagnets and superspin glasses. *Physical Review B* **71**, 104405 (2005).

[165] Bedanta, S. *et al.* Overcoming the dipolar disorder in dense CoFe nanoparticle ensembles: Superferromagnetism. *Physical Review Letters* **98**, 176601 (2007).